공학박사학위논문

# Decomposition of Bis(3-Sulfopropyl) Disulfide and Poly(Ethylene Glycol-Propylene Glycol) during Cu Electrodeposition and Its Monitoring via Electrochemical Method

구리 전해 도금 과정에서 유기 첨가제로 사용되는
bis(3-sulfopropyl) disulfide 및
poly(ethylene glycol-propylene glycol)의 분해와
이에 대한 전기화학적 모니터링

2016 년 2 월

서울대학교 대학원
화학생물공학부
최 승 회

**Decomposition of Bis(3-Sulfopropyl) Disulfide and Poly(Ethylene Glycol-Propylene Glycol) during Cu Electrodeposition and Its Monitoring via Electrochemical Method**

구리 전해 도금 과정에서 유기 첨가제로 사용되는 bis(3-sulfopropyl) disulfide 및 poly(ethylene glycol-propylene glycol)의 분해와 이에 대한 전기화학적 모니터링

지도교수 김 재 정

이 논문을 최승회 박사학위논문으로 제출함

2015 년 11 월

서울대학교 대학원

화학생물공학부

최 승 회

최승회의 공학박사 학위논문을 인준함

2015 년 12 월

위 원 장 _____ (인)

부 위 원 장 _____ (인)

위 원 _____ (인)

위 원 _____ (인)

위 원 _____ (인)

# Abstract

Cu electrodeposition has been widely utilized in various industrial fields because of its high productivity, low process cost, and excellent products qualities. Cu plating bath usually contains small amount of organic additives that control the morphologies and the properties of Cu deposits. However, the organic additives are unstable under the electrolytic condition and gradually decompose through various chemical and electrochemical reactions. Because of the decomposition of the additives and the consequent degradation of the solution performance, the additives concentrations of the bath are tightly monitored with the electrochemical methods such as cyclic voltammetry stripping (CVS), and maintained by daily bleed-and-feed system.

Despite those efforts, the bath is eventually unusable after long time operation of plating bath. It is because the breakdown products, which affect the properties of deposited Cu films and disturb the signal of monitoring tool, are uncontrollably accumulated in the bath. However, the present monitoring system cannot provide the information of breakdown products, and it is necessary to develop the advanced monitoring methods that enable to analyze not only the parent additives but also their breakdown products. Therefore, this study describes the influences of byproducts on Cu

electrodeposition process in detail and suggests the advanced methodologies enabling the analysis of both the parent organic additives and their breakdown products.

The aging of bis(3-sulfopropyl) disulfide (SPS) over 120 min led to the deterioration in bath performance. It was associated with the breakdown of SPS into 3-mercapto-1-propane sulfonate (MPS) and 1,3-propane disulfonic acid (PDS) via the electro-oxidation reaction and the sequential chemical oxidation by dissolved oxygen gases. The subsequent experiments revealed that the effects of PDS on $Cu^{2+}$ reduction kinetics, Cu film properties and filling capabilities are negligible since it could not form chemical linkage to the Cu surface. However, MPS significantly affected the electrochemical response of plating bath, leading to the inaccurate results in CVS analysis of SPS concentration. Moreover, the presence of MPS deteriorated the filling capability of Cu plating bath. Both aspects implied the need for the development of advanced monitoring methods that provide both SPS and MPS concentrations.

To evaluate their concentrations individually, a two-step CVS analysis was suggested in which the total accelerator concentration ([SPS] + 1/2[MPS]) and conversion ratio were separately determined. All MPS species in the bath were oxidized to SPS by controlling the plating solution pH. Subsequent modified linear approximation technique (MLAT)-CVS analysis successfully revealed the total accelerator concentration in the Cu

plating solution. Individual SPS and MPS concentrations were thereby calculated using the conversion ratio evaluated from the difference in their relative accelerating abilities. This modified method enabled determination of the SPS concentration with <10% error, suggesting a reliable and high accuracy tool to predict pattern filling capabilities of plating solutions.

During electrodeposition, poly(ethylene glycol-propylene glycol) (PEG-PPG), a suppressor-type additive, fragmented into lower molecular weight (MW) units by the oxidative scissoring reaction on ether bond. This reaction accompanied the change in terminal groups from hydroxyl to aldehyde, formic ester, and ketone and reduces average MW. Consequently, the aged solution contained high population of low MW PEG-PPG units, which affects both the electrochemical responses of bath and the properties of Cu deposits. This result indicated that the monitoring of MW of PEG-PPG was necessary for accurate prediction of solution performance.

Considering those factors, the breakdown products from decomposition of additives significantly affect the filling capabilities and Cu film properties. Concentration analyses of both parent additives and its breakdown product are necessary for accurate diagnosis of Cu plating bath. This comprehensive study provides the general guideline for the

development of advanced monitoring methods that are more accurate than conventional CVS.

**Key word: Cu, electrodeposition, organic additive, cyclic voltammetry stripping, bis (3-sulfopropyl) disulfide, poly(ethylene glycol-propylene glycol), modified linear approximation technique, dilution titration**

**Student number: 2012-30260**

# Content

# LIST OF TABLES

# LIST OF FIGURES

# Chapter I. Introduction

## 1.1. Recent Trend for Semiconductor Metallization

The continuous demand for the high performance electronic device and the reduction of process cost have driven the development of ultra large scale integration (ULSI) semiconductor devices. The critical dimension of semiconductor devices has continued to decrease in accordance with Moore's law, and recently, the development of 14 nm-scale technology is ready to be realized. Figure 1.1 describes the critical dimension of logic and memory devices for next generation suggested by 2013 International Technology Roadmap for Semiconductor (ITRS).[1]

Continuous decrease of semiconductor dimension has led to the changes in the wiring materials from Al to Cu.[2] It is attributed to the substantial increase of resistance-capacitance delay (RC delay) caused by the decrease of the wiring width to a few nanometer scale. Therefore, since the late 1990's, the RC delay has dominated the gate delay, determining the overall speed of microprocessor.[3] It stimulates the use of low resistivity wiring materials like Cu (1.67 $\mu\Omega \cdot cm$) and Ag instead of Al (2.66 $\mu\Omega \cdot cm$) in the metallization process. Furthermore, it has been reported that Cu has advantage

over Al against the electromigration problem that are strongly related with the reliability issues.[2,3]

The change in wiring material from Al to Cu accompanies the development of Cu damascene process. Generally, Al metal line is fabricated with the sequential unit processes of physical vapor deposition (PVD), lithography, subtractive etching, and the deposition of surrounding dielectric. However, this process sequence cannot be directly applied to the metallization of Cu, since the non-volatile $CuCl_2$ residue remains on substrate after the subtractive etching process.

Therefore, the damascene process has been developed for Cu metallization. Figure 1.2 presents the standard procedure of damascene process.[6-15] Damascene process typically comprises the unit processes of the deposition of interlayer dielectric material, lithography and the etching for pattern formation, physical vapor deposition (PVD) of diffusion barrier layer, PVD of Cu film as seed layer, electrodeposition of Cu for pattern filling, and the chemical-mechanical polishing for the planarization. Recently, due to the poor step coverage of PVD,[16-19] the alternative processes such as electroless deposition (ELD), chemical vapor deposition (CVD), or atomic layer deposition are suggested for the fabrication of diffusion barrier and Cu seed layer.[20-22]

| Year of Production | 2013 | 2015 | 2017 | 2019 | 2021 | 2023 | 2025 | 2028 |
|---|---|---|---|---|---|---|---|---|
| Logic Industry "Node Name" Label | "16/14" | "10" | "7" | "5" | "3.5" | "2.5" | "1.8" | |
| Logic ½ Pitch (nm) | 40 | 32 | 25 | 20 | 16 | 13 | 10 | 7 |
| Flash ½ Pitch [2D] (nm) | 18 | 15 | 13 | 11 | 9 | 8 | 8 | 8 |
| DRAM ½ Pitch (nm) | 28 | 24 | 20 | 17 | 14 | 12 | 10 | 7.7 |
| FinFET Fin Half-pitch (new) (nm) | 30 | 24 | 19 | 15 | 12 | 9.5 | 7.5 | 5.3 |
| FinFET Fin Width (new) (nm) | 7.6 | 7.2 | 6.8 | 6.4 | 6.1 | 5.7 | 5.4 | 5.0 |
| 6-t SRAM Cell Size(um2) [@60f2] | 0.096 | 0.061 | 0.038 | 0.024 | 0.015 | 0.010 | 0.0060 | 0.0030 |
| MPU/ASIC HighPerf 4t NAND Gate Size(um2) | 0.248 | 0.157 | 0.099 | 0.062 | 0.039 | 0.025 | 0.018 | 0.009 |
| 4-input NAND Gate Density (Kgates/mm) [@155f2] | 4.03E+03 | 6.37E+03 | 1.01E+04 | 1.61E+04 | 2.55E+04 | 4.05E+04 | 6.42E+04 | 1.28E+05 |
| Flash Generations Label (bits per chip) (SLC/MLC) | 64G /128G | 128G /256G | 256G / 512G | 512G / 1T | 512G / 1T | 1T / 2T | 2T / 4T | 4T / 8T |
| Flash 3D Number of Layer targets (at relaxed Poly half pitch) | 16-32 | 16-32 | 16-32 | 32-64 | 48-96 | 64-128 | 96-192 | 192-384 |
| Flash 3D Layer half-pitch targets (nm) | 64nm | 54nm | 45nm | 30nm | 28nm | 27nm | 25nm | 22nm |
| DRAM Generations Label (bits per chip) | 4G | 8G | 8G | 16G | 32G | 32G | 32G | 32G |
| 450mm Production High Volume Manufacturing Begins (100Kwspm) | | | | 2018 | | | | |
| Vdd (High Performance, high Vdd transistors)[**] | 0.86 | 0.83 | 0.80 | 0.77 | 0.74 | 0.71 | 0.68 | 0.64 |
| 1/(CV/I ) (1/psec) [**] | 1.13 | 1.53 | 1.75 | 1.97 | 2.10 | 2.29 | 2.52 | 3.17 |
| On-chip local clock MPU HP [at 4% CAGR] | 5.50 | 5.95 | 6.44 | 6.96 | 7.53 | 8.14 | 8.8 | 9.9 |
| Maximum number wiring levels funchanged | 13 | 13 | 14 | 14 | 15 | 15 | 16 | 17 |
| MPU High-Performance (HP) Printed Gate Length (GLpr) (nm) [**] | 28 | 22 | 18 | 14 | 11 | 9 | 7 | 5 |
| MPU High-Performance Physical Gate Length (GLph) (nm) [**] | 20 | 17 | 14 | 12 | 10 | 8 | 7 | 5 |
| ASIC/Low Standby Power (LP) Physical Gate Length (nm) (GLph)[**] | 23 | 19 | 16 | 13 | 11 | 9 | 8 | 6 |
| ** Note: from the PIDS working group data; however, the calibration of Vdd, GLph, and I/CV is ongoing for improved targets in 2014 ITRS work | | | | | | | | |

**Figure 1.1**. 2013 overall roadmap technology characteristic. (ref. 1)

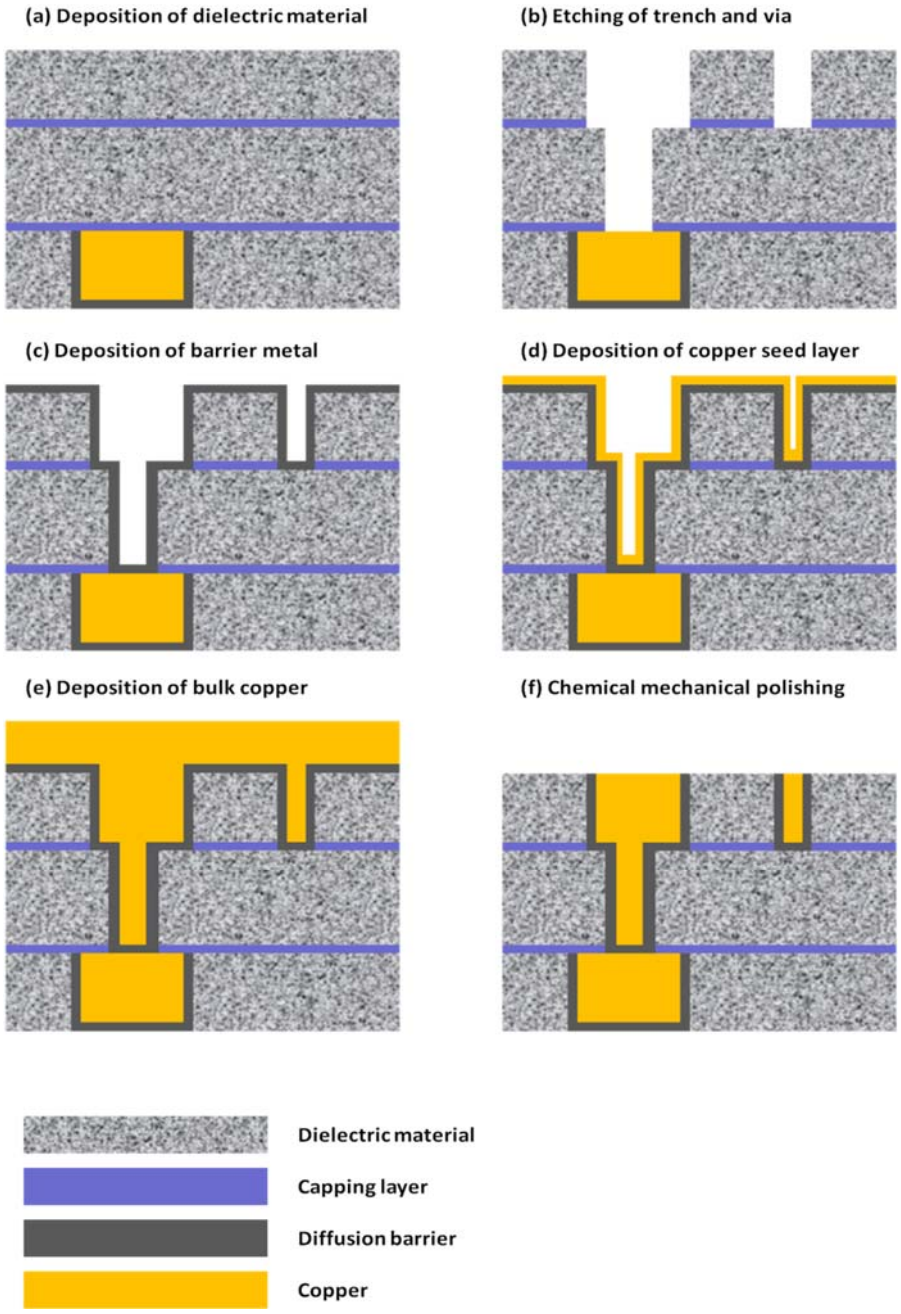


**Figure 1.2**. Schematic diagram of damascene process.

## 1.2. Cu Electrodeposition

Cu electrodeposition is one of core processes in the damascene Cu metallization.[6-15] This process is based on the electrochemical reduction of $Cu^{2+}$ ion onto the substrate surface by the external power source. Figure 1.3 describes the detail mechanism of Cu electrodeposition. Under the electric field by external power source, $Cu^{2+}$ ion from bulk solution moves to the surface of substrate by the convection, the diffusion, and the migration process. Then, $Cu^{2+}$ ion adsorbs on Cu surface and diffuses until it reaches the vacant lattice sites. At the vacant sites, $Cu^{2+}$ is confined and reduced to metallic Cu by two-step charge transfer; the reduction of $Cu^{2+}$ to $Cu^{+}$ and the reduction of $Cu^{+}$ to $Cu^{0}$. Among those process, the slowest step is regarded as the rate-determination step.

The qualities of Cu deposits are affected by process variables, such as the supporting electrolyte, the potential/current waveform, and the combination of organic additives. Supporting electrolyte is non-reactive solute for the purpose of minimizing the solution resistance and stabilizing $Cu^{2+}$ ion in the solution. Currently, sulfuric acid, pyrophosphate and cyanide-based solutions have been generally utilized as supporting electrolytes for various purposes.[23,24] Particularly for the damascene Cu plating, the sulfuric acid-based

electrolyte has been mostly preferred due to its excellent filling capability, low cost, and low toxicity.[10-15]

The potential/current waveform is also significant factor affecting the performance of plating bath. While the constant current/potential is generally applied in the majority of industrial field, the uses of modified waveforms like pulse, and pulse-reverse have been widely applied for the control of grain size,[25] the enhancement of filling capability,[26,27] and the construction of twin boundaries that shows excellent mechanical properties.[28-31]

The morphologies and the properties of Cu deposits are also affected by the combination of organic additives. As shown in Figure 1.4, the organic additives have been categorized as the accelerator, suppressor, and leveler based on their electrochemical behaviors and functionality on the pattern filling process. Suppressor group additives are typically the polymers containing either ethylene or propylene oxide such as polyethylene glycol (PEG), polypropylene glycol (PPG), or copolymer (PEG-PPG).[32-40] They generally control the uniformity of deposited films through adsorption in the complex form with the dissolved cuprous and chloride ions on the surface of Cu.[38,40] Meanwhile, accelerator group additives typically contain either mercapto or disulfide functional groups such as bis(3-sulfopropyl) disulfide (SPS), 3-mercapto-1-propanesulfonate (MPS), and 3-N,N-dimethylaminodithiocarbamoyl-1-propanesulfonic

acid (DPS).[41-48] They improve the surface roughness and enable the superfilling of Cu for fabricating the metal interconnections in various electronic devices.[41-48] The third chemical group is called as the leveler, which decreases the micro-scale roughness of Cu deposits by reducing the current flowing to the peak site to below that flowing to the recessed site through a convection-dependent adsorption mechanism.[49-53] 1,2,3-benzotriazole (BTA), janus green B (JGB), dodecyltrimethylammonium chloride (DTAC), and polyethylene imine (PEI) are typically used as leveling agent.[49-53]

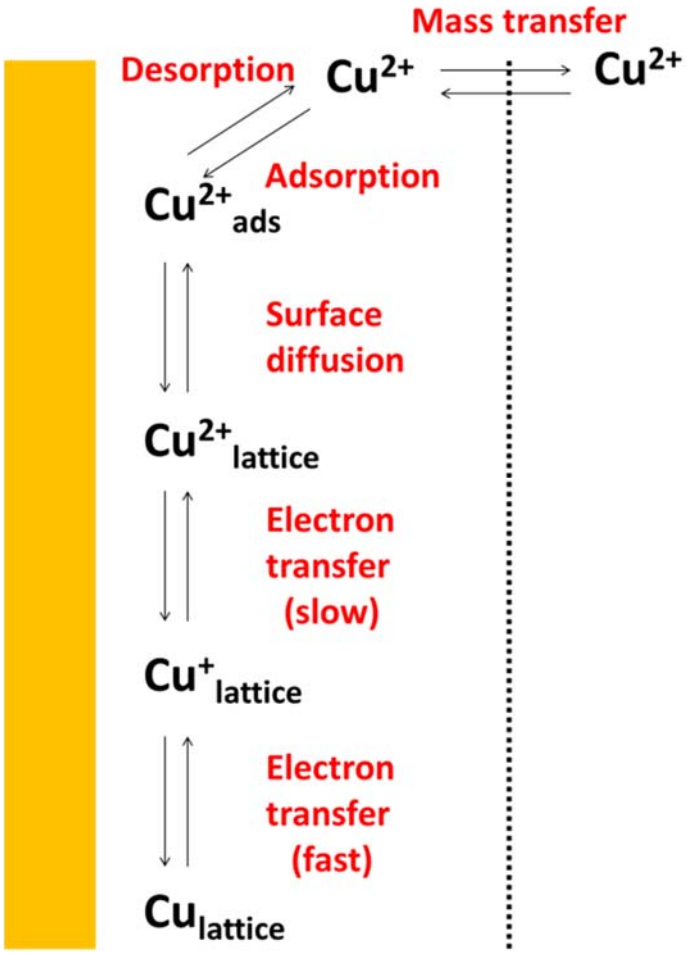


**Figure 1.3.** Schematic diagram of Cu electrodeposition.

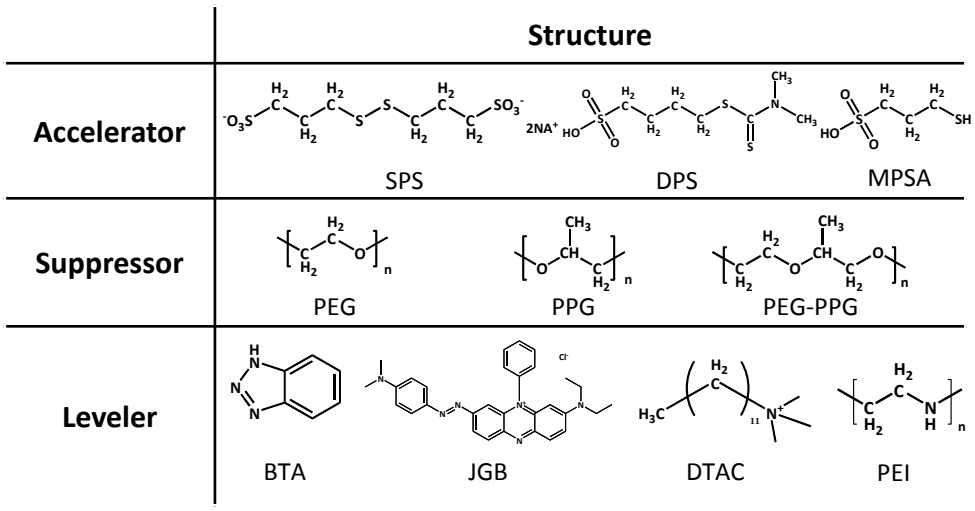


**Figure 1.4.** Conventional organic additives for Cu electrodeposition.

## 1.3. Superfilling

Generally, the growths of Cu in patterned substrates result in three types of cross-sectional profiles; subconformal, conformal, or superconformal profiles. Figure 1.5 shows the subconformal, conformal and superconformal deposits profiles. Subconformal profile results from the rapid Cu deposition on the trench top relative to trench bottom. It generally appears when the Cu deposition rate is governed by either the mass transfer or the solution resistance. Meanwhile, the conformal profile is formed when the deposition rates at the trench top and trench bottom are comparable, which results from the charge transfer-limited Cu deposition by the conformal adsorption of suppressor-type additives. Both subconformal and conformal profiles are improper for Cu interconnection because it has been known that the void and seam are vulnerable for electromigration.[2,3] Therefore, the superconformal profile is mostly preferred and it can be achieved by the proper combination of organic additives.

The Cu superfilling within a submicron trenches or microscale vias has been demonstrated by a number of different mechanisms including curvature enhanced accelerator coverage (CEAC),[11,12,54,55] convection dependent adsorption (CDA),[56-58] and negative differential resistance (NDR)[59-62] models. CEAC model is associated with the

bottom-up process of the submicron-sized trenches. For CEAC mechanism, the bottom-up filling of metal is explained with the increase of accelerator coverage at the bottom of features by the reduction of geometrical area. This phenomenon is quantified by Eq. 1.1 that shows the differential changes of accelerator coverage by the area reduction, displacement of suppressor, and the incorporation.[54]

$$\frac{d\theta_{SPS}}{dt} = \kappa v\theta_{SPS} + C_{SPS}k^{+}_{SPS}(1-\theta_{SPS}) - k^{-}_{SPS}(\theta_{SPS})^{q} \text{ (Eq. 1.1)}$$

Here, $\theta_{SPS}$ is the surface coverage of SPS, $\kappa$ is the curvature, $v$ is the interface velocity, $C_{SPS}$ is the concentration of SPS, $k^{+}_{SPS}$ is the adsorption coefficient of SPS on Cu surface, $k^{-}_{SPS}$ is the incorporation constant, and q is the power-law consumption exponent. The first term, $\kappa v\theta_{SPS}$, indicates the increase of SPS coverage by the reduction of geometrical area at the bottom of trench. The accelerator is rapidly accumulated in the bottom of trenches where the area reduction proceeds due to sidewall thickening. It leads to the higher Cu deposition rate at the bottom, followed by the bottom-up filling and bump formation, as described at Figure 1.6.[56]

Both CDA and NDR models are related to the bottom-up filling of micro-sized patterned features such as microvia or through silicon via (TSV). According to CDA model, the leveler-type additives adsorbs preferentially on the pattern tops where the diffusion length from bulk solution is relatively short. This has been demonstrated by

several electrochemical analyses where the electrodes with rotation is more polarized than that without rotation.[56-58]

NDR model is based on the local inhibition breakdown at the bottom of via, followed by the fast bottom-up filling until the inhibition layer is re-established. This was firstly suggested by Moffat et al who achieved bottom-up filling of Cu into TSV using tetronic 701 as single suppressor additives.[59] Further investigation in Au, Zn, and Ni systems has elucidated the detail mechanism and revealed critical variable to achieve the bottom-up filling without voids.[60-62]

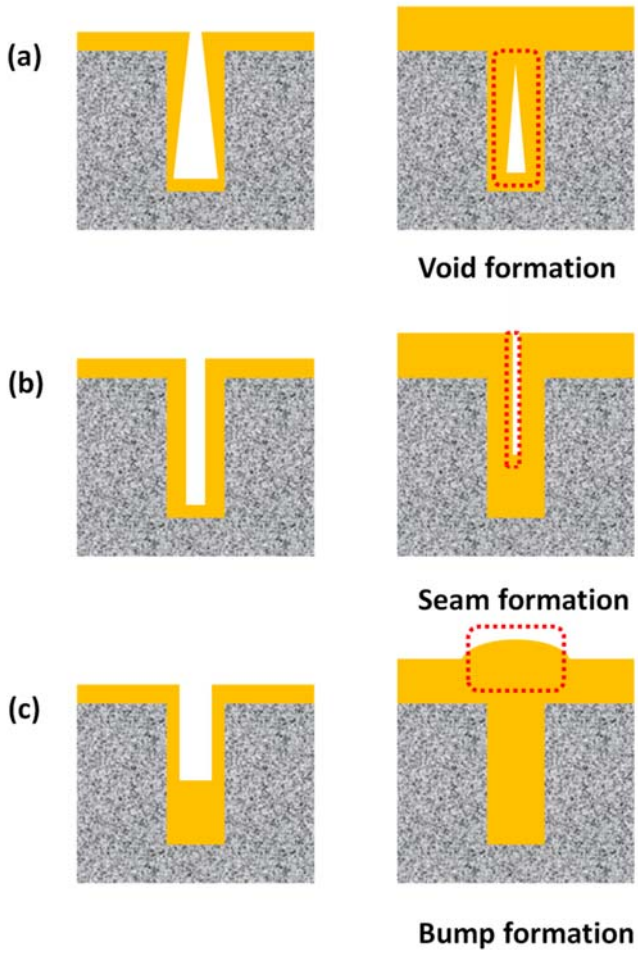


**Figure 1.5.** (a) Subconformal, (b) conformal, and (c) superconformal profiles of Cu at the initial and final stages of electrodeposition.

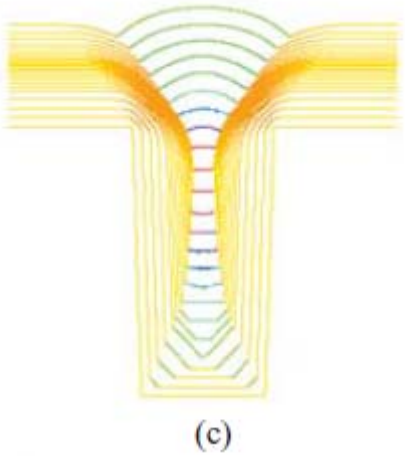


**Figure 1.6.** Superconformal film growth based on CEAC mechanism. (ref. 54)

## 1.4. Degradation of Plating Bath

As aforementioned at section 1.2, the organic additives are crucial factors affecting the morphology and the properties of Cu deposits. However, the organic additives are not stable in the electrolytic condition and they gradually decompose through various chemical/electrochemical side reactions.[63-80] As shown in Figure 1.7, the decomposition of organic additives leads to the degradation of bath performances, leading to defects in either trench filling or the subsequent chemical–mechanical planarization (CMP) process.[65,70] This chapter introduces the decomposition mechanisms of additive, especially focusing on the well-known two additives, SPS and PEG.

### 1.4.1. Decomposition of SPS

It has been known that the decomposition of accelerator occurs through at least three kinds of pathways; the reaction with dissolved oxygen molecular, the electro-oxidation reaction, and the dissociation reactions.[63-72] The reaction by oxygen molecular occurs under both open circuit and electrolytic conditions. Healy *et al.* has reported that SPS decomposes under open circuit condition by $Cu^{+}$, which comes from the

comproportionation-disproportionation reaction between $Cu^{2+}$ and metallic Cu, to form Cu-thiolate complex.[67] They also have suggested that the Cu-thiolate complex is unstable in the presence of $O_2$ and undergoes oxidation. Koh *et al.* has reported that the Cu-thiolate complexes can react with dissolved oxygen molecular to form inactive sulfonate compounds.[69] This reaction can take place even at the open circuit conditions when the Cu ion is present. However, the electrolytic condition can prompt the decomposition rate because of the rapid formation of cuprous ion at both cathode and anode.[63,64]

The electro-oxidation reaction occurs at the anode under electrolytic condition. This reaction yields 1,3-propane disulfonic acid (PDS) as breakdown products as described at Eq. 1.2.[63,68]

$$SPS^{2-} + 6H_2O \rightarrow 2PDS^{2-} + 10e^{-} + 12H^{+} \quad (\text{Eq. } 1.2)$$

Figure 1.8 presents the molecular structures of PDS. Since this reaction occurs at the surface of anode, the reaction rate is affected by the properties and surface area of anode. This reaction occurs more rapidly when the anode overpotential is high, therefore, the use of insoluble anode usually prompts the reaction 1.2.[63,81]

The third decomposition pathway is the dissociation of disulfide bonds on the cathode surface.[42,82-84] This reaction accompanies the formation of two MPS molecular, some of

which are recombined into SPS by the oxidation reaction with cupric ion. The redox cycle between SPS and MPS is presented at Eq. 1.3.[42,63,84]

$$2MPS^{-} + 2Cu^{2+} \leftrightarrow SPS^{2-} + 2Cu^{+} + 2H^{+} \quad (Eq.\ 1.3)$$

Here $Cu^{+}$ is further stabilized to form complex with residual MPS or $Cl^{-}$,[24] or rapidly oxidized by dissolved oxygen molecular.[85] Eq 1.3 is often used to explain the catalytic effect of SPS or MPS on Cu reduction process.[84]

### 1.4.2. Decomposition of PEG

Unlike to SPS, PEG have been shown to be stable under the open circuit conditions. However, under the electrolytic condition, PEG also decomposes and gradually fragments into low molecular units by either nucleophilic substitution reaction or the radical decomposition reaction.[73-77]

The nucleophilic substitution mechanism is based on the catalytic activity of $Cu^{2+}$ for the cleavage of ether bond at the cathode surface.[74] This reaction occurs via two-step; the nucleophilic substitution reaction followed by the successive unimolecular or bimolecular elimination reactions, as described Eqs 1.4-1.5.

$$R - CH_2 - CH_2 - O - CH_2 - CH_2 - R' + HNu:$$

$$\rightarrow R - CH_2 - CH_2 - Nu + R' - CH_2 - CH_2 - OH \text{ (Eq. 1.4)}$$

$$R - CH_2 - CH_2 - Nu \rightarrow R - CH = CH_2 + HNu \text{ (Eq. 1.5)}$$

Here, R and R' are the polymer chain and Nu is the nucleophile such as $Cu^{2+}$ ion. These reactions happen at the cathode and yield the vinyl ether- and alcohol-terminated PEG.[74]

The radical decomposition mechanism focuses on the reactivity of hydroxyl radical generated by the series of chemical reactions, as described at Eqs 1.6-1.14.[75,86,87]

$$2Cl^- \rightarrow Cl_2 + 2e^- \text{ (Eq. 1.6)}$$

$$Cl_2 + H_2O \leftrightarrow HOCl + Cl^- + H^+ \text{ (Eq. 1.7)}$$

$$HOCl \leftrightarrow H^+ + OCl^- \text{ (Eq. 1.8)}$$

$$6OCl^- + 3H_2O \rightarrow 2O_3Cl^- + 4Cl^- + 6H^+ + \frac{3}{2}O_2 + 6e^- \text{(Eq. 1.9)}$$

$$O_3Cl^- + H_2O \rightarrow O_4Cl^- + 2H^+ + 2e^- \text{ (Eq. 1.10)}$$

$$OCl^- + 2HOCl \rightarrow ClO_3^- + 2Cl^- + 2H^+ \text{ (Eq. 1.11)}$$

$$HOCl + OCl^- \rightarrow ClO\cdot + Cl^- + OH\cdot \text{ (Eq. 1.12)}$$

$$OH\cdot + OCl^- \rightarrow ClO\cdot + OH^- \text{ (Eq. 1.13)}$$

$$OCl\cdot + OCl^- + OH^- \rightarrow 2Cl^- + O_2 + OH\cdot \text{ (Eq. 1.14)}$$

The hydroxyl radical abstracts hydrogen from a methyl group in PEG to generate PEG internal radical and $H_2O$, followed by the C-O hydrolysis resulting in the breakdown of PEG, as shown in Figure 1.9.[75] Finally, low molecular weight (MW) PEG with aldehyde-, ethyl ether-, and vinyl ether-terminal groups are produced as byproduct.[75]

### 1.4.3. Factors influencing the decomposition of organic additives

The decomposition of organic additives depends on the several process factors such as the type of anode, oxygen level in plating bath, applied current/potential, or the presence of membrane. The insoluble anode usually results in fast decomposition of organic additives because of its high anodic potential stimulating anodic-oxidative decomposition reaction and the oxygen evolution.[63,73,81] The soluble Cu anode also has the potential risk for SPS decomposition, providing cuprous ion that drives the oxidation of SPS by dissolved oxygen.[67,69] Therefore, the phosphorous impurity has been used to diminish the release of cuprous ion into the electrolyte. The membrane to separate the cathodic and anodic spaces also has been widely applied in order to inhibit the decomposition and enlarge bath lifetime.[88]

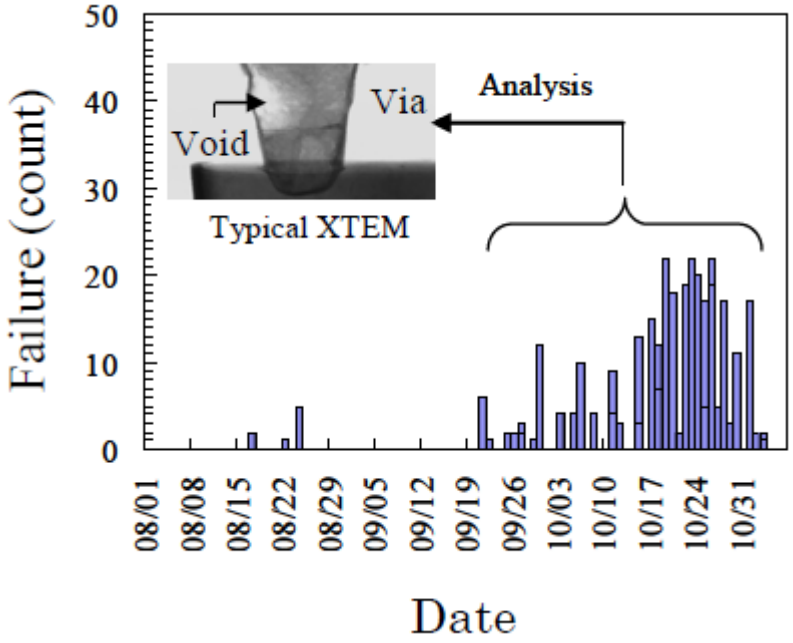


**Figure 1.7.** Number of failure in wafer electric test of interconnection. (ref. 70)

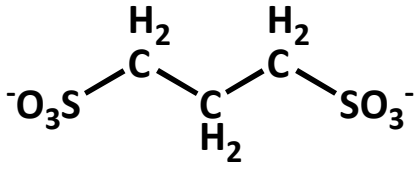


**Figure 1.8.** Molecular structures of PDS.

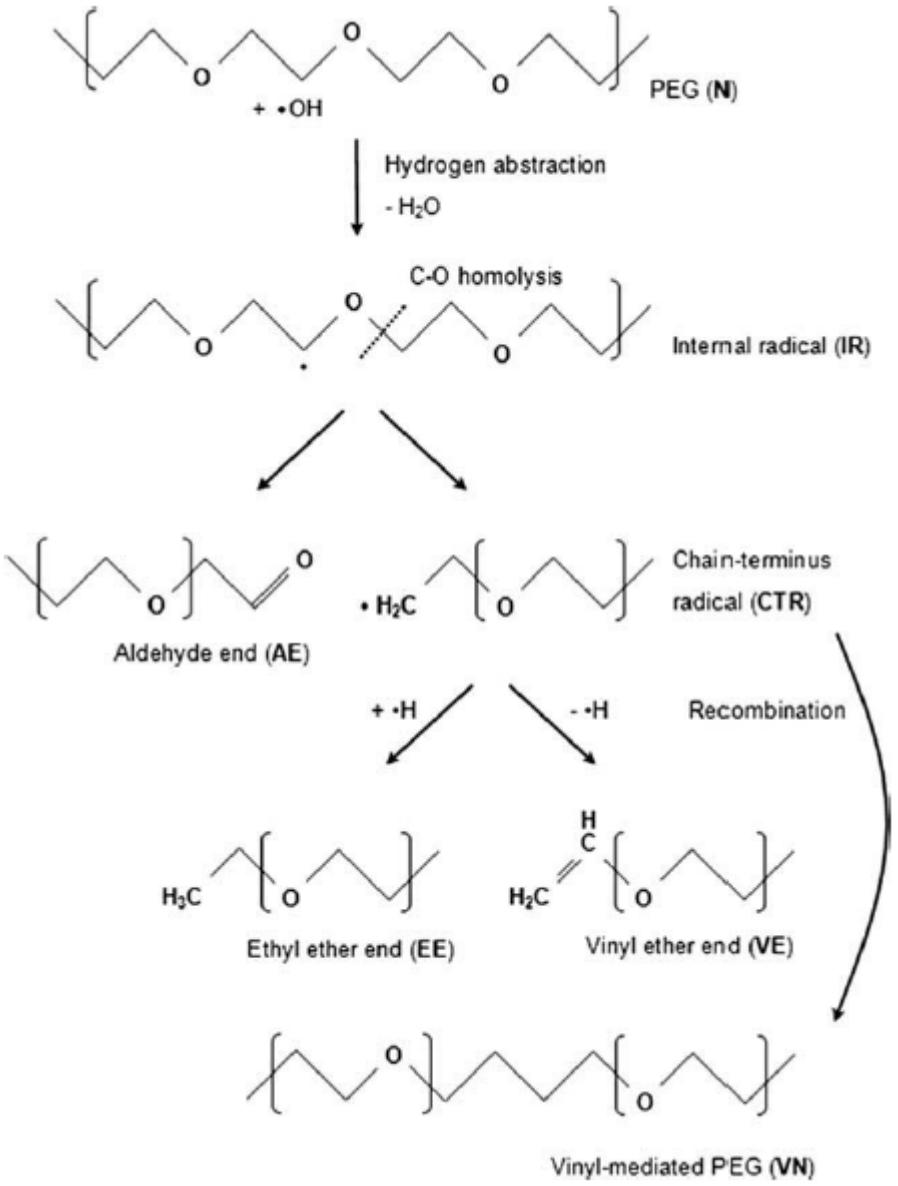


**Figure 1.9.** PEG decomposition pathway by electrolysis. (ref. 75)

## 1.5. Monitoring Methods for Additives Concentrations

Because of decomposition of the additives and the consequent degradation of the solution performance, concentration monitoring systems and additive feeding systems based on the measured concentrations are necessary to maintain the performance of the plating solution. Various methods have been developed for monitoring the additive concentrations, including the electrochemical techniques[89-95] such as cyclic voltammetry stripping (CVS)[89-93] and cyclic pulse voltammetry stripping (CPVS),[94] and the spectroscopic methods such as nuclear magnetic resonance (NMR),[63,73] UV-visible spectroscopy,[42,80] mass spectroscopy,[64,65,75,77] raman spectroscopy,[96] chromatography.[97,98] This chapter briefly introduces CVS method and the various spectroscopic tools to evaluate the concentrations of organic additives in Cu plating solution.

### 1.5.1. Cyclic voltammetry stripping

CVS has been regarded as the most powerful method for the determination of additives concentrations in Cu plating solution.[63,69,70,73,89-94] This method is based on the impact of organic additives on Cu reduction kinetics; the accelerator-type additives

increase the deposition rate, while the suppressor-type additives decrease the deposition rate. Several experimental techniques known as the dilution titration (DT), the modified linear approximation technique (MLAT) and the response curve (RC) are applied to determine the concentration of suppressor-, accelerator-, and leveler-type additives, respectively.[73,89,92,93]

(a) MLAT-CVS

MLAT-CVS is used for the analysis of accelerator concentration.[89,93] The standard procedure of MLAT-CVS is described at Figure 1.10; 1) evaluation of $Q_i$ from CVS analysis of the suppressor-saturated plating solution (the intercept solution); 2) evaluation of $Q_0$ after addition of the target solution (Cu plating solution to be analyzed) into the intercept solution; 3) evaluation of Q after addition of the accelerator standard solution into the intercept solution; 4) repetition of procedure 3 (2–3 times) to determine the increase in $\Delta Q/\Delta C_s$; and 5) evaluation of the accelerator concentration in the target plating solution from the Eq. 1.15.

$$C = \frac{Q_0 - Q_i}{\Delta Q/\Delta C_s} \frac{V_t + V_i}{V_t} \quad \text{(Eq. 1.15)}$$

Here $Q_i$, $Q_0$, and Q are the stripping charges of the intercept solution, the intercept solution mixed with the target solution, and the intercept solution after the addition of

accelerator standard solution, respectively. And, C is the concentration of accelerator in target plating solution, $C_S$ is the concentration of SPS in intercept solution after addition of accelerator standard solution, and C is the concentration of accelerator in target plating solution, $V_i$ is the volume of intercept solution, and $V_t$ is the addition volume of target solution, respectively.

Figure 1.11 presents the example Q-plot for the MLAT-CVS analysis of SPS, a representative accelerator. By SPS in target plating solution, $Q_0$ is higher than $Q_i$, and the value of $Q_0$-$Q_i$ converts to SPS concentration with comparing the charge increase by unit SPS concentration.

(b) DT-CVS

DT-CVS is typically used for the quantification of suppressor-type additives.[73,92,93] Figure 1.12 shows the standard procedure of DT-CVS analysis. In DT-CVS, the suppressor concentration in the target plating solution is determined by the following procedures; (1) measurement of the stripping charge ($Q_b$) by CVS of an additive-free plating solution, named as base solution, (2) addition of a small amount of the target plating solution into the base solution, (3) measurement of the normalized stripping charge ($Q/Q_b$) by CVS of the mixture, (4) repetition of procedures (2)-(3) until $Q/Q_b$

reaches an end point, referred to as the evaluation ratio which is a predetermined value for titration calculation, and (5) measurement of the volume of the target plating solution at the specific evaluation ratio. Above procedures are identically applied to the standard solution, in which the concentration of suppressor is tightly controlled to make the standard curve (calibration curve) of $Q/Q_b$ as a function of suppressor concentration. By comparing the volume of the target solution with that of a standard solution at the evaluation ratio, the suppressor concentration of the target solution can be determined, from the basic titration formula shown in Eqs. 1.16-1.18.

$$C = C'[\text{at evaluation ratio}] \quad (\text{Eq. } 1.16)$$

$$C = C' = \frac{V_p C_p}{V_b + V_p} = \frac{V_S C_S}{V_b + V_S} \quad (\text{Eq. } 1.17)$$

$$C_P = \frac{V_S C_S}{V_b + V_S} \frac{V_b + V_p}{V_P} \quad (\text{Eq. } 1.18)$$

In the above equation, C is the concentration of suppressor in (target + base) mixture, C' is the concentration of suppressor in (standard + base) mixture, $V_b$ is the volume of the base solution, $V_s$ is the volume of the standard solution at the evaluation ratio, $V_p$ is the volume of the target solution at the evaluation ratio, $C_s$ is the concentration of the suppressor in the standard solution, and $C_p$ is the concentration of the suppressor in the target solution.

Figure 1.13 shows typical Q-plot results of DT-CVS. By the suppressor species in the target plating solution, $Q/Q_b$ decreases with addition of target plating solution and finally reaches the evaluation ratio. The volume of target plating solution required to lower $Q/Q_b$ to evaluation ratio is compared to that of standard solution, and thereby the concentration of suppressor can be eventually evaluated.

(c) RC-CVS

The RC-CVS method is typically used for the determination of leveler-type additive in Cu plating solution.[93] In RC-CVS method, the decrease in stripping charge by leveler species is measured, which sequentially converts into leveler concentration in plating solution. Standard procedure of RC-CVS is described at Figure 1.14. Preliminarily, the standard calibration curve (also named as RC curve) depicting the relation between leveler concentration and normalized stripping charge was obtained with following steps; 1) preparation of suppressor- and accelerator-saturated Cu plating solution called as base solution, 2) measurement of stripping charge, 3) addition of leveler standard solution into base solution, 4) measurement of stripping charge, 5) repetition of procedure 3-4 (for 5-10 times).

Figure 1.15 presents the typical example of RC curve showing the linear relation between $Q/Q_b$ and leveler concentration. With this calibration plot, the leveler concentration of unknown sample is can be accurately determined.

### 1.5.2. Spectroscopy analysis

Various merits of CVS including the accuracy, the simplicity, and the time requirement for analysis has allowed its wide applications in the various industrial fields. However, the drawback of CVS has been pointed out, including the incapability of the analysis of breakdown products and the signal interference by breakdown products.[70,73] The detection and quantification of byproduct conventionally relies on the spectroscopic methods such as UV-visible spectroscopy,[42,80] $^1$H-NMR,[63,73] and mass spectroscopy.[64,65,75,77] For the application of spectroscopy, the pretreatment of solution sample is necessarily carried out in order to extract organic species from plating bath. Examples of pretreatment include solid phase extraction (SPE)[68,74] and liquid-liquid extraction.[78,79] Various applications of spectroscopic methods on the monitoring of plating solution can be found elsewhere.[63-66,73,74,96-99]

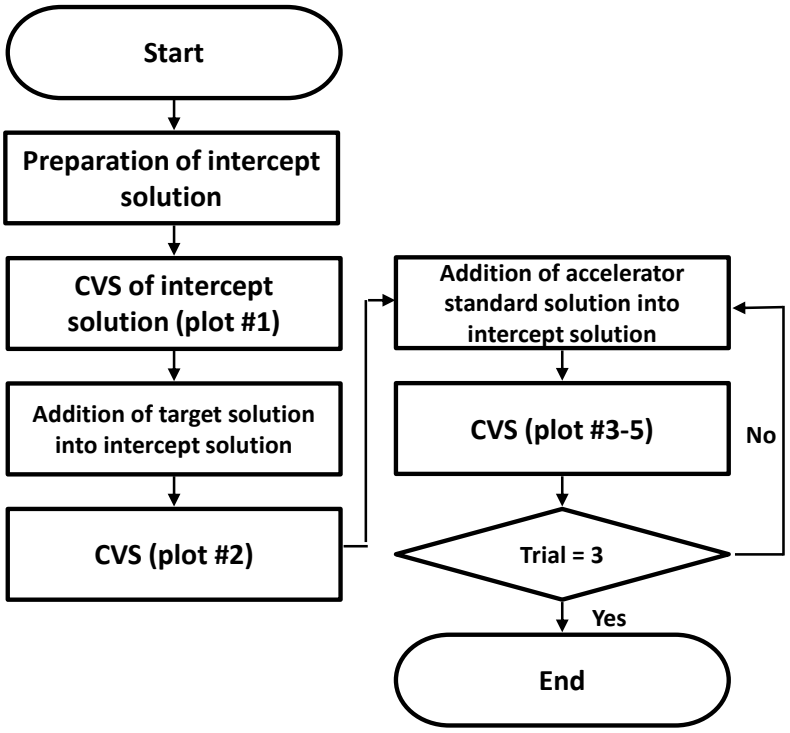


**Figure 1.10.** Standard procedures of MLAT-CVS.

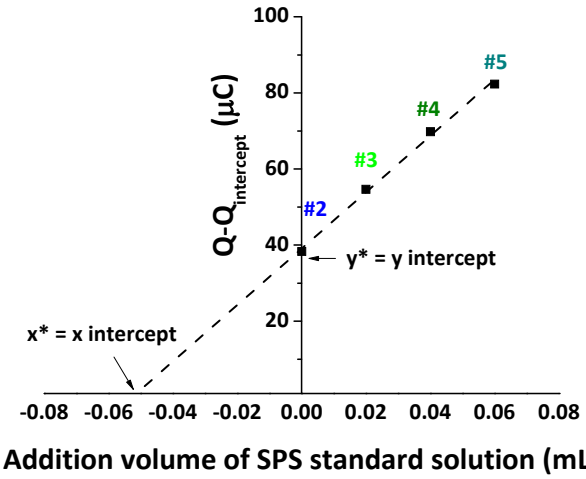


**Figure 1.11.** Example Q plot for MLAT-CVS analysis of accelerator. The numbers indicate the charges obtained from corresponding unit procedures in Figure 1.9. (see Figure 1.9)

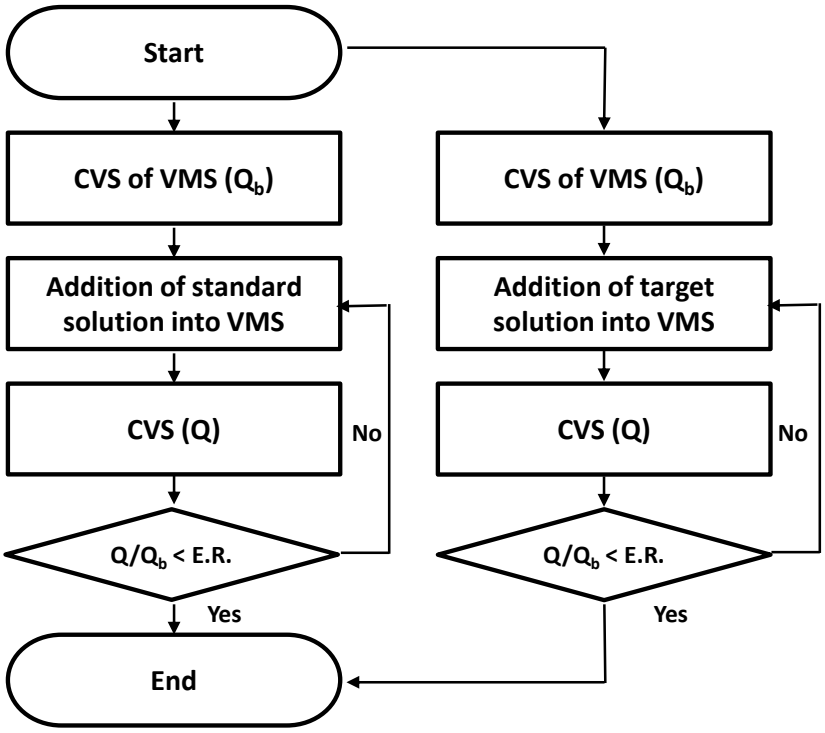


**Figure 1.12.** Standard procedures of DT-CVS.

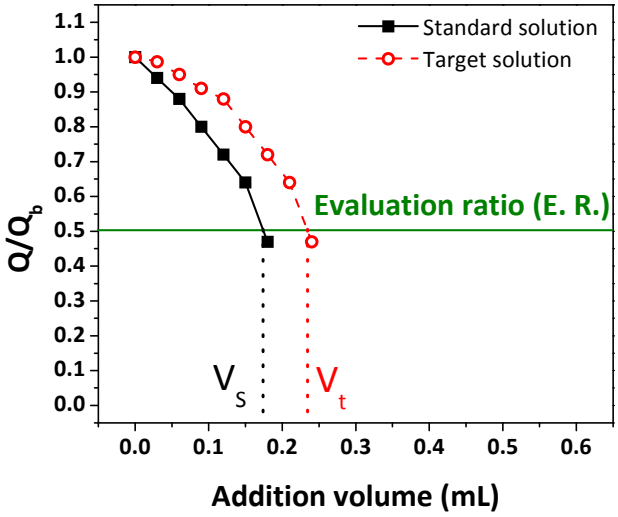


**Figure 1.13.** Example Q plot for DT-CVS analysis of suppressor.

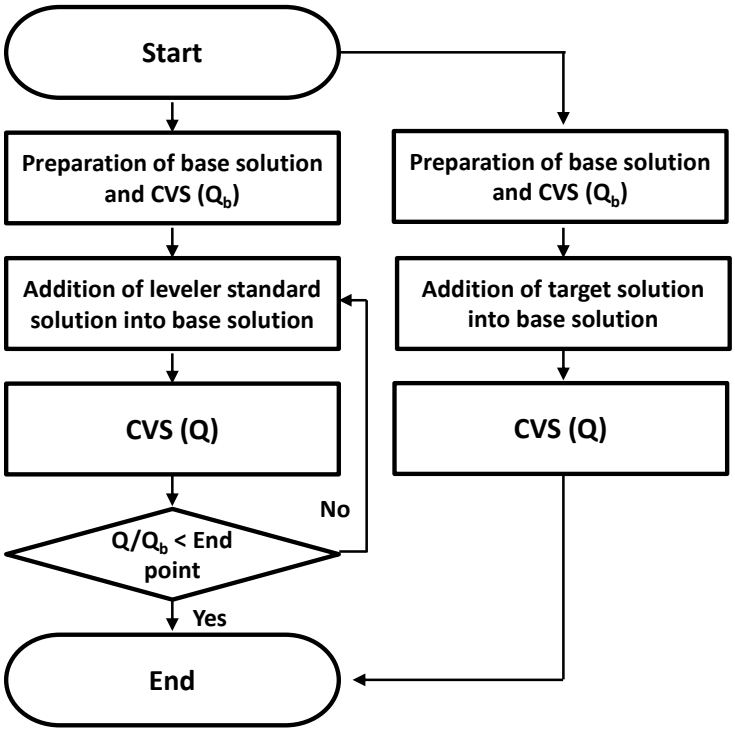


**Figure 1.14.** Standard procedure of RC-CVS.

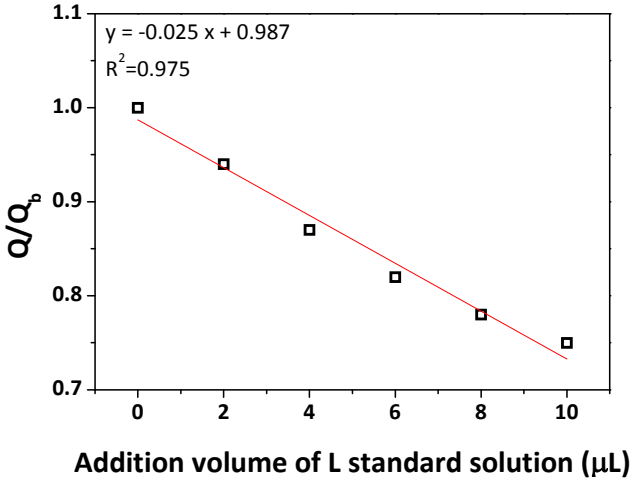


**Figure 1.15.** Example RC plot for RC-CVS analysis of leveler.

## 1.6. Purpose of This Study

Although the significant efforts are continuously made to maintain the concentration of organic additives in Cu plating bath, the bath is eventually unusable after long time of operation due to the impacts of additive breakdown products. The breakdown products might either adsorb on Cu surface or form a complex with $Cu^{2+}$ ion, thereby deteriorating the filling capability of plating bath and changing the properties of Cu film. Besides, the additives breakdown products might disturb the monitoring results if their signals are overlapped with their parent additives. For example, MPS, one of the breakdown products from SPS decomposition, might disturb the MLAT-CVS results of SPS concentrations because both MPS and SPS result in the acceleration effect for Cu reduction. Considering those aspects, it is necessary to develop the advanced monitoring methods that enable to analyze not only the parent additives but also their breakdown products.

This study comprehensively describes the additives decomposition phenomenon, the influences of breakdown products, and the development of advanced monitoring methods for accurate evaluation of bath performance. In particular, the decompositions of SPS and PEG-PPG are focused on.

In chapter 3, the influences of breakdown products from SPS decomposition are investigated by analyzing the electrochemical behavior, Cu film properties and the filling capability. At first, the breakdown products of SPS are verified using in-situ $^{1}$H-NMR analysis. The analyzed breakdown products are MPS and PDS, and the subsequent experiments revealed their effects on the filling capability and CVS monitoring results.

In chapter 4, a two-step CVS analysis was suggest for the individual measurement of SPS and MPS concentrations in acidic Cu plating solution. The suggested method is based on an assumption that the interconversion between SPS and MPS is strongly influenced by the solution pH because oxidation of MPS into SPS accompanies the formation of a proton (Eq. 1). In the first step, we determined the total accelerator concentration (conc. of SPS + 1/2 conc. of MPS) using the MLAT-CVS method, after oxidizing MPS into SPS by adjusting the Cu plating solution pH. Subsequently, in the second step we determined the conversion ratio from the result that acceleration by MPS was more effective than that by SPS. We finally obtained the concentrations of SPS and MPS separately using the values of the total accelerator concentration and conversion ratio.

In chapter 5, the decomposition of PEG-PPG during Cu electrodeposition and the influences of MW reduction are studied. The breakdown product of PEG-PPG was

examined with the spectroscopic methods including $^{1}$H-NMR, matrix assisted laser desorption ionization time of flight (MALDI-TOF), and gel permeation chromatography (GPC). The influence of breakdown products was also studied by analyzing the electrochemical behavior and performances of aged bath.

# Chapter II. Experimental

## 2.1. Aging Experiment

### 2.1.1. Aging of SPS

Figure 2.1 illustrates the experimental apparatus used in this study. Individual additives was intentionally decomposed by continuous electrodeposition under conventional plating conditions, referred to as the “aging experiments” throughout this paper.

The SPS aging experiments consisted of the following procedures: (1) electrodeposition with a suppressor-free electrolyte for 30, 60, 90, 120, and 180 min, (2) supplement of the consumed $CuSO_4$ and NaCl, and (3) collection and analysis of the plating solution. Electrodeposition for the aging experiment was carried out at a 10 $mA/cm^2$ current density at 25°C. The plating solution consisted of 0.56 M $CuSO_4$, 1.47 M $H_2SO_4$, 1.67 mM NaCl, and 35 μM SPS. Cu foil with an active area 70 $cm^2$ was used as the working electrode and either $Ir/IrO_x$ or Cu plates were used as counter electrodes. The total volume of solution in the bath was 1.5 L. The bath was equipped with a bubbler

to enhance the mass transport of cupric ions. After the experiments, some of the plating solution was extracted for $^{1}$H-NMR measurements.

Since both cupric and chloride ions are consumed during aging experiment, they were periodically supplied every 30 min. The supplementing of $CuSO_4$ was based on the amount of charge passed, whereas the supplementing of NaCl was based on measurements by 'Chloride Concentration Analyzer for Acidic Plating Solution' from Jungdo21 Co. It should be noted that the $Na^+$ added to the electrolyte during the replenishment can also affect the additive chemistry, though the detailed chemistry is not fully understood up to now.

2.1.2. Aging of PEG-PPG

PEG-PPG (average MW: 900 Da) was aged using electrodeposition with a current density of 40 mA/cm$^2$ in an acidic plating solution consisting of 0.56 M $CuSO_4$, 1.47 M $H_2SO_4$, 1.67 mM NaCl, and 1400 μM PEG-PPG. Cu foil with an active area 70 cm$^2$ was used as the working electrode and either Ir/$IrO_x$ or Cu plates were used as counter electrodes. The volume of electrolyte in the cell was 1.5 L. The ratio of cathodic surface area per electrolyte volume was about 0.047 cm$^{-1}$. The bubbler was equipped to enhance the mass transport of Cu ions, and the temperature of electrolyte was precisely controlled

to remain at 39 °C. Since both cupric and chloride ions were consumed during electrodeposition, these were periodically supplied every 3 hr based on the amount of charge passed and measurement done by the chloride concentration analyzer for acidic plating solutions (Jungdo21 Co.) The decomposition rate of PEG-PPG under these experimental conditions was much faster than the conventional plating cell where the protections against decomposition were well-installed.

The aging experiment comprised a series of conventional electrodeposition, measurement of PEG-PPG concentration using the DT method of CVS, and addition of an adequate supplement of fresh PEG-PPG into the electrolyte. Therefore, the concentrations of PEG-PPG in fresh and aged plating solutions were comparable, while the amount of by-products increased as the duration of aging increased. Cu electrodeposition was performed using the same conditions as described in the aforementioned experiments. The CVS was performed at 15 hr, 25 hr, and 35 hr intervals from the start of the electrodeposition for the measurement of PEG-PPG concentration. Then, fresh PEG-PPG was supplied to the electrolyte to maintain the concentration of PEG-PPG.

The DT methods of CVS (797 VA Computrace, Metrohm) were used to determine the concentration of PEG-PPG in the electrolyte. The Pt rotating disk electrode (RDE),

insoluble anode, and Ag/AgCl (3 M KCl) were used as working, counter and reference electrodes, respectively. The scanning swept from 2.0 V to -0.2 V with a scan rate of 100 mV/s and a rotation of 1000 rpm. The evaluation ratio of the DT method was fixed at 0.6. All the aforementioned parameters were previously optimized in our system.

### 2.1.3. Aging of full solution

Cu plating bath containing 0.25 M $CuSO_4$, 1.0 M $H_2SO_4$, 1.0 mM NaCl, 50 μM SPS and 360 μM PEG-PPG are aged by electrodeposition at 10 mA/$cm^2$. Cu foil with an active area 70 $cm^2$ was used as the working electrode and either Ir/$IrO_x$ or Cu plates were used as counter electrodes. The temperature of electrolyte was precisely controlled to remain at 25 °C. Both cupric and chloride ions were periodically supplied every 30 min based on the aforementioned methods.

## 2.2. Effect of Breakdown Products

### 2.2.1. Solution extraction

Individual additives were extracted from the acidic plating solution through the following steps: (1) addition of 10 ppm saccharin as an internal standard for the normalization of $^{1}$H-NMR peaks; (2) neutralization of the plating solution with the addition of 8 M KOH solution; (3) addition of pure ethanol in the ratio of 4 (solution) : 6 (ethanol) to precipitate the inorganic compounds; (4) filtering and evaporation to remove the precipitator and water; and (5) dissolution of the residue in $D_2O$. A final solution containing additives and saccharin (internal standard) was investigated using $^{1}$H and $^{13}$C-NMR (600 MHz, Bruker), MALDI-TOF (Voyager-DETM, Applied Biosystems Inc.), and GPC (HPLC UltiMate 3000 RI system, Thermo).

2.2.2. Electrochemical analysis

<Aging effect of SPS>

Cyclic voltammetry (CV) was performed in order to study the influences of SPS decomposition and the by-products from it on the electrochemical behavior of the plating solution. For CV measurements, a Cu RDE with 300 rpm rotation was used as the working electrode while the counter and the reference electrodes were the same as those used in the feature-filling experiments. The scan rate was 10 mV/s. The first cycle of scan was used to compare the electrochemical behavior of plating solution.

<Aging effect of PEG-PPG>

Chronoamperometry (CA) was performed in previously prepared electrolytes for clarifying the effect of aging. 35 μM SPS was additionally added to those electrolytes to investigate the competitive adsorption between SPS and PEG-PPG. The CA was carried out with a Cu RDE, 99.9 % Cu wire, and Ag/AgCl (saturated KCl) as the working, counter, and reference electrodes. The rotating speed and geometric area of RDE were 300 rpm and 0.1258 $cm^2$, respectively. The applied potentials were fixed at -0.1 V, -0.15 V and -0.2 V for 150 s.

2.2.3. Analysis of solution performance

<Aging effect of SPS>

After aging the plating solution for 30, 60, 90, 120, and 180 min (i.e., continuous operation without supplement of SPS), analysis of the feature-filling performance was carried out at 10 $mA/cm^2$ at 25°C. PEG–PPG (360 μM, Mw: 900) was then added to the solution as the suppressor. Patterned Cu wafers with a 55-nm-wide trench having an aspect ratio of 6 and a multilayer structure of physical vapor deposited (PVD) Cu (7.5 nm)/PVD Ta (6 nm)/PVD TaN (1.5 nm), a Cu wire (99.9% pure) and a Ag/AgCl (sat.

KCl) electrode were used as the working, the counter and the reference electrodes, respectively.

The effects of the dissociation by-product, PDS, on the properties of Cu films were studied by electrodeposition of Cu in electrolyte consisting of 0.56 M $CuSO_4$, 1.47 M $H_2SO_4$, 1.67 mM NaCl, 360 μM PEG-PPG, 35 μM SPS, and various concentrations of PDS. Blanket Cu wafer with the structures of PVD Cu (40 nm)/PVD Ta (7 nm)/SiO2 was used as a working electrode with the same counter and reference electrodes used in the feature filling. Cu films were deposited with 10 $mA/cm^2$ current density for 500 s. The deposited Cu films were examined by X-ray diffraction (XRD, D8-Advance, Bruker), field-emission scanning electron microscopy (FESEM, S-4800, Hitachi), four-point probe (CMT-SR1000N, Chang Min Tech.). The impurity level of Cu films was obtained by elemental analyzer (Flash EA 1112, Thermo Electron Corporation) after the deposition of Cu for 2400 s on the 10 μm-thick Cu foil. The other conditions were the same as mentioned above.

The influences of another breakdown product, MPS, was explored with a pattern filling experiment of the target solutions having different compositions of SPS and MPS. The solution for pattern filling was composed of target solutions and 90 μM PEG (MW: 3400). Electrodeposition was carried out at room temperature with 10 $mA/cm^2$ current

density. Cu pattern wafers with the structure of Cu seed (50 nm at the bottom of the trench, 15 nm at the sidewall)/Ta (30 nm at the bottom, 15 nm on the sidewall)/SiO2 were used as the working electrodes. A Cu rod (99.9% purity) and Ag/AgCl [sat. KCl] were used as the counter and reference electrodes, respectively.

<Aging effect of PEG-PPG>

Cu films were deposited in the previously prepared electrolyte to investigate the effect of solution aging on the properties of Cu films. Blanket Cu wafers with the structures of PVD Cu (40 nm)/PVD Ta (7 nm)/SiO2 were used as working electrodes. The Cu films were deposited with a current density of 10 mA/cm2 for 500 s. The counter and reference electrodes were the same as that used in CA experiments. The deposited Cu films were examined by X-ray diffraction (XRD, D8-Advance, Bruker), field emission scanning electron microscopy (FESEM, S-4800, Hitachi), and a four point probe (CMT-SR1000N, Chang Min Tech.).

## 2.3. CVS Analysis

### 2.3.1. Electrolyte

Cu plating solutions, referred to as the target solution, intercept solution #1 (IS1), and intercept solution #2 (IS2), were used in this experiment. Target solutions comprised 0.25 M $CuSO_4$, 1.0 M $H_2SO_4$, 1 mM NaCl, 0–50 μM SPS, and 0–100 μM MPS. IS1 was a base solution for conventional MLAT-CVS analysis with a composition of 0.125 M CuSO4, 0.5 M $H_2SO_4$, 1.0 mM NaCl, and 1400 μM PEG (MW: 3400). IS2 was a pH-modified IS1 consisting of 0.125 M $CuSO_4$, 0.5 M $H_2SO_4$, 1.0 mM NaCl, 1400 μM PEG (MW: 3400), and 1.2 M KOH. The composition of IS1 was optimized for conventional MLAT-CVS, while IS2 was optimized for the two-step CVS.

2.3.2. MLAT-CVS

CVS analysis was aimed at observing the electrochemical behavior of the solutions and measuring the concentrations of accelerators. CVS plots were obtained using either IS1 or IS2 as the base electrolyte. Prior to the CVS measurement, 0–4.5 μM SPS and 0–9 μM MPS were added into IS1 or IS2. A Pt RDE with a rotating speed of 2000 rpm, a Pt rod, and Ag/AgCl (3 M KCl) were used as the working, counter, and reference electrodes, respectively. A scan rate of 0.1 V/s and a vertex potential of -0.3 V were constantly applied.

Conventional MLAT-CVS analysis of the SPS concentration was carried out using the following procedures: 1) evaluation of $Q_i$ from the CVS analysis of IS1 (volume of IS1: 50 mL); 2) addition of diluter (1.0 mM NaCl) into the target plating solution at a 1:1 (v/v) ratio; 3) evaluation of $Q_0$ after addition of the diluted target solution into IS1 (addition volume: 5 mL); 4) evaluation of Q after addition of the standard SPS solution (5000 μM SPS) into IS1 (addition volume: 0.05 mL); 5) repetition of procedure 4 (3 times) to determine $\Delta Q/\Delta C_S$; and 6) evaluation of the SPS concentration of the target plating solution from $(Q_0\text{-}Q_i)/(\Delta Q/\Delta C_S)$.Eq. 1.15.

However, our modified MLAT-CVS analysis consisted of a two-step methodology. The first step was carried out to evaluate the total accelerators concentration with the following procedures: 1) evaluation of Qi from the CVS analysis of IS2 (volume of IS2: 50 mL), 2) addition of pH adjuster (2.4 M KOH, 1.0 mM NaCl) into the target plating solution with a 1:1 (v/v) ratio, 3) evaluation of $Q_0$ after addition of the pH-adjusted target plating solution into IS2 (addition volume: 5 mL), 4) evaluation of Q after addition of the SPS standard solution (5000 μM SPS) into IS2 (addition volume: 0.05 mL), 5) repetition of procedure 4 (3 times) to determine $\Delta Q/\Delta C_S$, and 6) evaluation of the SPS concentration in the target plating solution from the value of $(Q_0\text{-}Q_i)/(\Delta Q/\Delta C_S)$.

The second step was aimed at measuring the conversion ratio: 1) evaluation of $Q_i$ from the CVS analysis of IS1 (volume of IS1: 50 mL), 2) addition of diluter (1.0 mM NaCl) into the target plating solution with a 1:1 (v/v) ratio, 3) evaluation of Q after addition of the diluted target plating solution into IS1 (addition volume: 0.5–2 mL), 4) repetition of procedure 3 (3–5 times) to obtain the relation between $Q/Q_i$ and addition volume of the target plating solution, 5) evaluation of the slope for the calculation of $(\Delta Q/Q_i)/\Delta C_T$, where $C_T$ is the total accelerator concentration, and 6) evaluation of the conversion ratio using the pre-determined calibration curve. The conditions of all electrochemical experiments, including the electrodes, scan rate, and vertex potential, were as described above.

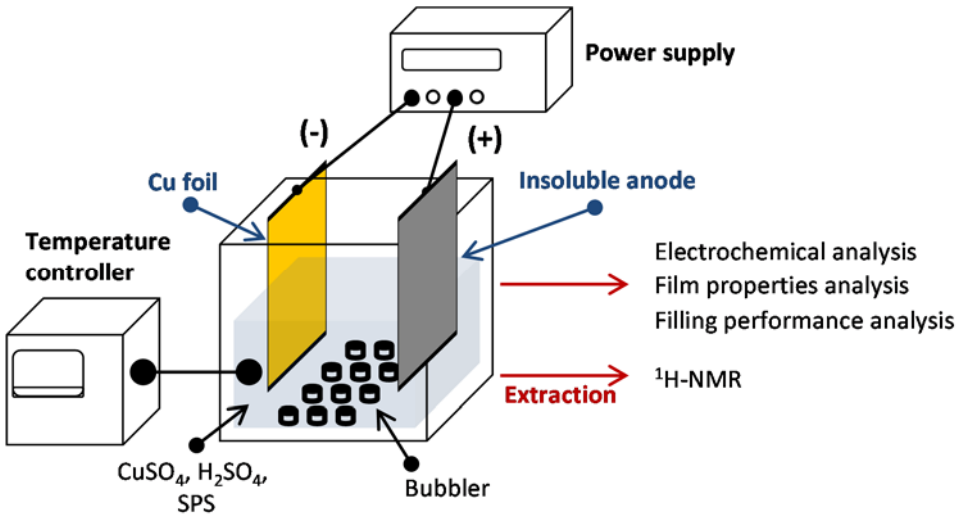


**Figure 2.1.** Schematic diagram of aging experiment.

# Chapter III. Decomposition of SPS

## 3.1. Decomposition of SPS

SPS, a dimer of MPS, has been regarded as one of the essential components for achievement of superfilling. The role of SPS for superfilling is to accelerate the deposition rate at the trench bottom more than the deposition rate at the trench top via the CEAC mechanism described at chapter 1. Acceleration by SPS has been explained by the competitive adsorption theory[11,12,54,55] or by the catalytic action caused by the reduction of cupric ions.[42,84] In the competitive adsorption theory, acceleration is regarded as a recovery of the deposition rate previously suppressed by the polyethylene glycol (PEG)-Cl inhibition layer, and recovery occurs through the displacement of the PEG-Cl layer with SPS.[11,12,54,55] A recent study revealed that the acceleration is a result of the dissociative adsorption of SPS with displacement of the well-ordered Cl- layer.[82,83] MPS, a dissociated product of SPS, reconverts to SPS with reduction of cupric ions, as described in Eq. 1.3.

As mentioned aforehead at chapter 1, SPS decomposes into MPS and PDS by various chemical/electrochemical reactions. It is evident that the decomposition of SPS degrades

the performances of plating solutions, leading to defects in either trench filling or the subsequent chemical-mechanical planarization (CMP) process. However, the detail failure mechanism including the roles of breakdown products has not been reported yet.

Therefore, in this chapter, the influences of breakdown products from SPS decomposition are examined in detail. The byproducts from SPS decomposition are characterized using $^{1}$H-NMR, which is further used to analyze the changes in the concentrations of active and inactive organics in the plating bath. Then, the impacts of byproducts are analyzed.

Experiments were performed to confirm the differences in filling performance as a function of aging time. Figures 3.1(a)–(c) show that the plating solution had good filling performance up to a aging time of 60 min. Voids appeared after 90 min [Figure 3.1(d)], accompanied by changes in filling profiles from superconformal to conformal [Figure 3.1(f)] because of SPS decomposition during electrodeposition, as reported by Wang *et al.* and Koh *et al.* who observed that the voids were formed during via filling when the charge passing through the circuit exceeded 15 Ah/L and 25 Ah/L, respectively.[66,70] These values are significantly higher than those obtained through our experiments (0.93 Ah/L). This difference can possibly be ascribed to processing factors such as the sizes of

features, the presence of other chemical components, or the replenishment of additives using the CVS method.

Figure 3.2 shows the CV results of the fresh and aged solutions. The presence of fresh SPS resulted in typical hysteresis, which is associated with the competitive and the potential dependent adsorption behavior of SPS and PEG–PPG on the Cu surface.[11,12,54,55] As the degradation time increased, the current density in the forward scan decreased slightly, whereas that in the backward scan declined significantly after initial preservation until 90 min. Both the decrease of forward current density and disappearance of hysteresis indicated the decrease of active accelerating compounds in the plating solution. The hysteresis curve finally disappeared after 180 min, at which point the filling profile completely changed from superconformal to conformal [Figure 3.1(f)].

$^{1}$H-NMR analyses were carried out to identify the chemical components of the plating solutions aged for 0, 30, 60, 90, and 180 min. Figure 3.3 shows that SPS initially had three characteristic peaks at 2.18 ppm, 2.89 ppm, and 3.06 ppm with an area ratio of 1:1:1 (denoted as S1, S2, and S3, respectively). It was noticeable that the relative intensity of the 2.89 ppm triplet (S2) decreased as the aging time increased. This decrease was associated with the dissociation of the SPS disulfide bond on the Cu surface. This reaction resulted in the formation of two MPSs, whose peaks appeared at 2.03 ppm (M1),

2.48 ppm (M2), 3.05 ppm (M3). Another byproduct from the decomposition of the disulfide bond was the PDS observed at 2.18 ppm (P1) and 3.06 ppm (P2) with the area ratio of 1:2. The formation of MPS and PDS are already well known as byproducts of SPS decomposition during Cu electrodeposition. Lee *et al.* and Wang *et al.* observed MPS and PDS in aged plating solutions by means of mass spectroscopy and each suggested a mechanism of SPS decomposition using density functional theory.[64,66] They proposed that PDS was formed from the oxidation reaction of SPS catalyzed by the metallic Cu surface. Koh *et al.* observed that oxygen purging into the plating solution accelerated the decomposition of SPS.[69]

Before quantitative analysis of each additive, the $^{1}$H-NMR spectrums of the power and standard samples (additives after pretreatment from non-electrolyzed bath) of SPS-related compounds were obtained in order to check the stability of each additive during pretreatment. As shown in Figure 3.4 (a) and (b), SPS and PDS were stable throughout the pretreatment. However, most of MPS changed to SPS during the pretreatment step by the oxidative dimerization reactions. No evidence on the oxidation of MPS to PDS was observed. The results of Figure 3.4 (a) and (b) imply that some portion of MPS formed by the decomposition of SPS was converted back to SPS during the pretreatment step.

Therefore, the amounts of SPS and MPS in the samples subjected to NMR were different with the actual amounts of them right after the aging step.

The concentrations of active accelerating compounds (SPS+1/2MPS), PDS, and overall compound (SPS+1/2MPS+1/2PDS) were obtained by comparing the relative area of each peak with 10 ppm saccharin, as shown in Figure 3.5. The concentrations of active accelerating compounds were expressed based on the following considerations. First, two MPS molecules could be reconverted to one SPS molecule by an oxidative dimerization reaction with the reduction of cupric ions. It was essential step of the acceleration because it aided the reduction of $Cu^{2+}$ to $Cu^{+}$, the rate determining step in Cu electrodeposition. Furthermore, the individual determination of MPS and SPS concentrations had little meaning due to the interconversion reaction of MPS to SPS during the pretreatment step (Figure 3.4 (a), (b)). As shown in Figure 3.5, as the aging time increased, the concentration of active accelerating compounds steadily decreased whereas the PDS concentration increased. The concentration of overall compounds (SPS+1/2MPS+1/2PDS) steadily decreased due to the incorporation of additives into the growing Cu films. The total incorporated amount of SPS and its by-products was 14.7 μM after 180 min of aging test in our conditions. A possible mechanism of SPS decomposition is illustrated in Figure 3.6. One significant reaction is the dissociation of

the SPS disulfide bond on the Cu surface, producing two MPS molecules. Meanwhile, SPS could be sequentially oxidized through a reaction with $O_2$ and $H_2O$, leaving PDS and MPS as the byproducts. PDS seemed to be most stable, and it remained in the plating solution without any further chemical reactions.

Considering the initial and final product presented in Figure 3.3, the net reactions of SPS decomposition can be expressed by following equation:

$$SPS^{2-} + O_2 + H_2O \rightarrow PDS^{2-} + MPS^{-} + H^{+} \text{ (oxidation by molecular oxygen) (Eq. 3.1)}$$

$$SPS^{2-} + 6H_2O \rightarrow 2PDS^{2-} + 10e^{-} + 12H^{+} \text{ (anodic-oxidation) (Eq. 3.2)}$$

$$SPS^{2-} + \text{oxidant (dissolved } O_2\text{, anode)} \rightarrow 2PDS^{2-} \text{ (overall) (Eq. 3.3)}$$

Since either the decrease in active species (SPS) or the increase in breakdown products (MPS, PDS) can deteriorate filling capability, the effects of SPS, MPS, and PDS will be discussed in the next chapter.

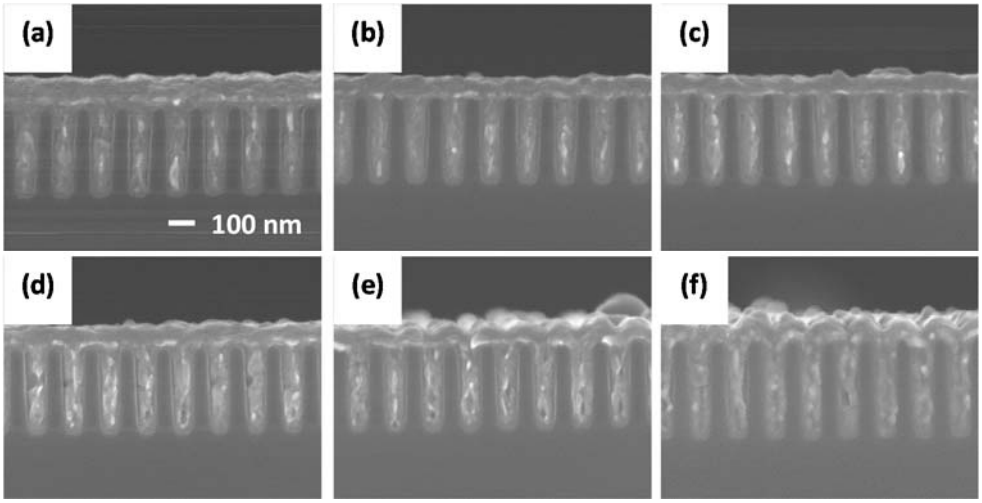


**Figure 3.1.** Filling performance of plating solutions aged for (a) 0 min, (b) 30 min, (c) 60 min, (d) 90 min, (e) 120 min, and (f) 180 min. 360 μM PEG–PPG was added before the experiments.

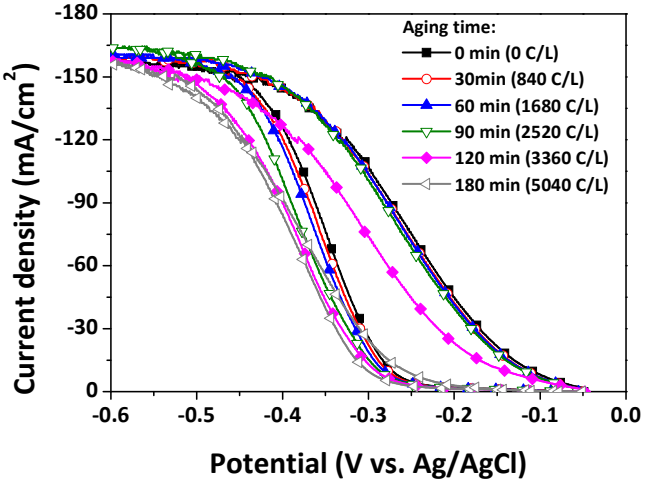


**Figure 3.2.** CV voltammograms of plating solutions aged for 0, 30, 60, 90, 120, and 180 min. 360 μM PEG–PPG was added before the experiments.

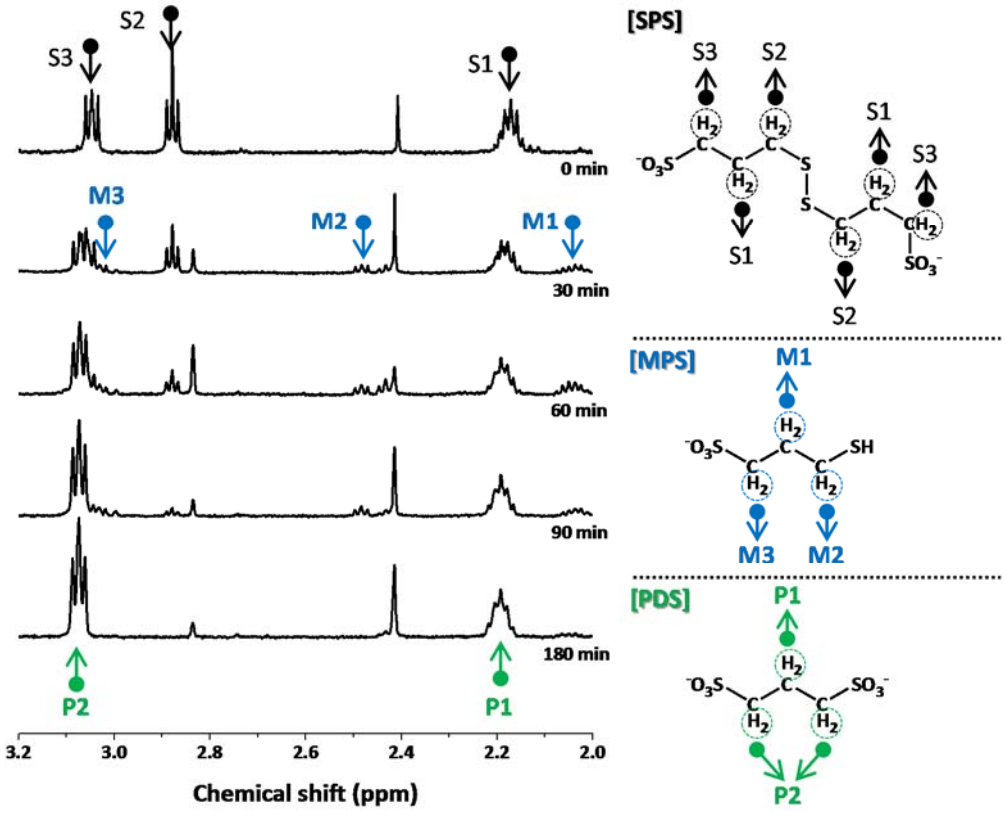


**Figure 3.3.** (a) $^{1}$H-NMR spectrums of plating solutions aged for 0, 30, 60, 90, 180 min. Black (S1~S3), blue (M1~M3), and green (P1, P2) arrows indicate the peaks of SPS, MPS, and PDS, respectively. $^{1}$H-NMR spectrums of (b) power and (c) standard samples were also displayed.

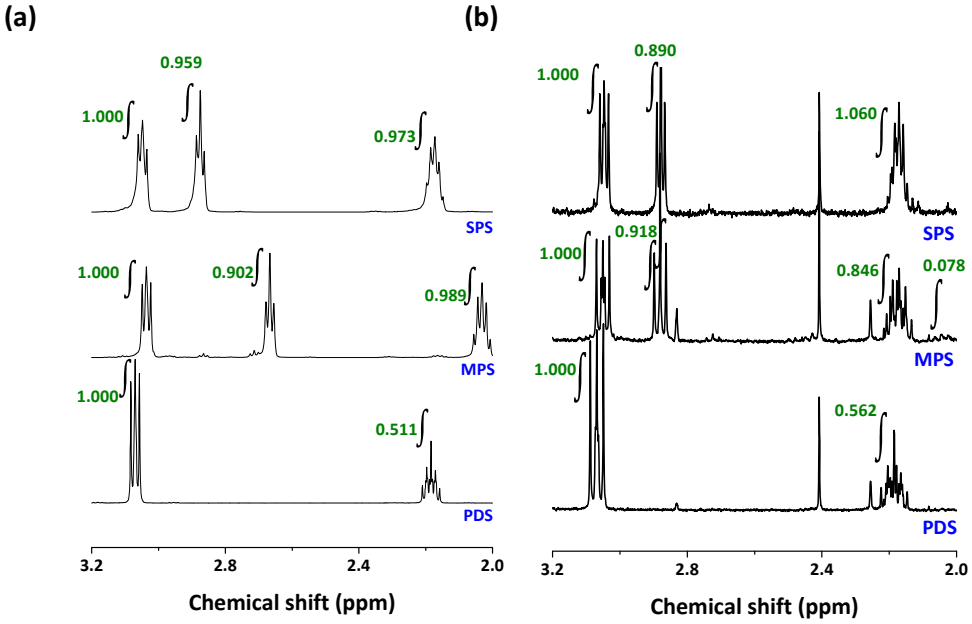


**Figure 3.4.** $^{1}$H-NMR spectrums of (a) power and (b) standard samples.

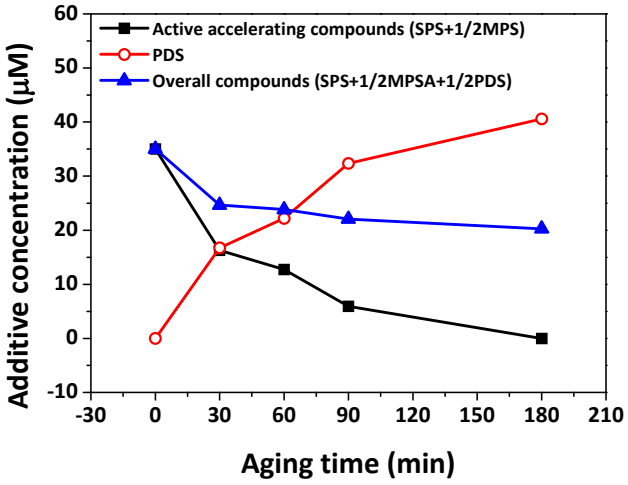


**Figure 3.5.** Concentrations of active accelerating compounds, PDS and overall compounds in the plating solution aged for 0, 30, 60, 90, and 180 min. The active accelerator concentrations were calculated from the sum of SPS and one-half of MPS concentrations.

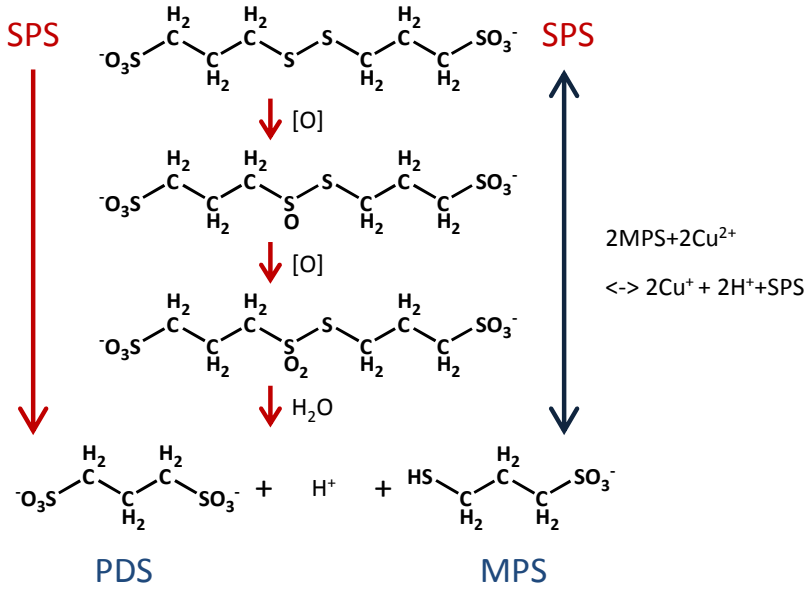


**Figure 3.6.** Decomposition pathway of SPS during electrodeposition.

## 3.2. Effect of SPS Concentration

Figures 3.7(a)–(f) show the filling profiles after electrodeposition with various SPS concentrations and the corresponding CVs. The bath containing more than 17.5 μM SPS showed excellent filling performance and clear hysteretic behaviors in the CVs. However, when the concentration of SPS was below 8.75 μM, voids appeared and the filling profiles changed from superconformal to conformal. Although a minimal SPS concentration enabling superfilling could be dependent on the feature dimensions as well as on the chemistries of the suppressor and leveler, it suggested that SPS concentration should be tightly controlled over the critical value in order to maintain the performance of the plating solution.

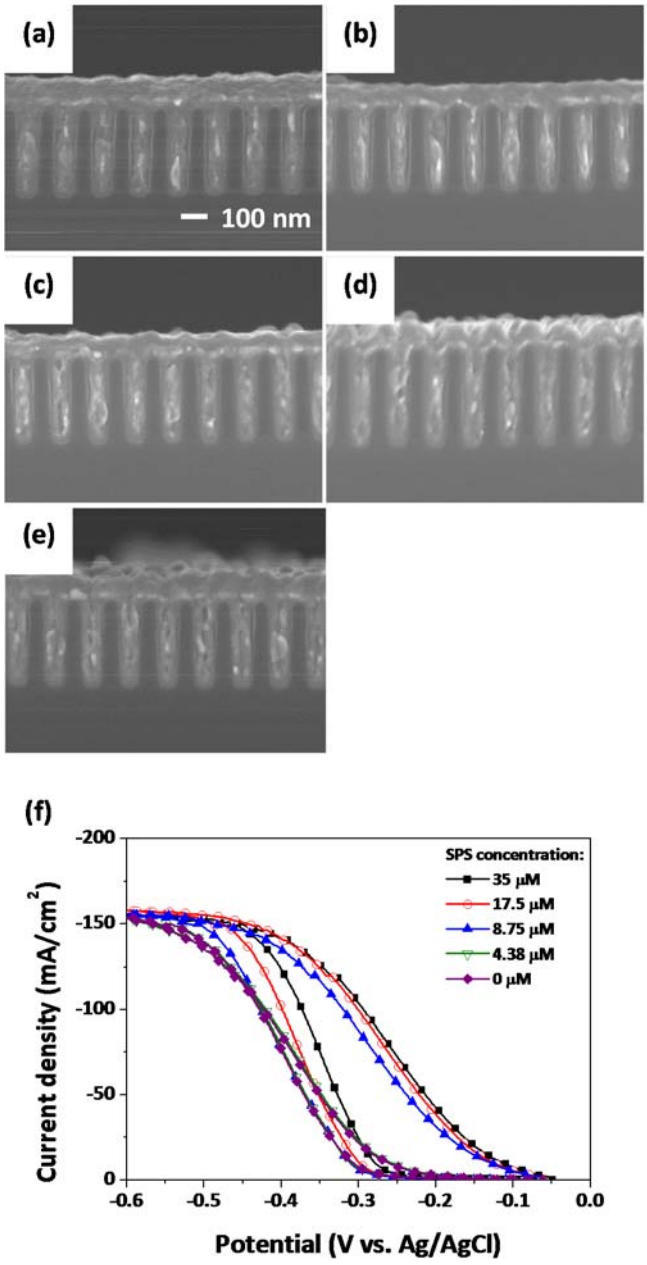


**Figure 3.7.** Filling performance of SPS as function of its concentration: (a) 35, (b) 17.5, (c) 8.75, (d) 4.38, and (e) 0 μM, respectively. PEG–PPG (360 μM) was also added. The CV voltammograms corresponding to (a)–(e) are shown in (f).

## 3.3. Effect of PDS

Figure 3.8 shows the redox reactions of SPS-related compounds during Cu electrodeposition. As described at Eqs. 3.1–3.3, SPS continuously decomposes through chemical/electrochemical processes, forming MPS and PDS as its breakdown products. Taking into account of stoichiometry ratio, one SPS molecular produces either two MPS molecular, two PDS molecular, or one MPS and one PDS molecular after conversion. Based on those factors, the following variables (Eqs. 3.4-3.6) might be related to the superfilling capability of the plating solution.

$$\text{Concentration of total accelerating compounds } (C_T) = C_S + \frac{1}{2}C_M \quad \text{(Eq. 3.4)}$$

$$\text{Conversion ratio of SPS to PDS } (X_P) = \frac{1/2C_P}{1/2C_P + C_S} \quad \text{(Eq. 3.5)}$$

$$\text{Conversion ratio of SPS to MPS } (X_M) = \frac{1/2C_M}{1/2C_M + C_S} = \frac{C_M}{2C_T} \quad \text{(Eq. 3.6)}$$

where $C_S$, $C_M$, and $C_P$ are the concentrations of SPS, MPS, and PDS, respectively. Physically, $C_T$ refers to the sum of intact and dissociated SPS (note that the dissociation of 1 molecule of SPS forms 2 molecules of MPS), while $X_S$ indicates the mole fraction of dissociated SPS. Namely, the decrease of $C_T$ implies the consumption of SPS by

incorporation and oxidative decomposition resulting in PDS formation, while the increase of $X_S$ means the consumption of SPS by dissociation to form MPS.

The conversion ratio from SPS to PDS could influence the overall bath performance. Figure 3.9(a) shows the CV results of the plating solution as a function of $X_P$, i.e., the artificially controlled ratio between the SPS and PDS concentrations. As presented in Figure 3.9(a), the acceleration effect in the forward scan decreased as $X_P$ increased, and the hysteresis disappeared at 100% conversion ($X_P = 1$). This tendency was consistent with the CVs of plating solutions aged by electrodeposition (Figure 3.2). The changes of electrochemical behavior were ascribed to the lack of acceleration effect of PDS. PDS had no significant influence on electrochemical behavior in the forward and reverse CV scans, regardless of its concentration [Figure 3.9(b)].

In order to verify the influence of PDS on the properties of Cu films, Cu films were deposited under various PDS concentrations. Figures 3.10(a)–(e) reveal that the surface morphology and resistivity were not significantly influenced by the PDS concentrations when SPS, PEG–PPG, and Cl- coexisted in the plating solutions. Figures 3.11(a)–(c) exhibit the crystalline orientation, the grain sizes calculated by Scherrer's equation, and the carbon content of the deposited Cu films as a function of PDS concentration. The changes in crystallinity and grain sizes with respect to PDS concentrations were also

negligible, whereas the carbon content of the Cu films slightly increased, perhaps due to the incorporation of PDS into the Cu film.

The influence of PDS on the electrochemical behavior and properties of the deposited Cu films were negligible, regardless of its concentration, possibly due to the absence of functional groups that allow PDS to be adsorbed onto a Cu surface. PDS does not contain mercapto or disulfide groups, which are known to tether the accelerator to the Cu surface.[84,99] Although PDS has two sulfonate groups that are essential for the acceleration effect, these groups alone could not effectively interrupt the suppressor-Cl- layer, a claim supported by the experimental results from Moffat *et al.*, who showed that PDS did not influence the voltammetry in the presence of PEG–Cl- because it could not form a chemical linkage to the Cu surface.[99]

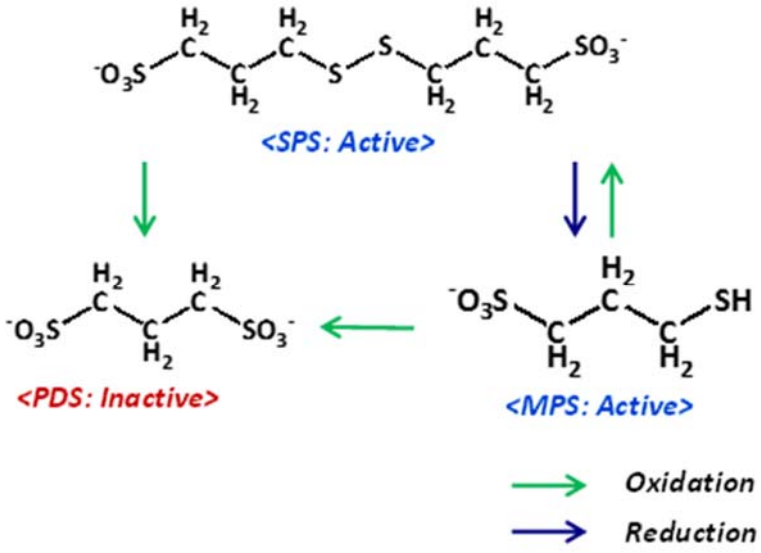


**Figure 3.8.** Redox reactions of SPS-related compounds during Cu electrodeposition.

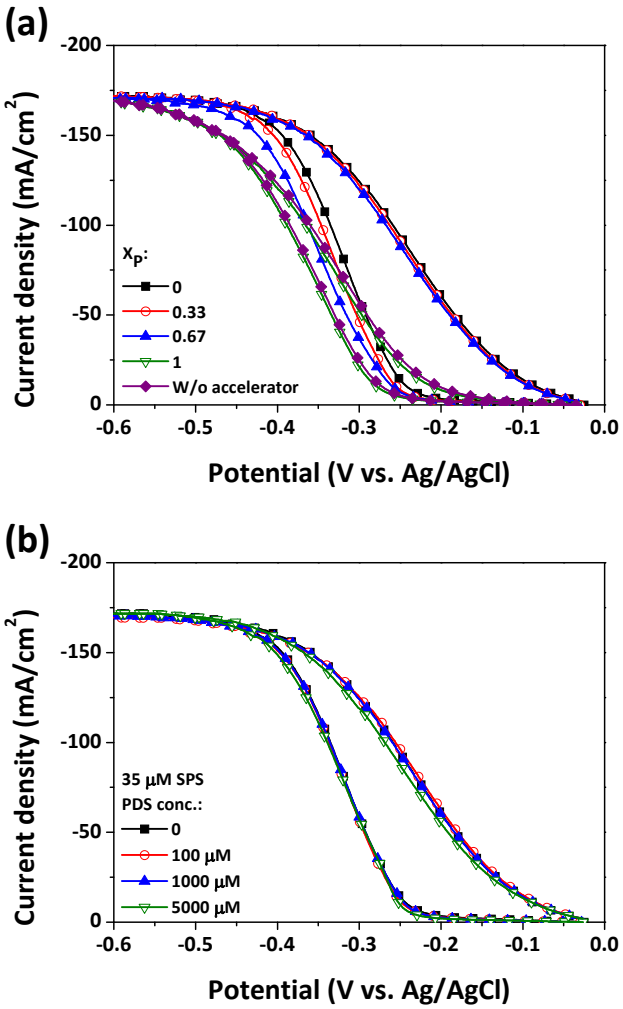


**Figure 3.9.** CV results of plating solution as function of the (a) conversion ratio of SPS and (b) PDS concentrations. PEG–PPG (360 μM) was also added.

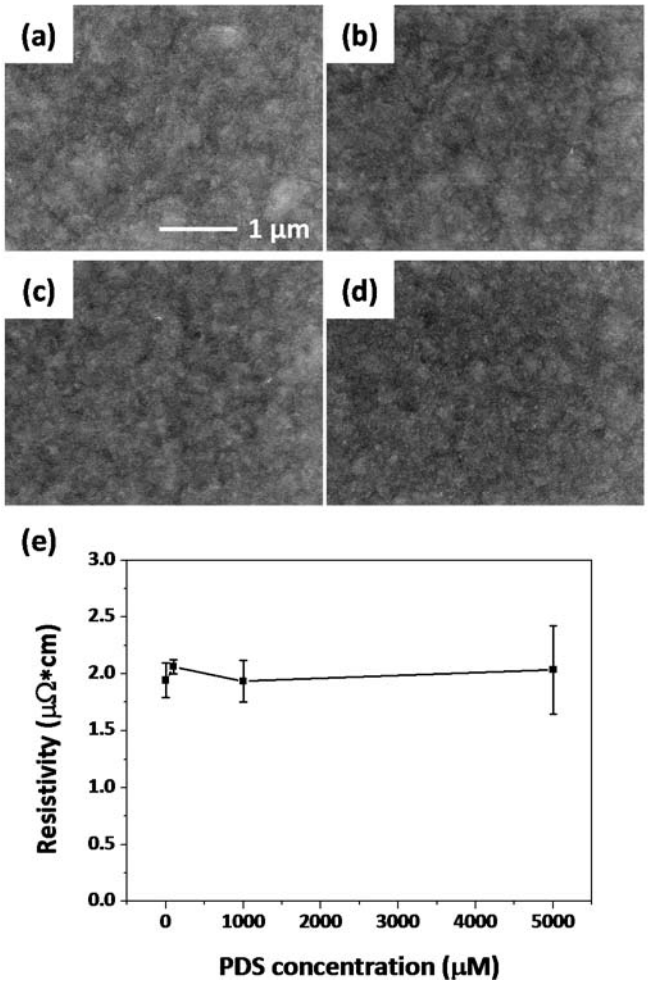


**Figure 3.10.** Surface morphology of Cu films deposited with (a) 0, (b) 100, (c) 1000, (d) 5000 μM PDS. PEG–PPG (360 μM) was also added. The resistivities obtained from (a)–(d) are shown in (e).

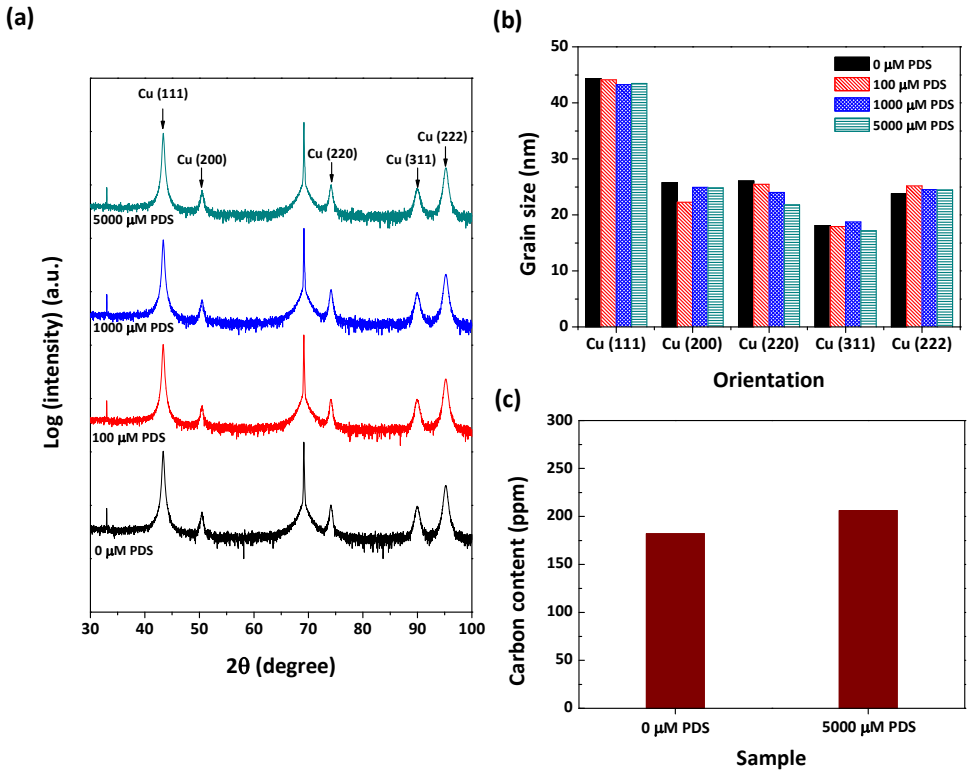


**Figure 3.11.** (a) XRD spectrum, (b) grain sizes, and (c) carbon contents of Cu films deposited with 0, 100, 1000, 5000 μM of PDS. PEG–PPG (360 μM) was also added. The grain sizes of the films were obtained from Scherrer's equation.

## 3.4. Effect of MPS

Figure 3.12 shows the CVS voltammogram as a function of artificially controlled $X_M$ at the same $C_T$ of 4.5 μM. It was observed that the stripping current density in a potential range of 0.05 V- 0.35 V increased as $X_M$ increased. This means that 2 equivalents of MPS was more effective than 1 equivalent of SPS in accelerating Cu reduction on the flat electrode, as reported by Tan *et al.* and Moffat *et al.* who observed the stronger acceleration effect of MPS than SPS using chronoamperometry experiments.[88,100]

Despite the superfilling-incapability of MPS, its electrochemical acceleration effect, as shown in Figure 3.12 and the literatures might lead to significant error in the results of conventional MLAT-CVS analysis since the electrochemical responses of SPS and MPS are not distinguishable in the conventional MLAT-CVS. (Note that conventional MLAT-CVS provides only a stripping charge value, regardless of where the increased stripping charges originate—from either MPS or SPS). Table 3.1 shows the measured C values by conventional MLAT-CVS analysis of various plating solutions having different $C_S$ and $C_M$. This confirms that the accuracy of conventional MLAT-CVS is guaranteed only when $X_M = 0$ ($C_M = 0$). Otherwise, the C value is always higher than the actual $C_S$ because of the acceleration effect by MPS. Furthermore, the measured C values exhibit

significant deviation from $C_T$ due to the strong accelerating ability of MPS compared to that of SPS.

Figure 3.13 presents the filling performances of plating solutions #1–#6 (refer to Table 1 for details). As shown in Figures 3.13 (a)–(f), the filling capability is a strong function of $X_M$ (i.e. $C_S$ and $C_M$); the increase of $X_M$ leads to degradation of the filling capability. Similar results were reported by Kim *et al.* showing that MPS itself is unable to induce bottom-up filling, whereas its dimerized form, SPS, enabled superfilling.[42] One notable point is the adverse effect of MPS on the filling capability. Figures 3.13(a) and (d) show that in the absence of MPS in the plating solution, an SPS concentration within the range of 25–50 μM is sufficient to induce superfilling. However, as shown in Figures 3.13(b) and (c), the use of solutions #2 and #3, containing 20–40 μM MPS, result in a conformal filling profile, which implies that the presence of MPS causes deterioration of the filling capability.

Consequently, it is clearly revealed that the filling capability relies on not only $C_S$ but also $C_M$. Therefore, it is necessary to develop the techniques that enable the determination of both $C_S$ and $C_M$ for the accurate monitoring of solution performance without actual filling test.

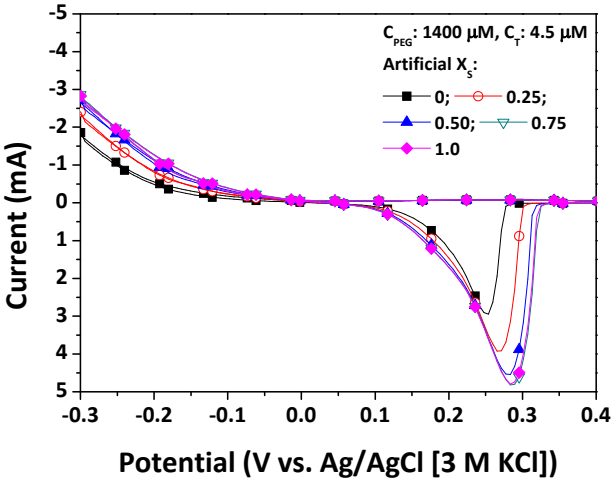


**Figure 3.12.** CVS results showing the influence of XS on the accelerating effect.

**Table 3.1.** Measured Concentrations of Accelerator with Conventional MLAT-CVS Analysis.

| Solution | Actual values | | | Conventional CVS | |
|---|---|---|---|---|---|
| | $C_S$ (μM) | $C_M$ (μM) | $C_T$ (μM) | $X_S$ | C* (μM) |
| #1 | 50 | 0 | 50 | 0 | 50.32 (±1.97) |
| #2 | 40 | 20 | 50 | 0.2 | 55.07 (±2.31) |
| #3 | 30 | 40 | 50 | 0.4 | 86.96 (±5.64) |
| #4 | 25 | 0 | 25 | 0 | 24.46 (±1.29) |
| #5 | 20 | 10 | 25 | 0.2 | 24.32 (±1.64) |
| #6 | 15 | 20 | 25 | 0.4 | 36.16 (±2.04) |

*Note that C is conventionally treated as $C_S$.

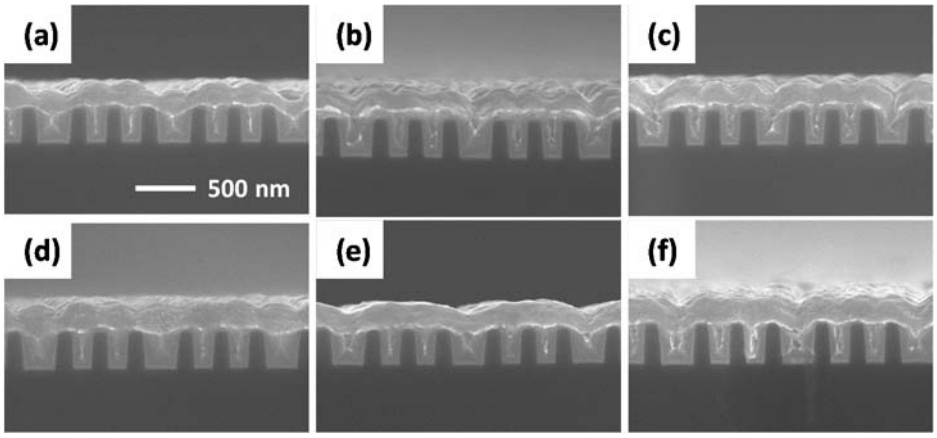


**Figure 3.13.** Filling performances of plating solutions (a) #1, (b) #2, (c) #3, (d) #4, (e) #5, and (f) #6 (see Table 1 for details)

## 3.5. Summary

During continuous usage of the plating solution, SPS converted to MPS and PDS. Although MPS recombined to form SPS through an oxidation reaction with cupric ions, the conversion to PDS was irreversible, which led to the accumulation of PDS in the plating solution. This conversion of SPS into PDS resulted in the disappearance of the electrochemical acceleration effect and a degradation of bath performance. However, the influence of PDS on electrochemical behavior and film properties was negligible due to the absence of critical functional groups capable of making the linkage on Cu surface. These results suggested that the failure by SPS decomposition mainly resulted not from the accumulation of PDS but rather from the decrease in the SPS concentration or the formation of MPS.

Though MPS enhances the Cu deposition rate on flat electrodes, it is not a superfilling-capable accelerator for the damascene structure, unlike SPS. Enhancement of the Cu deposition rate by MPS interferes with the electrochemical signal of SPS, leading to a significant error when using the modified MLAT-CVS analysis method.

# Chapter IV. Advanced CVS Monitoring Method

## 4.1. Two-step CVS Analysis

At chapter 3, it is revealed that $C_S$ and $C_M$ are significant factors affecting the performance of plating bath, while the effect of $C_P$ is negligible. However, it is difficult to determine $C_M$ and $C_S$ individually with conventional MLAT-CVS because the electrochemical responses of MPS and SPS are overlapped.

Therefore, in this chapter, a new electrochemical method is suggested to determine both $C_S$ and $C_M$ in Cu plating bath. This method is based on the algorithm described at Figure 4.1, in which $C_T$ and $X_S$ are determined instead of $C_S$ and $C_M$. The combination of $C_T$ and $X_S$ yields $C_S$ and $C_M$, as shown Eqs. 4.1-2.

$$C_M = 2C_T X_S \text{ (Eq. 4.1)}$$

$$C_S = C_T(1 - X_S) \text{ (Eq. 4.2)}$$

$C_T$ can be obtained by sequential steps of artificial conversion of MPS to SPS (i.e. establishing the condition of $X_S = 0$) and then measuring the C value using MLAT-CVS (note that $C = C_S = C_T$ when $X_S = 0$, see Table 3.1). In detail, the first step aims to evaluate $C_T$ by the intentional control of another variable ($X_S$) with the chemical

treatment of plating solutions. Table 4.1 describes our detail strategy for oxidation of MPS into SPS. The oxidation of MPS into SPS can be accomplished by the additions of oxidizing agents or by the control of pH to higher value that prompts the reaction 1.3.

In order to observe the conversion of MPS after the addition of oxidizing agent, $H_2O_2$, $^1$H-NMR analysis is carried out and the results are presented at Figure 4.2. When $H_2O_2$ was added, the MPS are oxidized into not only SPS but also PDS, indicating that the use of this method results in the oxidation of MPS into not SPS but PDS.

Figure 4.3 presents the $^1$H-NMR spectra of MPS in the Cu plating solutions with pH = 0.3, 2, and 4 after 20 min in the open circuit condition. For the case of pH = 0.3, the chemical structure of MPS remains, whereas for weak acidic conditions of pH = 2 and 4, MPS completely converts to SPS within 20 min. This is because the forward reaction of Eq. 1.3 is promoted in relatively high pH conditions by Le Chatelier's principle. Fast thiol oxidation to disulfide at high pH has been reported elsewhere, including protein engineering.[101] Similar NMR study by Garcia-Cardona *et al.* demonstrated the formation of SPS and Cu-thiolate complex from the reaction between MPS and $Cu^{2+}$ in moderate pH condition (0.25 M $D_2SO_4$).[102] This work also supports that SPS is originated from reaction 1.3, though the different pH with our work might cause the different conversion rate.

Figure 4.4 presents the CVS results with various $X_S$ values for the case of pH = 2. The current densities and corresponding stripping charges are independent of $X_S$, unlike in strong acidic conditions of pH = 0.3 (Figure 3.12). As shown in the $^1$H-NMR results (Figure 4.3), this seems to result from complete oxidation of MPS into SPS.

The pH adjustment of the target plating solutions led to the condition of $X_S = 0$ ($C_M = 0$), resulting in identical CVS plots, regardless of the initial $X_S$ values. As shown in Table 3.1, C values from conventional MLAT-CVS match well with $C_T$ in the case of $X_S = 0$. This means that $C_T$ can now be evaluated with MLAT-CVS analysis after pH adjustment of the plating solution. Figure 4.5 shows the measured concentrations by MLAT-CVS for 50 μM $C_T$ with various $X_S$ values before and after pH adjustment. It was observed that in the case without pH adjustment, the measured $C_T$ value increases as $X_S$ increases due to the stronger accelerating ability of MPS than SPS. However, when the pH of the target solution is adjusted, the measured $C_T$ values are in good agreement with the actual $C_T$ values of 50 μM, regardless of the initial $X_S$.

The above results show that $C_T$ can be accurately measured by MLAT-CVS analysis after pH adjustment. However, $C_T$ itself cannot fully indicate the filling capability of the plating solution because the filling capability strongly depends on not only $C_T$ but also $X_S$ (Figure 3.13). Therefore, additional analysis to measure $X_S$ must be developed, which

can be performed based on the result that the acceleration effect of MPS is relatively stronger than that of SPS (Figure 3.12). This means that $X_S$ influences the current density and stripping charges in the CVS analysis, as presented in Figure 4.6. Figure 4.6(a) shows that the stripping charge increases linearly with the increase in $C_T$, and the slopes of the plot, $(\Delta Q/Q_i)/\Delta C_T$, are affected by $X_S$. Figure 4.6(b) presents the relation between $(\Delta Q/Q_i)/\Delta C_T$ and $X_S$, which reveals that $(\Delta Q/Q_i)/\Delta C_T$ linearly increases as $X_S$ increases in the range of $X_S < 0.5$. This relationship will be further used in the independent determination of $C_M$ and $C_S$.

Figure 4.7 presents the procedures of the two-step CVS for determination of $C_T$ and $X_S$. In the first step, the pH adjustment of the target plating solution was carried out in order to oxidize MPS into SPS, using an alkaline solution consisting of 2.4 M KOH and 1.0 mM NaCl. Then, MLAT-CVS analysis was performed to determine $C_T$. In the second step, the target solution was diluted with 1.0 mM NaCl in a 1:1 ratio, which was added to IS1 3–5 times. The stripping charges were measured after each addition, from which the graph for $Q/Q_i$ vs. addition volume of the target solution was obtained. The addition volume of the target plating solution can be converted to $C_T$ of IS1 using the following equation.

$$C_{TI} = \frac{C_{Tt} \cdot V_t}{V_{IS1} + V_t} \quad \text{(Eq. 4.3)}$$

where $C_{TI}$ is the $C_T$ value of IS1 after addition of the target plating solution, $C_{Tt}$ is the $C_T$ of the target plating solution, $V_t$ is the addition volume of the target plating solution, and $V_{IS1}$ is the initial volume of IS1. Therefore, the plot of $Q/Q_i$ vs. $C_{TI}$ could be obtained, in which $(\Delta Q/Q_i)/\Delta C_{TI}$ is converted to $X_S$ using the calibration curves presented in Figure 4.6(b). The values of $C_{Tt}$ and $X_S$ were then used to determine $C_S$ and $C_M$, as described in Eqs. 4.1 and 4.2.

The accuracy of the two-step MLAT-CVS analysis was verified using the same test samples of solutions #1–#6 (Table 3.1) and the results are presented in Table 4.2. Table 4.2 shows now the complete sets of $C_S$, $C_M$, $C_T$, and $X_S$ values for solutions #1–#6. The C values from conventional MLAT-CVS and filling performances of solutions #1–#6 are also presented for comparison. As shown in Table 3.1, the conventional MLAT-CVS provides only the concentration (C), which is not in good agreement with the actual $C_S$ except when $X_S = 0$ ($C_M = 0$). In addition, the conventional MLAT-CVS cannot provide $C_M$, which limits the accurate assessment of solution performance. However, for the case of the modified two-step MLAT-CVS, both $C_M$ and $C_S$ were accurately measured within 10% error. By providing $X_S$ values, the superfilling-capability of the test solutions is now also predictable without actual filling tests; an extremely low $X_S$ (close to zero) corresponds to good superfilling performance.

By combining two-step CVS and $^{1}$H-NMR analyses, the concentrations of SPS, MPS, and PDS in operating Cu bath were monitored. Figure 4.8 reveals that the use of Ir/$IrO_x$ insoluble anode results in rapid SPS decomposition, because the high anodic overpotential of Ir/IrOx electrode increases the rate of reaction Eq. 3.2. Otherwise, the use of soluble anode increases the concentration of $Cu^{+}$, thereby prompting the dissociation of SPS into MPS. Above results demonstrate that the use of two-step CVS facilitates the in-situ monitoring of SPS and MPS in operating Cu plating bath. These results indicate the powerful ability of the developed two-step MLAT-CVS as a monitoring tool for Cu superfilling baths.

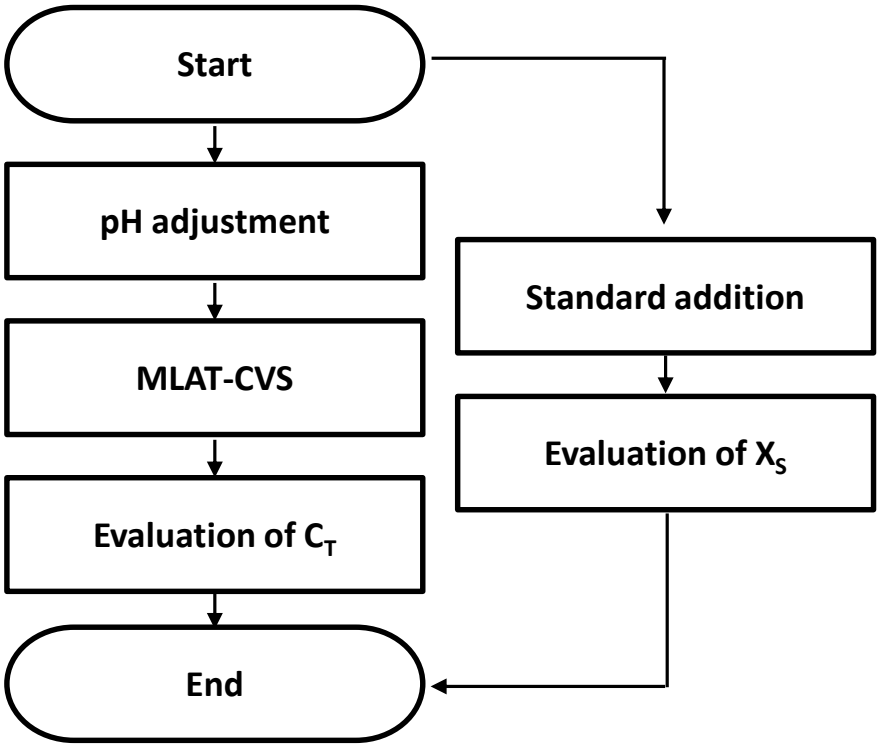


**Figure 4.1.** Algorithm of two-step CVS analysis.

**Table 4.1.** Strategy to Oxidize MPS into SPS.

| Treatments | Strategy | Expected reaction |
|---|---|---|
| #1 | Forced oxidation of MPS into SPS using oxidizing agent | $2MPS + H_2O_2 \rightarrow SPS + 2H_2O$ |
| #2 | Acceleration of MPS oxidation by $Cu^{2+}$ with pH adjustment | $2Cu^{2+} + 2MPS \rightarrow 2Cu^{+} + SPS + 2H^{+}$ |

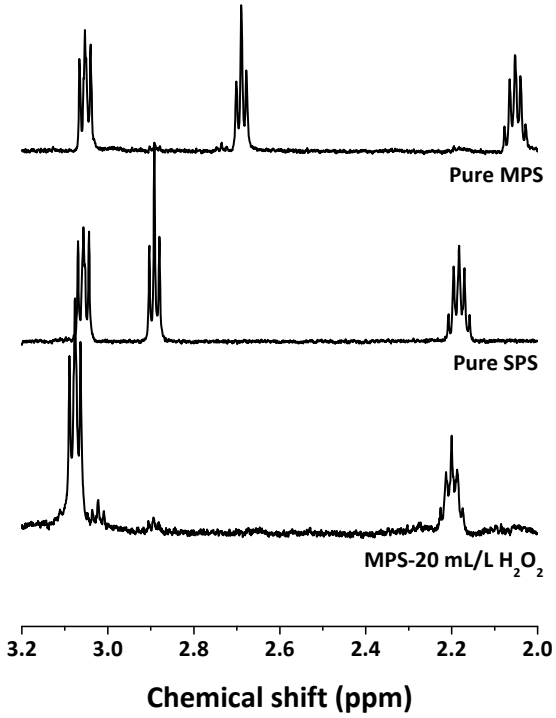


**Figure 4.2.** $^{1}$H-NMR results of MPS in Cu plating solutions after the treatments 1. (see Table 3.1)

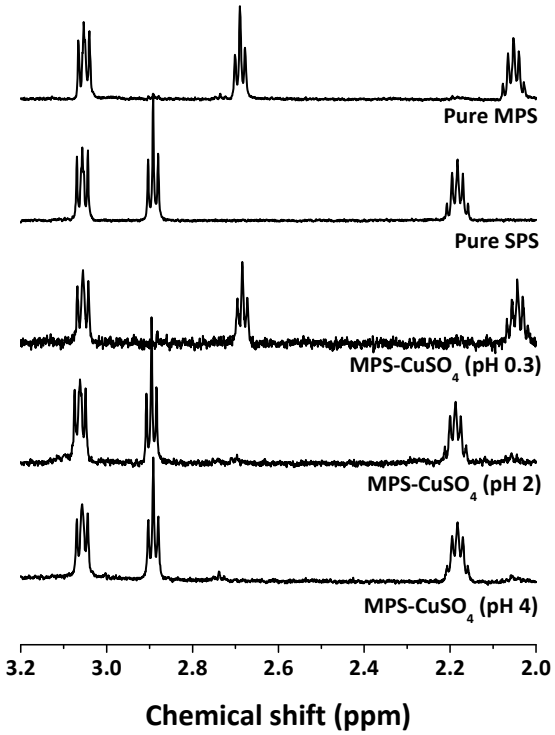


**Figure 4.3.** $^{1}$H-NMR results of MPS in $D_2O$ solutions containing 1 mM $CuSO_4$ and different amounts of $H_2SO_4$ as a pH adjuster. For the comparison, $^{1}$H-NMR results of SPS and MPS in pure $D_2O$ were also presented.

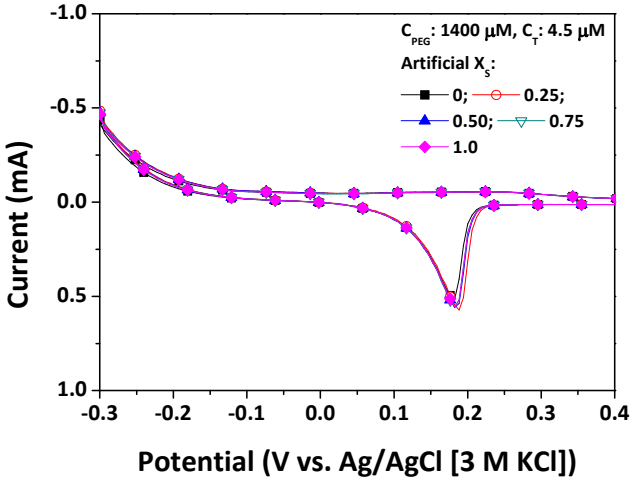


**Figure 4.4.** CVS results with various $X_S$ values after pH adjustment.

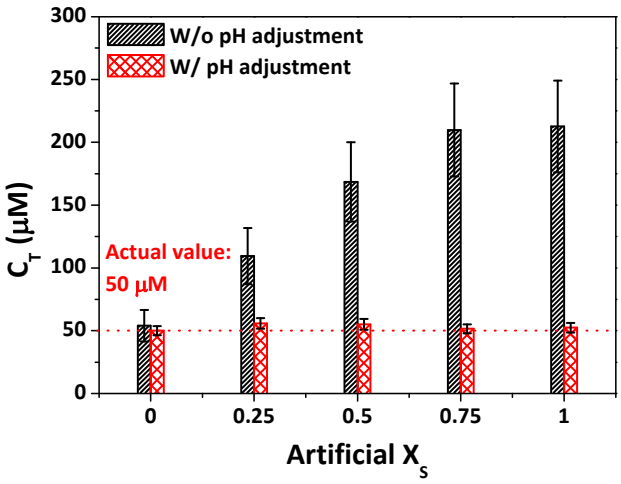


**Figure 4.5.** MLAT-CVS results of accelerator concentrations in Cu plating solutions with and without pH adjustment.

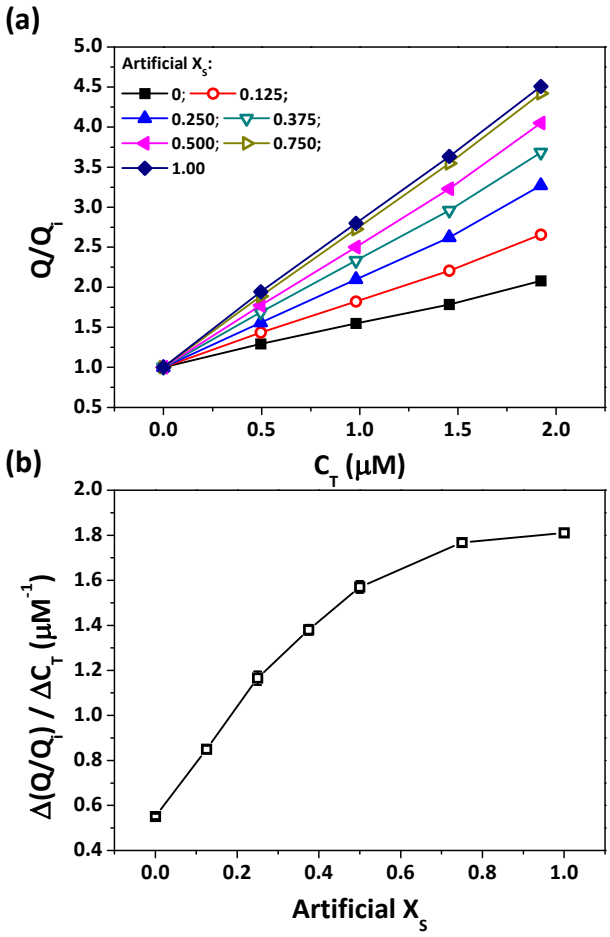


**Figure 4.6.** (a) $Q/Q_i$ as a function of $C_T$ with various $X_S$ values. The slope of the $Q/Q_i$ vs. $C_T$ plot is presented in (b).

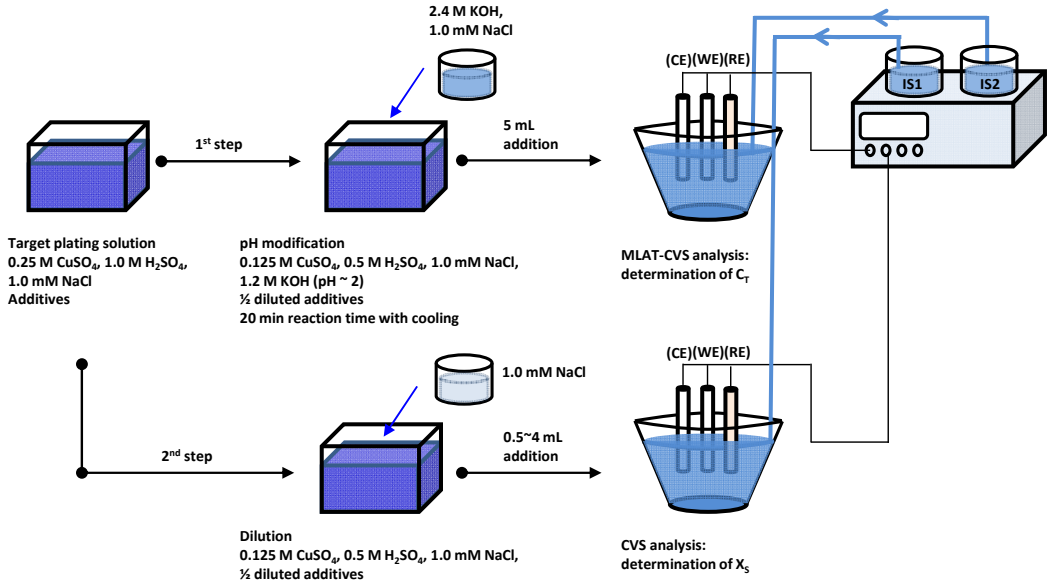


**Figure 4.7.** Modified CVS analysis procedure.

**Table 4.2.** Measured $C_T$, $X_S$, $C_S$, and $C_M$ with Modified CVS Analysis.

| Soln. | Actual values | | | | Modified CVS | | | |
|---|---|---|---|---|---|---|---|---|
| | $C_T$ (μM) | $C_S$ (μM) | $C_M$ (μM) | $X_S$ | $C_T$ (μM) | $C_S$ (μM) | $C_M$ (μM) | $X_S$ |
| #1 | 50 | 50 | 0 | 0 | 50.07 (±2.06) | 49.77 (±2.08) | 0.60 (±0.02) | 0.006 |
| #2 | 50 | 40 | 20 | 0.2 | 51.76 (±2.76) | 42.24 (±2.57) | 19.05 (±1.01) | 0.184 |
| #3 | 50 | 30 | 40 | 0.4 | 50.09 (±2.48) | 32.05 (±2.11) | 36.06 (±1.78) | 0.360 |
| #4 | 25 | 25 | 0 | 0 | 24.28 (±1.49) | 23.43 (±1.46) | 1.70 (±0.10) | 0.035 |
| #5 | 25 | 20 | 10 | 0.2 | 25.30 (±2.10) | 20.50 (±1.91) | 9.61 (±0.80) | 0.190 |
| #6 | 25 | 15 | 20 | 0.4 | 26.38 (±2.65) | 16.77 (±2.29) | 19.20 (±1.93) | 0.364 |

*Note that C is conventionally treated as $C_S$.

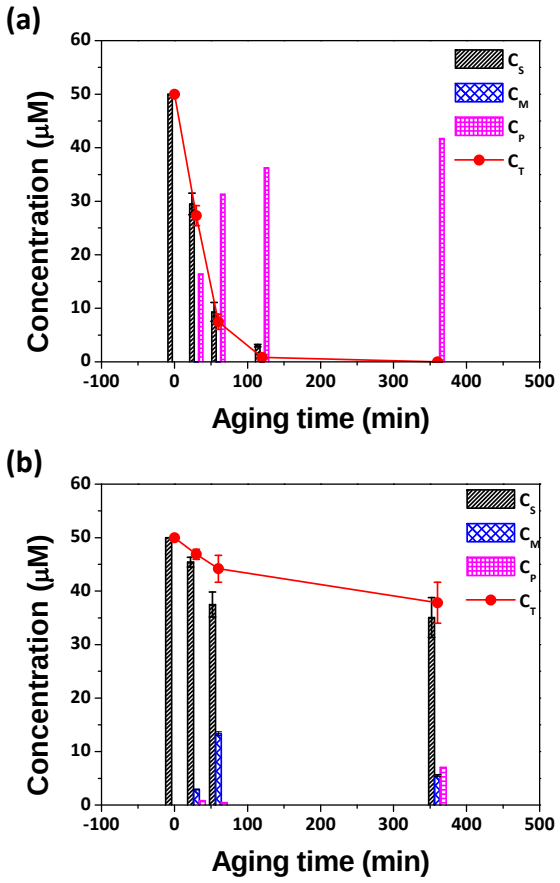


**Figure 4.8.** Concentration changes of SPS, MPS, and PDS during aging experiments.

The anode materials are (a) Ir/$IrO_x$ plate and (b) Cu plate, respectively.

## 4.2. Summary

A modified two-step MLAT-CVS method was suggested as a powerful tool for evaluation of $C_S$ (concentration of SPS) and $C_M$ (concentration of MPS) in an acidic Cu plating bath. This method is designed to determine two important parameters (the total accelerator concentration $C_T$ and the conversion ratio $X_S$) governing the filling capability of the plating solution. In order to obtain $C_T$, the condition of $X_S = 0$ was established by intentional pH control of the target plating solution, whereby MLAT-CVS analysis could reveal $C_T$ without the interference of MPS. $C_T$ was then converted to individual concentrations, $C_S$ and $C_M$, using $X_S$ evaluated from the difference of the relative accelerating abilities between SPS and MPS. This modified method quickly provided $C_S$ and $C_M$ of the sample baths with less than 10% error, enabling the accurate prediction of the filling performance of the solution without actual filling tests.

# Chapter V. Decomposition of PEG-PPG

## 5.1. Decomposition of PEG-PPG

PEG-PPG is one of the suppressor-type additive comprising the alternative chains of ethylene glycol and propylene glycol. Although the decomposition of PEG-PPG during Cu electrodeposition has not reported yet, many previous researchers have investigated about breakdown of PEG during electrodeposition. L.D' Urzo et al reported that PEG was fragmented during electrodeposition by the nucleophilic substitution reaction occurring at cathode.[74] Meanwhile, Y.S Won *et al.* suggested the radical decomposition mechanism to explain the fragmentation of PEG.[75] M. J. West *et al.* observed that the low-mass PEG was accumulated at the well-aged bath where the additives concentrations were maintained by daily bleed-and-feed method.[103,104] These accumulated by-products could be involved in the Cu deposition process. However, the influences of by-product accumulation in the plating solution were not fully understood.

This chapter describes the decomposition of PEG-PPG in the electrodeposition process and its influence on the performance of the plating solution. The by-products from PEG-PPG decomposition were examined using spectroscopic methods. In addition, the

influence of by-products was analyzed by maintaining the concentration of PEG-PPG using the periodic complement based on CVS measurements.

The by-products of the decomposition of PEG-PPG during electrodeposition were analyzed using $^{1}$H- and $^{13}$C- NMR and MALDI-TOF spectroscopy. Figures 5.1 and 5.2 depict the $^{1}$H- and $^{13}$C-NMR spectra of fresh and aged electrolytes. Before aging, $^{1}$H-NMR spectrum showed the peaks of original bath components; PEG-PPG (4.00-3.00 ppm, 1.56 ppm, 1.36 ppm, 1.18 ppm, and 0.92 ppm), $H_2O$ (4.81 ppm), and SPS (3.06 ppm, 2.87 ppm, 2.17 ppm). The peaks originated from PEG-PPG were also found in $^{13}$C -NMR spectrum at 65-80 ppm, 33.5 ppm, 21.5 ppm, 18.7 ppm and 16.0 ppm, while the peaks of SPS were indistinct due to the low resolution of $^{13}$C-NMR. The corresponding chemical structures of each peak in $^{1}$H- and $^{13}$C-NMR spectra are summarized in Table 5.1.

In $^{1}$H-NMR, the aged plating solution showed several peaks at the chemical shifts of 9.50 ppm, 8.47 ppm, 3.66 ppm, 2.83 ppm, and 2.05 ppm. The relative intensities of these peaks gradually increased as the duration of aging increased, which implied the formation of by-products from the decomposition of PEG-PPG. The intensities of peaks at 8.47 ppm and 3.66 ppm were relatively stronger compared to the other peaks, indicating that these two peaks were related to the major by-products.

Figures 5.1(b)–(f) shows the magnified images of the peaks and their corresponding chemical structures. From the chemical shift as well as coupling, the singlet shown in Figure 5.1(b) is assumed to be the peak resulting from the hydrogen atom of the formic ester. This was also supported by the $^{13}$C-NMR spectrum that showed strong peaks at 174 ppm and 63 ppm after 9 hr of aging (Figure 5.2). Previous reports on the thermal degradation of PEG, PPG or PEG-PPG have indicated the formation of formic esters as a result of oxidation.[105-109] Both, S. Han *et al.*, and G. Gallet *et al.*, reported that α-hydroperoxides were formed on the carbon chains of either PEG or PEG-PPG upon the reaction of either PEG or PEG-PPG with oxygen.[105,107] Since α-hydroperoxide was thermally unstable, it decomposed through either the radical or intramolecular decomposition, yielding the formic ester as one of its final products.[105,108] Both of these mechanisms could also accompany the formation of aldehyde, ketone and hydroxyl groups as shown in Figures 5.1(c), (d), and (e), respectively.[105,108,109] Also, the quintet shown in Figure 5.1(f) is due to the hydrogen in the propyl group. The peaks from aldehyde, ketone, and propyl groups were unclear in $^{13}$C-NMR because of its lower sensitivity and small quantity of sample (Figure 5.2). The formation of aldehyde, hydroxyl, and propyl groups during electrodeposition has already been predicted by density functional theory (DFT) in previously published work. Y. S. Won *et al.* suggested

that the aldehyde and hydroxyl terminals could be formed during electrodeposition via an attack by OH radicals, by comparing the formation energy of the PEG radical with that of each terminal group using DFT.[75] The formation of hydroxyl group was also reported by L. D'Urzo *et al.*, who proposed that the PEG could be fragmented during electrodeposition through a nucleophilic substitution reaction.[74]

Figure 5.3 shows the changes in the mass distribution of PEG-PPG as a function of duration of aging. Initially, the mass of PEG-PPG was symmetrically distributed with a mean of 900 Da. However, this gradually changed with the fragmentation of PEG-PPG through decomposition during the electrodeposition. Consequently, the average MW decreased from 900 Da to 500 Da after 9 hr of electrodeposition.

Based on the chemical structures of breakdown products, the decomposition mechanism of PEG-PPG was proposed as described at Figure 5.4. The decomposition of PEG-PPG might be initiated by OH· radicals that are produced from the reactive $Cl_2$ gases or $Cu^+$ ions. Then, the radicals cause the internal electron transfer in PEG-PPG radicals, followed by the scissoring of -C-O- bonds and the formation of various terminal groups.

**Table 5.1.** Chemical Structures and Their Chemical Shifts of PEG-PPG, SPS, and Water in $^{1}$H- and $^{13}$C-NMR Spectra.

| Chemical structures | Chemical shift ($^{1}$H-NMR) | Chemical shift ($^{13}$C-NMR) | Chemical structures | Chemical shift ($^{1}$H-NMR) |
|---|---|---|---|---|
| **PEG-PPG** | | | **SPS** | |
| 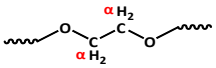 | α: 3-4 ppm | α: 65-80 ppm | 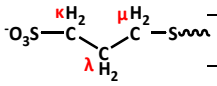 | κ: 3.06 ppm<br>λ: 2.17 ppm<br>μ: 2.87 ppm |
| 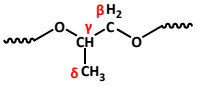 | β: 3-4 ppm<br>γ: 3-4 ppm<br>δ: 1.18 ppm | β: 65-80 ppm<br>γ: 65-80 ppm<br>δ: 18.7 ppm | **$H_2O$** | |
| | | |  | ν: 4.81 ppm |
| 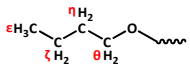 | ε: 0.92 ppm<br>ζ: 1.36 ppm<br>η: 1.56 ppm<br>θ: 3-4 ppm | ε: 16.0 ppm<br>ζ: 21.5 ppm<br>η: 33.5 ppm<br>θ: 65-80 ppm | | |

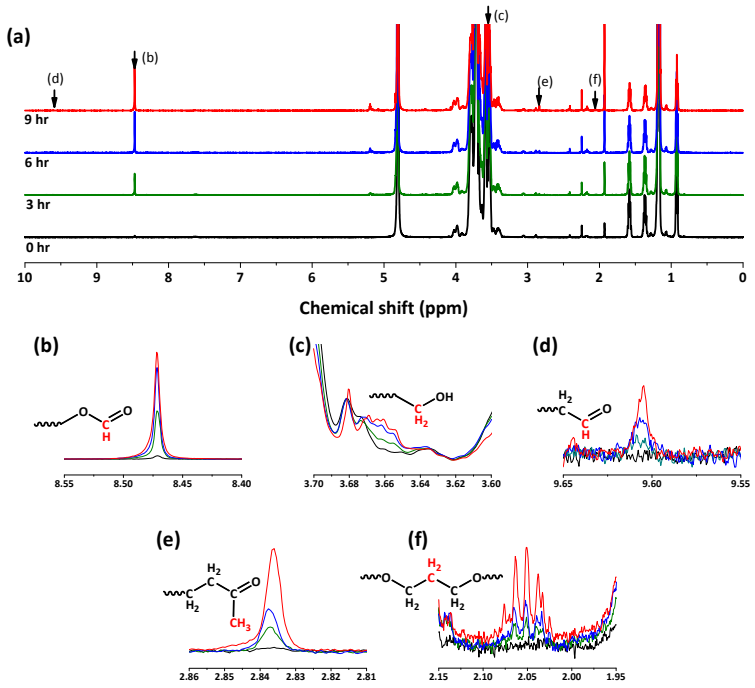


**Figure 5.1**. (a) Normalized $^{1}$H-NMR spectra of PEG-PPG after 0 hr, 3 hr, 6 hr, and 9 hr of aging. The magnified images of each of the peaks show the formation of (b) formic ester, (c) hydroxyl, (d) aldehyde, (e) ketone, and (f) propyl groups.

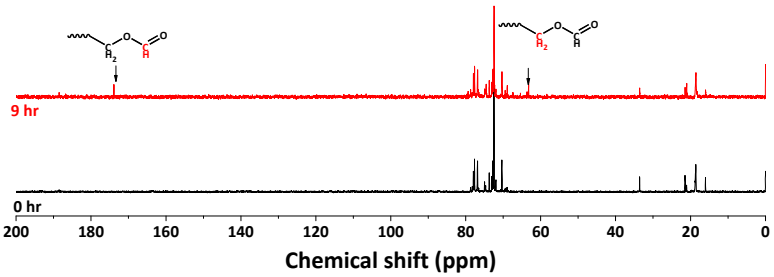


**Figure 5.2.** $^{13}$C-NMR spectra of PEG-PPG, before and after aging.

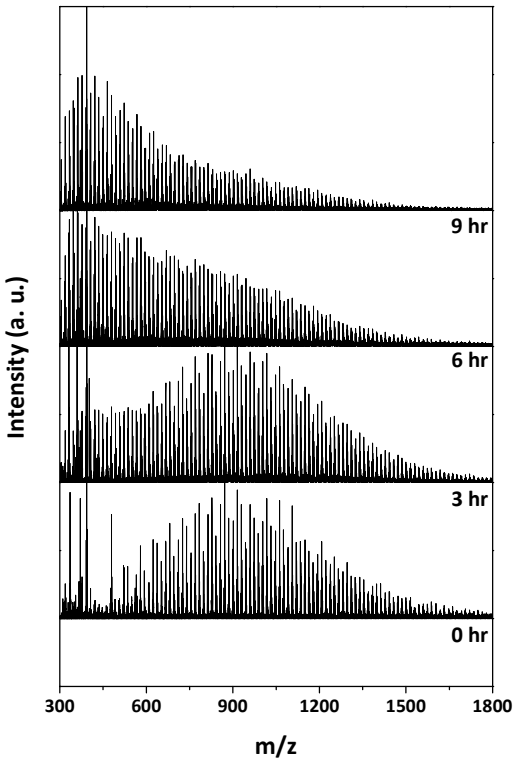


**Figure 5.3.** MALDI-TOF spectra of PEG-PPG after 0 hr, 3 hr, 6 hr, and 9 hr of aging.

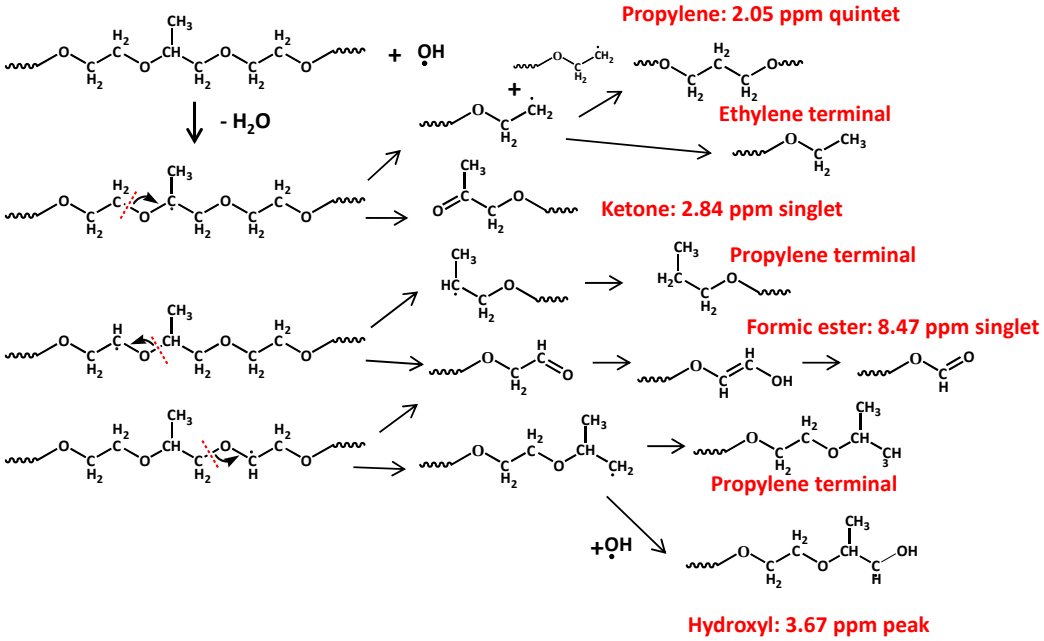


**Figure 5.4.** Decomposition mechanisms of PEG-PPG during Cu electrodeposition.

## 5.2. Effect of Breakdown Products

From Figures 5.1–5.3, it can be seen that the fragmented PEG-PPG with substituted functional groups was gradually produced in the plating solution during the electrodeposition. The accumulation of fragmented PEG-PPG possibly influenced the determination of concentration in CVS and properties of deposited Cu films, because the fragmented PEG-PPG got adsorbed on the Cu surface as well as affected the electrochemical measurements. In order to figure out the influence of fragmented PEG-PPG on the performance of the electrolyte, electrolytes with various aging times but comparable concentrations were prepared by aging and successive supplementation of fresh PEG-PPG using CVS. Figure 5.5 exhibits the change in the concentration of PEG-PPG during aging. As depicted by the solid line in Figure 5.5, the concentration of PEG-PPG decreased after several hours of aging, which was attributed to the incorporation of PEG-PPG into Cu films as well as reduction in the average MW due to decomposition.[110,111] The dotted lines in Figure 5.5 show that the concentration of PEG-PPG rebounded after an adequate supply of the supplement of fresh PEG-PPG. CVS measurements performed after dosing indicated that the PEG-PPG concentrations were in the range of 1362 μM to 1455 μM, which were comparable to the initial values.

The mass distribution of PEG-PPG in plating solutions after the addition of PEG-PPG supplement was examined by MALDI-TOF and GPC as described in Figures 5.6 and 5.7. As shown in Figure 5.6, the mass distribution of PEG-PPG was initially symmetric, but changed to a bimodal shape with two distribution centers at 400 Da and 900 Da. These came from the fragmented and fresh PEG-PPG in the series of aging and PEG-PPG supplement steps. The average MW of PEG-PPG seemed to have decreased due to an accumulation of fragmented PEG-PPG in the plating solution. As shown in Figure 5.7, an increase in the retention time in the GPC spectrum was associated with either a reduction in the physical sizes of PEG-PPG or an increase in the affinity between the solid phase and PEG-PPG. The changes in the hydrophilicity of PEG-PPG due to decomposition were negligible; rather, those changes were brought about by a reduction in the average MW of PEG-PPG in the plating solution. Based on Figures 5.6-5.7, it can be concluded that the mass distribution of PEG-PPG was inevitably changed due to an increase in the amount of fragmented PEG-PPG.

In order to clarify the influence of by-products, the changes in the electrochemical behavior were examined by the addition of 35 μM SPS. Figures 5.8(a)–(c) exhibit the results of CA performed at -0.10 V, -0.15 V, and -0.2 V with fresh and aged electrolytes. As shown in Figures 5.8(a)–(c), the currents initially increased, and then converged to the

values, collectively referred to as the saturation current density. The increase in the current density was attributed to the gradual displacement of the PEG-PPG–$Cl^-$ complex by SPS on the surface of Cu. The current density was finally saturated after few tens of seconds when the surface coverage of SPS and suppressor-$Cl^-$ reached an equilibrium. Figures 5.8(a)–(c) show that the saturation current density increased as the duration of aging increased. These results implied that the fragmented PEG-PPG was more easily displaced by SPS on the surface of Cu.

Similar CA experiments were performed on PEG of various MWs, as shown in Figure 5.8(d). The saturation current density increased as the average MW of PEG decreased. W. P. Dow *et al.* have suggested a dependence of the adsorption strength on the MW of PEG.[112] They explained that PEG with high MW interacted with many chloride ions that acted as the adsorption bridge between PEG and Cu surface. Therefore, PEG with higher MW strongly adsorbed on the surface of Cu, while the ones with lower MW were easily displaced. Based on Figures 5.8(a)–(d), it can be concluded that the increase in the saturation current density is due to the presence of fragmented PEG-PPG. As shown in Figure 5.6, the aged bath contained a large amount of small PEG-PPG, which was weakly adsorbed on the surface of Cu and easily displaced by SPS. Therefore, although

the recorded concentrations of PEG-PPG in fresh and aged baths were comparable, the aged bath showed a higher saturation current density.

In order to verify the influence of PEG-PPG aging on the properties of films, Cu films were deposited in the presence of SPS under conventional operating conditions. Figures 5.9(a)–(d) displays the surface morphologies, XRD patterns, grain sizes, and resistivities of Cu films deposited by fresh and aged electrolytes. As shown in Figure 5.9(a), Cu films deposited from both fresh and aged electrolytes show smooth surfaces without any defects or irregularities. All the Cu films had strong Cu (111) and relatively weak Cu (200), Cu (220), Cu (311), and Cu (222) orientations, regardless of the duration of aging (Figure 5.9(b)). However, as shown in Figure 5.9(c), the grain sizes of Cu (111) orientation calculated by Scherrer's equation indicated that the average Cu (111) grain size gradually decreased, and was finally reduced by 32.92 % after 35 hr of aging. It led to an increase in the electrical resistivity as a result of grain boundary scattering, although the differences was within the deviation (Figure 5.9(d)). Furthermore, the standard deviation of resistivity increased as the duration of aging increased because of the deviation of film thickness caused by the uniformity problem (not shown here). An analogous phenomenon was investigated by R. Maru *et al.* who reported that the average grain size of electrodeposited Cu films decreased as the MW of PEG decreased over the

MW range of 200 Da to 1000 Da. This suggested that the surface diffusion of the Cu adatoms was influenced by the MW of the suppressor.

As described in Figures 5.8–5.9, the small PEG-PPG accumulated in the aged plating solution influences both, electrochemical behavior and film properties. This implied that the aged solution finally lost its original performance and changed the properties of deposits, even though the concentration of PEG-PPG was controlled using CVS methods. The failure to record the amount of by-products limits the sustainable application of CVS in the monitoring of the plating solution. Therefore, the methods needed to monitor the amount of by-products need to be considered in the determination of the lifetime of plating solutions.

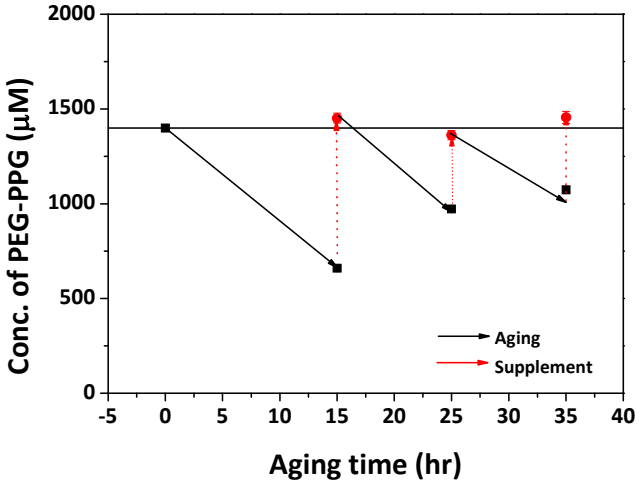


**Figure 5.5.** Changes in PEG-PPG concentrations; amount of PEG-PPG consumed during aging was periodically supplied at intervals of 15 hr, 25 hr, and 35 hr based on electrochemically calculated values of CVS measurements.

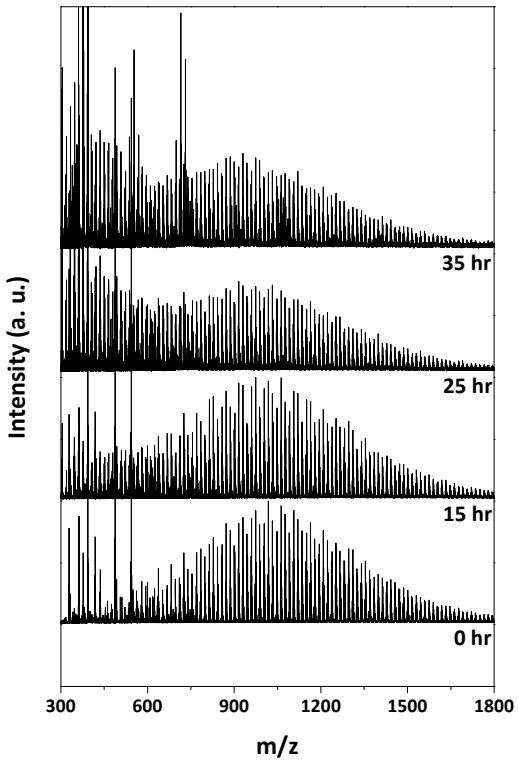


**Figure 5.6.** MALDI-TOF spetra of PEG-PPG after 0 hr, 15 hr, 25 hr, and 35 hr of aging and periodic addition of supplement. The analyses were carried out just after the addition of PEG-PPG supplement as shown in Figure 5.4.

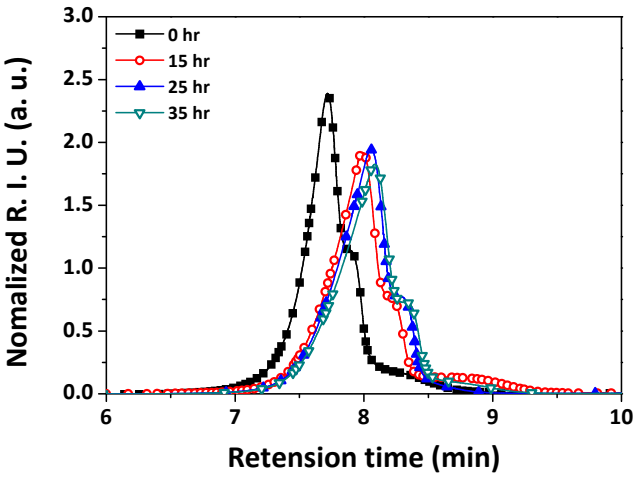


**Figure 5.7.** GPC spectra of PEG-PPG after 0 hr, 15 hr, 25 hr, and 35 hr of aging and periodic addition of supplement. The analyses were carried out just after the addition of PEG-PPG supplement as shown in Figure 5.4.

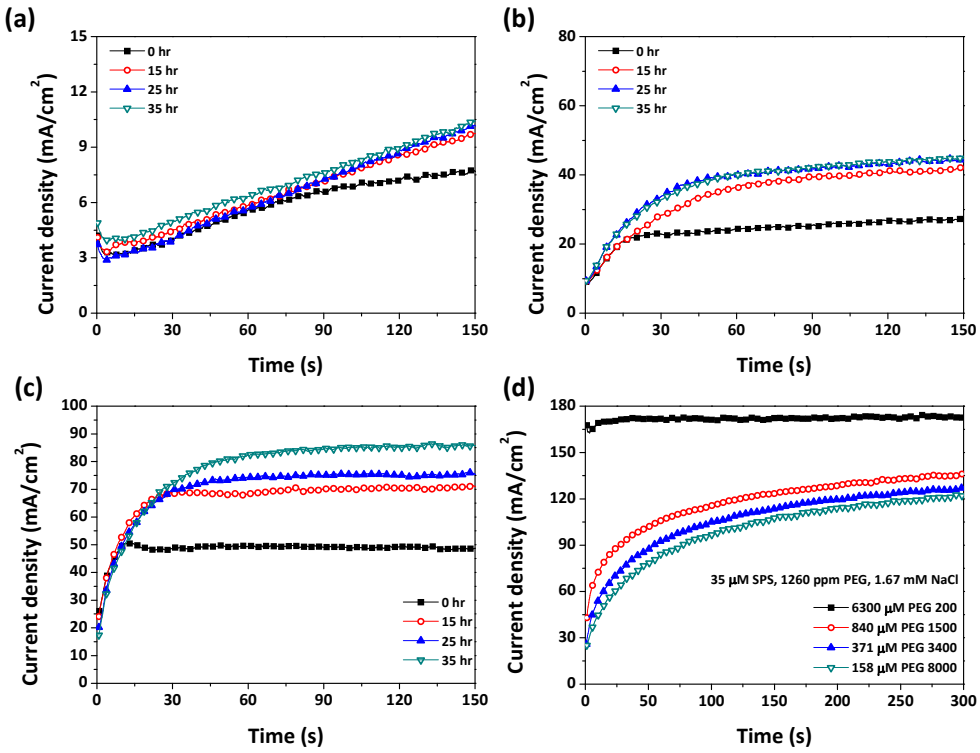


**Figure 5.8.** CAs of fresh and aged electrolytes after addition of 35 µM SPS at (a) -0.10 V, (b) -0.15 V, and (c) -0.2 V.(d) Additional CAs in fresh electrolytes containing 35 µM SPS, and 1.67 mM NaCl and PEG of various MWs and concentrations. The mass concentrations of PEGs were fixed at 1260 ppm to maintain the concentration of monomers. Aging of electrolyte was carried out through electrodeposition and periodic addition of PEG-PPG supplement as depicted in Figure 5.4.

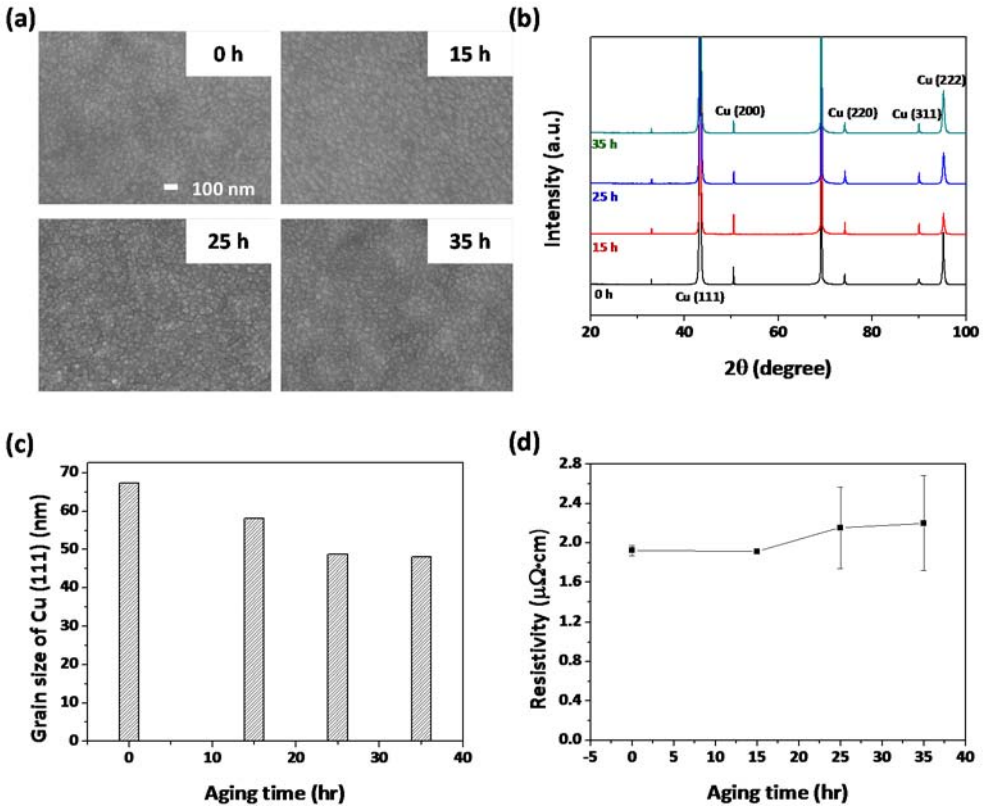


**Figure 5.9.** (a) Surface morphology, (b) XRD spectra, (c) Cu (111) grain sizes calculated using Scherrer's equation, and (d) resistivities of Cu films obtained from fresh and aged electrolytes. 35 μM SPS was added to the electrolyte prior to electrodeposition. Aging of electrolyte was carried out through electrodeposition and periodic addition of PEG-PPG supplement as depicted in Figure 5.4.

## 5.3. Summary

In this study, we observed that PEG-PPG decomposed during electrodeposition. The resulting by-products were small PEG-PPG containing aldehyde, formic ester, ketone, and propyl as terminal functional groups. Since the fragmented PEG-PPG also showed a suppression effect on Cu electrodeposition, it influenced the concentration values in CVS measurements and interrupted the precise control of PEG-PPG concentration. Therefore, the electrochemical behavior of the electrolyte and properties of the electrodeposited Cu films significantly changed with the aging, even though the PEG-PPG concentration was maintained using the conventional CVS method. Consequently, additional methods to monitor the amount of by-products are required for the long-term usage of the plating solution.

# Chapter VI. Conclusion

This study comprehensively described the additive decomposition phenomenon during Cu electrodeposition and suggested the modified methods to evaluate the concentrations of both the parent additives and its breakdown products.

SPS, one of the most common accelerator, decomposes into MPS and PDS during Cu electrodeposition via the electro-oxidation reaction at anode and the sequential chemical oxidation with molecular oxygen. The decomposition of SPS results in the degradation of filling capability and the decrease of electrochemical acceleration effect. One of the breakdown product, PDS, was gradually accumulated in bath during Cu electrodeposition. However, the influences of PDS on electrochemical behavior and film properties were negligible due to the absence of critical functional groups enabling to form the linkage on Cu surface. These results imply that the conversion of SPS into PDS results in just the deactivation of SPS without any further side effect.

Unlike PDS, MPS exerts significant effects on both the $Cu^{2+}$ reduction kinetics and filling capabilities of plating solution. MPS strongly adsorbs on Cu surface and accelerates the Cu reduction rate through both competitive adsorption and catalytic action on $Cu^{2+}$ reduction to $Cu^{+}$. It leads to the inaccurate results during MLAT-CVS

analysis of SPS concentration. Besides, the presence of MPS significantly deteriorates the filling capability of plating bath. Those aspects indicated that MPS concentration in Cu plating bath is also critical factor and the method to measure both SPS and MPS concentrations has to be developed for the accurate diagnosis of plating bath.

In order to evaluate the concentration of SPS and MPS individually, a modified two-step MLAT-CVS method was suggested, in which $C_T$ and $X_S$ are evaluated to yield $C_S$ and $C_M$. In order to obtain $C_T$, the condition of $X_S = 0$ was established by intentional pH control of the target plating solution, whereby MLAT-CVS analysis could reveal $C_T$ without the interference of MPS. $C_T$ was then converted to individual concentrations, $C_S$ and $C_M$, using $X_S$ evaluated from the difference of the relative accelerating abilities between SPS and MPS. This modified method quickly provided $C_S$ and $C_M$ of the sample baths with less than 10% error, enabling the accurate prediction of the filling performance of the solution without actual filling tests.

The decomposition of PEG-PPG, a suppressor additive, during Cu electrodeposition is also investigated here. Although the detail mechanism is unclear, the breakdown of PEG-PPG seems to occur via the oxidation of ether bond in backbones, forming the oxidative terminal groups like aldehyde, formic ester, ketone, and propyl. Since the fragmented PEG-PPG are accumulated in Cu plating bath, the MW distribution of PEG-PPG

gradually changes as the aging time increases. Therefore, the characteristics of aged bath, including its electrochemical behavior and the quality of products, are significantly changed during aging, even though the PEG-PPG concentration is tightly maintained by the periodical feeding of fresh PEG-PPG. Those results indicates that the additional methods to monitor the molecular distribution of PEG-PPG are required for the long-term usage of the plating solution.

In conclusion, the decomposition of organic additives significantly affect the quality of plating bath, and the concentrations of breakdown products as well as their parent additives have to be tightly monitored for accurate diagnosis of bath performances. Suggested results can provide the guideline for the development of advanced monitoring tools that offer more accurate predictions of bath performance without actual tests.

# Reference

[1] International Technology Roadmap for Semiconductors (ITRS), Semiconductor Industrial Association, 2013.

[2] P. C. Andricacos, C. Uzoh, J. O. Dukovic, J. Horkans, and H. Delihianni, *IBM J, Res. Dev*., **42**, 567 (1998).

[3] M. T. Bohr, Proc. *IEEE IEDM Tech. Dig.*, **241** (1995).

[4] S. P. Muraka, *Microelectron. Eng*., **29**, 37 (1997).

[5] G. Schneider, D. Hamback, B. Niemann, B. Kaulich, J. Susini, N. Hoffmann, and W. Hasse, *Appl. Phys. Lett.*, **78**, 1936 (2001).

[6] T. P. Moffat, D. Wheeler, and D. Josell. *J. Electrochem. Soc.*, **151**, C262 (2004).

[7] K. Kondo, N. Yamakawa, Z. Tanaka, and K. Hayashi, *J. Electroanal. Chem*., **559**, 137 (2003).

[8] E. J. Ahn and J. J. Kim, *Electrochem. Solid-State Lett.*, **7**, C118 (2004).

[9] J. J. Kim, S.-K. Kim, and J.-U. Bae. *Thin Solid Films*, **415**, 101 (2002).

[10] T. P. Moffat, J. E. Bonevich, H. Huber, A. Stanishevsky, D. R. Kelly, G. R. Stafford, and D. Josell, *J. Electrochem. Soc*., **147**, 4524 (2000).

[11] D. Josell, D. Wheeler, W. H. Huber, J. E. Bonevich, and T. P. Moffat, *J. Electrochem. Soc*., **148**, C767 (2001).

[12] T. P. Moffat, D. Wheeler, S.-K. Kim, and D. Josell, *J. Electrochem. Soc.*, **153**, C127 (2006).

[13] D. Wheeler, D. Josell, and T. P. Moffat, *J. Electrochem. Soc.*, **150**, C302 (2003).

[14] S. -K. Kim, S. K. Cho, J. J. Kim, and Y. -S. Lee, *Electrochem. Solid-State Lett.*, **8**, C19 (2005).

[15] D. Josell, D. Wheeler, C. Witt, and T. P. Moffat, *Electrochem. Solid-State Lett.*, **6**, C143 (2003).

[16] S. T. Lim, Y. C. Park, S. J. Yoo, and B. J. Lee, *Thin Solid Films*, **517**, 3935 (2009).

[17] J. Guillan, K. Haxaire, S. Chhun, E. Richard, M. C. Luche, L. Arnaud, E. Petitprez, C. Monget, D. Galpin, and P. Normandon, *Microelectron. Eng.*, **88**, 697 (2011).

[18] T. Karabacak and T.-M. Lu, *J. Appl. Phys.*, **97**, 124504 (2005).

[19] J. Reid, *Jpn. J. Appl. Phys.*, **40**, 2650 (2001).

[20] C. H. Lee, S. Hwang, S.-C. Kim, and J. J. Kim, *Electrochem. Solid-State Lett.*, **9**, C157 (2006).

[21] H. Kim, H. B. Bhandari, S. Xu, and R. G. Gordon, *J. Electrochem. Soc.*, **155**, H496 (2008).

[22] B. S. Lim, A. Rahtu, and R. G. Gordon, *Nat. Mater.*, **2**, 749 (2003).

[23] S. Choe, M. J. Kim, H. C. Kim, T. Lim, K. J. Park, S. K. Cho, S.-K. Kim, and J. J. Kim, *J. Electrochem. Soc.*, **160**, D202 (2013).

[24] M. J. Kim, H. J. Lee, S. H. Yong, O. J. Kwon, S.-K. Kim, and J. J. Kim, *J. Electrochem. Soc.*, **159**, D253 (2012).

[25] M. J. Kim, S. K. Cho, H.-C. Koo, T. Lim, K. J. Park, and J. J. Kim, *J. Electrochem. Soc.*, **157**, D564 (2010).

[26] M. J. Kim, K. J. Park, T. Lim, O. J. Kwon, and J. J. Kim, *J. Electrochem. Soc.*, **160**, D3081 (2013).

[27] M. J. Kim, T. Lim, K. J. Park, S.-K. Kim, and J. J. Kim, *J. Electrochem. Soc.*, **160**, D3088 (2013).

[28] Y. F. Shen, L. Lu, Q. H. Lu, Z. H. Jin, and K. Lu, *Scr. Mater.*, **52**, 989 (2005).

[29] E. Ma, and Y. M. Wang, Q. H. Lu, M. L. Sui, L. Lu, and K. Lu, *Appl. Phys. Lett.*, **85**, 4932 (2004).

[30] L. Lu, Y. Shen, X. Chen, L. Qian, and K. Lu, *Science*, **304**, 422 (2004).

[31] L. Lu, X. Chen, X. Huang, and K. Lu, *Science*, **323**, 607 (2009).

[32] J. W. Gallaway and A. C. West, *J. Electrochem. Soc.*, **155**, D639 (2008).

[33] J. W. Gallaway, M. J. Willey, and A. C. West, *J. Electrochem. Soc.*, **156**, C287 (2009).

[34] M. E. H. Garrido and M. D. Pritzker, *J. Electrochem. Soc.*, **155**, D332 (2008).

[35] M. L. Walker, L. J. Richter, and T. P. Moffat, *J. Electrochem. Soc.*, **152**, C403 (2005).

[36] K. R. Hebert, S. Adhikari, and J. E. Houser, *J. Electrochem. Soc.*, **152**, C324 (2005).

[37] L. Bonou, M. Eyraud, R. Denoyel, Y. Massiani, *Electrochimica Acta*, **47**, 4139 (2002).

[38] Z. V. Feng, X. Li, and A. A. Gewirth, *J. Phys. Chem. B*, **107**, 9415 (2003).

[39] J. P. Healy, D. Pletcher, and M. Goodenough, *J. Electroanal. Chem.*, **338**, 155 (1992).

[40] M. L. Walker, L. J. Richter, and T. P. Moffat, *J. Electrochem. Soc.*, **154**, D277 (2007).

[41] M. J. Willey and A. C. West, *J. Electrochem. Soc.*, **154**, D156 (2007).

[42] S. -K. Kim and J. J. Kim, *Electrochem. Solid-State Lett.*, **7**, C98 (2004).

[43] S. K. Cho, S.-K. Kim, and J. J. Kim, *J. Electrochem. Soc*., **152**, C330 (2005).

[44] N. T. M. Hai, K. W. Krämera, A. Fluegel, M. Arnold, D. Mayer, and P. Broekmann, *Electrochim. Acta*, **83**, 367 (2012).

[45] T. P. Moffat, D. Wheeler, S. -K. Kim, and D. Josell, *Electrochim. Acta*, **53**, 145 (2006).

[46] A. C. West, S. Mayer, and J. Reid, *Electrochem. Solid-State Lett*., **4**, C50 (2001).

[47] B. Bozzini, L. D'Urzo, V. Romanello, and C. Mele, *J. Electrochem. Soc.*, **153**, C54 (2006).

[48] S. K. Cho, M. J. Kim, H. -C. Koo, O. J. Kwon, and J. J. Kim, *Thin Solid Film*, **520**, 2136 (2012).

[49] B. Bozzini, L. D'Urzo, M. re, and F. D. Riccardis, *J. Appl. Electrochem*., **38**, 1561 (2008).

[50] S.-K. Kim, S. Hwang, S. K. Cho, and J. J. Kim, *Electrochem. Solid-State Lett*., **9**, C25 (2006).

[51] S.-K. Kim, D. Josell, and T. P. Moffat, *J. Electrochem. Soc.,* **153**, C616 (2006).

[52] S.-K. Kim, D. Josell, and T. P. Moffat, *J. Electrochem. Soc.*, **153**, C826 (2006).

[53] P. Broekmann, A. Fluegel, C. Emnet, M. Arnold, C. Roeger-Goepfert, A. Wagner, N.T.M. Hai, and D. Mayer, *Electrochim. Acta*, **56**, 4724 (2011).

[54] T. P. Moffat, D. Wheeler, M. D. Edelstein, and D. Josell, *IBM J. Res. & Dev.*, **49**, 19 (2005).

[55] D. Josell and T. P. Moffat, *J. Electrochem. Soc.*, **154**, D2008 (2007).

[56] M. J. Kim, Y. Seo, H. C. Kim, Y. Lee, S. Choe, Y, G. Kim, S. K. Cho, and J. J. Kim, *Electrochim. Acta*, **163**, 174 (2015).

[57] S. M. Huang, C. W. Liu, and W. -P. Dow, *J. Electrochem. Soc.*, **159**, D135 (2012).

[58] W. -P. Dow, H. -S. Huang, M. -Y. Yen, and H. -C. Huang, *J. Electrochem. Soc*., **152**, C425 (2005).

[59] T. P Moffat and D. Josell, *J. Electrochem. Soc*., **159**, D208 (2012).

[60] D. Josell, T. P. Moffat, *J. Electrochem. Soc*., **162**, D129 (2015).

[61] S.-K. Kim, J. E. Bonevich, D. Josell, and T. P. Moffat, *J. Electrochem. Soc.*, **154**, D443 (2007).

[62] D. Josell and T. P. Moffat, *J. Electrochem. Soc.*, **160**, D3035 (2013).

[63] S. Choe, M. J. Kim, H. C. Kim, S. K. Cho, S. H. Ahn, S.-K. Kim, and J. J. Kim, *J. Electrochem. Soc.*, **160**, D3179 (2013).

[64] W. -H. Lee, C. -C. Hung, S. -C. Chang, and Y. -L. Wang, *J. Electrochem. Soc*., **157**, H131 (2010).

[65] C. -C. Hung, W. -H. Lee, S. -Y. Hu, S. -C. Chang, K. -W. Chen, and Y. -L. Wang, *J. Vac. Sci. Technol. B*, **26**, 255 (2008).

[66] W. Wang, Y. -B. Li, and Y. -L. Li, *Appl. Surf. Sci*., **255**, 4389 (2009).

[67] J. P. Healy and D. Pletcher, *J. Electroanal. Chem.*, **338**, 167 (1992).

[68] L. D'Urzo, H. Wang, A. Pa, and C. Zhi, *J. Electrochem. Soc*., **152**, C243 (2005).

[69] L. T. Koh, G. Z. You, S. Y. Lim, C. Y. Li, and P. D. Foo, *Microelectron. J*., **32**, 973 (2001).

[70] S. -I Imai, M. Kitabata, and T. Tanaka, Advanced Semiconductor Manufacturing Conference (2009).

[71] A. Frank and A. J. Bard, *J. Electrochem. Soc.,* **150**, C244 (2003).

[72] Y. -B. Li, W. Wang, and Y. -L. Li, *J. Electrochem. Soc.*, **156**, D119 (2009).

[73] S. Choe, M. J. Kim, H. C. Kim, T. Lim, K. J. Park, K. H. Kim, S. H. Ahn, A. Lee, S.-K. Kim, and J. J. Kim, *J. Electroanal. Chem.*, **714-715**, 85 (2014).

[74] L. D'Urzo, H. Wang, C. Tang, A. Pa, and C. Zhi, *J. Electrochem. Soc*., **152**, C697 (2005).

[75] Y. S. Won, D. Cho, Y. Kim, J. Lee, and S. S. Park, *J. Appl. Polym. Sci.*, **117**, 2083 (2010).

[76] J. -M. Shieh, S. -C. Chang, B. -T. Dai, and M. -S. Feng, *Jpn. J. Appl. Phys.*, **41**, 6347 (2002).

[77] F. Wafula, L. Yin, P. Borgesen, D. Andala, and N. Dimitrov, *J. Electron. Mater.*, **41**, 1898 (2012).

[78] A. Barriola, J. I. Miranda, M. Ostra, and C. Ubide., *Anal. Bioanal. Chem.*, **398**, 1085 (2010).

[79] M. Ostra, C. Ubide, and M. Vidal, *Anal. Bioanal. Chem.*, **399**, 1907 (2011).

[80] A. Barriola, E. Garcia, M. Ostra, and C. Ubide, *J. Electrochem. Soc*., **155**, D480 (2008).

[81] C. Gabrielli, P. Mocoteguy, H. Perrot, A. Zdunek, and D. Nieto-Sanz, *J. Electrochem. Soc.*, **154**, D163 (2007).

[82] N. T. M. Hai, K. W. Krämera, A. Fluegel, M. Arnold, D. Mayer, and P. Broekmann, *Electrochim. Acta*, **83**, 367 (2012).

[83] N. T. M. Hai, T. T. M. Huynh, A. Fluegel, M. Arnold, D. Mayer, W. Reckien, T. Bredow, and P. Broekmann, *Electrochim. Acta*, **70**, 286 (2012).

[84] J. J. Kim, S. -K. Kim, Y. S. Kim, *J. Electroanal. Chem*., **542**, 61 (2003).

[85] M. A. Pasquale, A. E. Bolzan, J. A. Guida, R. C. V. Piatti, A. J. Arvia, O. E. Piro, and E. E. Castellano, *Solid State Sci.*, **9**, 862 (2007).

[86] C. C. Chen and K. J. Rajeshwar, *J. Electrochem. Soc*., **141**, 2942 (1994).

[87] K. -W. Kim, E. -H. Lee, J. -S. Kim, K. -H. Shin, and B. -I. Jung, *Electrochem. Acta*, **47**, 2525, (2002).

[88] T. P. Moffat, B. Baker, D. Wheeler, and D. Josell, *Electrochem. Solid-State Lett.*, **6**, C59 (2003).

[89] M. Pavlov, E. Shalyt, and P. Bratin, US Patent 7291253 (2007).

[90] B. -G. Xie, J. -J. Sun, X. -B. Chem, J. -H. Chen, T. -L. Xiang, and G. -N. Chen, *J. Electrochem. Soc.*, **154**, D516 (2007).

[91] N. Xiao, D. Li, G. Cui, N. Li, Q. LI, and G. Wu, *Electrochim. Acta*, **116**, 284 (2014).

[92] S. Choe, M. J. Kim, K. H. Kim, H. C. Kim, J. C. Song, S. -K. Kim, and J. J. Kim, *J. Electrochem. Soc.*, **162**, H294 (2015).

[93] C. D. Ellis, M. C. Hamilton, J. R. Nakamura, and B. M. Wilamowski, *IEEE Trans. Compon. Packag. Manuf. Technol.*, **4**, 1380 (2014).

[94] D. Tench and J. White, *J. Electrochem. Soc*., **132**, D516 (1985).

[95] C. Gabrielli, P. Mocoteguy, H. Perrot, D. Nieto-Sanz, and A. Zdunek, *J. Appl. Electrochem.*, **38**, 457 (2008).

[96] H J. Bowley, E. A. Crathorne, and D. L. Gerrard, *Analyst*, **111**, 539, (1986).

[97] R. Palmans, S. Claes, L. E. Vanatta, and D. E. Coleman, *J. Chromatogr. A*. **1085**, 147 (2005).

[98] J. Rethmeier, G. Neumann, C. Stumpf, A. Rabenstein, C. Vogt, *J. Chromatogr. A*, **934**, 129 (2005).

[99] T. P. Moffat and L.-Y. O. Yang, *J. Electrochem. Soc.*, **157**, D228 (2010).

[100] M. Tan, C. Guymon, D. R. Wheeler, and J. N. Harb, *J. Electrochem. Soc.*, **154**, D78 (2007).

[101] F. J. Monahan, J. B. German, and J. E. Kinsella, *J. Agric. Food Chem.*, **43**, 46 (1995).

[102] E. Garcia-Cardona, E.H. Wong, and D.P. Barkey, *J. Electrochem. Soc.*, **158**, D143 (2011).

[103] M. J. West, M. R. Anderson, Q. Wang, T. H. Bailey, Advanced Semiconductor Manufacturing, IEEE Conference and Workshop, 492-497 (2004).

[104] M. J. West, M. R. Anderson, Q. Wang, and T. H. Bailey, Electrochemical Processes in ULSI and MEMS: Deligianni, Moffat, Mayer and Stafford, ECS Processing, 41-56. (2005).

[105] G. Gallet, S. Carroccio, P. Rizzarelli, and S. Karlsson, *Polym.*, **43**, 1081 (2002).

[106] S. Han, C. Kim, and D. Kwon, *Polym. Degrad. Stab.*, **47**, 203 (1995).

[107] S. Han, C. Kim, and D. Kwon, *Polym.*, **38**, 317 (1997).

[108] L. Yang, F. Heatley, T. G. Blease, and R. I. G. Thompson, *Eur. Polym. J.*, **32**, 535 (1996).

[109] M. A. Semsarzadeh, and H. Salehi, *Eur. Polym. J.*, **35**, 1001 (2000).

[110] R. Manu and S. Jayakrishnan, *Bull. Mater. Sci.*, **34**, 347 (2011).

[111] S. -L. Ko, J. -Y. Lin, Y. -Y. Wang, and C. -C. Wan, *Thin Solid Films*, **516**, 5046 (2008).

[112] W. -P. Dow, M. -Y. Yen, W. -B. Lin, S. -W. Ho, *J. Electrochem. Soc.*, **152**, C769 (2005).

# 국문초록

구리 전해 도금은 높은 생산성과 낮은 공정 단가로 우수한 특성을 가지는 구리 박막을 전착시킬 수 있다는 장점을 가져 여러 산업에서 널리 응용 되고 있다. 도금을 위한 전해질 내부에는 대부분의 경우 소량의 유기 첨가제가 포함되어 있으며, 이들의 첨가는 도금된 박막의 표면 형상 조절과 더불어 물리적, 기계적 특성 변화를 유도한다. 그러나 이들은 전해 조건에서 불안정하기 때문에, 도금 과정 중에 여러 화학적/전기화학적인 과정을 거쳐 분해가 진행된다. 이러한 첨가제 분해 현상은 도금액 특성을 저하시키는 원인이 되며, 이를 막기 위해 보통 도금액의 첨가제 농도는 cyclic voltammetry stripping (CVS) 등의 여러 전기화학적 모니터링법과 첨가제 보충을 통해 일정하게 관리 된다.

그러나 이러한 노력에도 불구하고 도금액 성능 저하는 막기 어렵다. 이것은 지속적인 첨가제 분해로 인해 분해 산물이 축적되고, 이들이 박막 특성에 영향을 줌과 동시에, 정확한 첨가제 농도 모니터링을 방해하기 때문이다. 따라서 첨가제와 더불어 분해 산물의 농도를 동시에 측정할 수 있는 방법의

개발이 요구되고 있다. 본 연구에서는 첨가제 분해 산물이 구리 전해 도금에 미치는 영향을 확인하고, 첨가제와 분해 산물의 농도 모두를 측정할 수 있는 방법을 제시하였다.

Bis(3-sulfopropyl) disulfide (SPS)를 첨가한 도금액을 120 분 이상 열화시키는 경우 도금액이 가진 채움 특성 저하와, SPS 의 전기화학적 가속 효과 감소가 관측 되었다. 이것은 도금액 구동 과정에서 SPS 의 전기화학적 산화 반응이 부반응으로 발생하여 SPS 가 분해되고 분해산물인 3-mercapto-1-propane sulfonate (MPS)와 1,3-propane sulfonic acid (PDS)가 생성되었기 때문이다. 차후 진행된 실험에서 최종 분해산물인 PDS 는 과량이 포함되었다 하더라도 도금 과정에 미치는 영향이 미미하다는 것을 확인하였다. 이는 PDS 가 도금액 표면에 흡착할 수 있는 작용기가 없어 구리 박막 표면에 흡착하기 어렵기 때문이라 추측된다. 그러나 중간 분해 산물인 MPS 의 경우 구리 전해 도금에 강한 가속 효과를 가졌으며, 이에 따라 SPS 농도 측정을 위한 MLAT-CVS 분석 결과에 오차를 유발시켰다. 더불어 MPS 는 도금액의 채움 특성 역시 저해시키는 결과를 불러왔다. 이러한 측면들은 SPS 농도뿐만 아니라 MPS

농도 역시 도금액 특성에 중요한 요소임을 암시하였기 때문에 이들을 모두 측정하기 위한 두 단계 CVS 법이 제시 되었다.

두 단계 CVS 법은 전체 가속제 농도합([SPS] + 1/2[MPS])과 전환률이라고 명명된 두 가지의 변수 측정을 통해 도금액 내부의 SPS 와 MPS 농도를 동시에 측정하는 방법이다. 우선 첫 번째 단계에서 pH 조절을 통해 MPS 를 SPS 로 강제 산화시킨 이후 고안된 선형 근사법 ((MLAT)-CVS) 분석을 시행하여 도금액 내부의 전체 가속제 농도합이 산출되었다. 이후 두 번째 단계에서는 전환률에 따른 가속 효과 차이를 이용하여 전환률이 측정 되었고, 측정된 전환률을 통해 전체 가속제 농도합은 SPS 와 MPS 의 개별 농도로 환산되었다. 이 방법은 SPS 와 MPS 농도를 10% 내의 오차 범위에서 측정할 수 있어 구리 도금액 관리에 유용하게 사용될 수 있을 것으로 사료 된다.

감속제로 사용되는 poly(ethylene glycol-propylene glycol) (PEG-PPG) 역시 도금액 구동 과정에서 분해되었다. PEG-PPG 의 분해는 PEG-PPG 의 골격을 이루는 C-O 결합에서 발생하여 C-O 결합의 해리를 가져옴과 동시에 분자량을 감소시키는 결과를 수반하였다. 분해 반응은 이와 더불어 PEG-PPG 의 말단기를 formic acid, aldehyde, ketone 등의 산화된 형태로 변화시켰다.

한편 PEG-PPG 의 분해로 인해 저분자량의 PEG-PPG 가 도금액 내부에 축적되고 이는 PEG-PPG 의 평균 분자량 변화를 가져왔다. 이러한 효과로 인해 도금액이 가진 전기화학적 특성 변화와 더불어, 도금된 박막의 특성 저하가 관측되었다. 이는 PEG-PPG 의 농도뿐만이 아니라 분자량 변화 역시 중요한 공정 변수임을 나타내며, 이에 따라 PEG-PPG 의 분자량 변화까지 측정할 수 있는 모니터링법의 개발이 필요하다고 사료된다.

이러한 현상들을 종합해 봤을 때, 첨가제 분해로 생성되는 분해 산물 역시 도금액 특성을 결정짓는 중요한 요소라는 것을 확인할 수 있으며, 이에 따라 본래의 첨가제들뿐만이 아니라 이들의 분해 산물의 농도를 측정하는 방법의 개발이 요구된다. 본 연구에서 제시된 결과들은 차후 도금액 모니터링법 개발에 중요한 가이드라인을 제시해 줄 수 있을 것이라 사료 된다.

**주요어: 구리 전해 도금, 유기 첨가제, cyclic voltammetry stripping, bis(3-sulfopropyl) disulfide, poly(ethylene glycol-propylene glycol), 고안된 선형 근사법, 희석 적정법**

**학번: 2012-30260**

# Appendix I

## Accuracy Improvement in Cyclic Voltammetry Stripping Analysis of Thiourea Concentration in Cu Plating Baths

### 1. Introduction

This chapter describes another modified CVS analysis for accurate determination of thiourea (TU) concentration in Cu plating bath. TU is a common additive in Cu and Ag electrodeposition baths and induces leveling and grain refining properties.[1-9] TU has been used as an additive either solely or in combination with $Cl^-$ (TU-$Cl^-$) in baths used for electrodeposition processes involving various current/potential waveforms such as direct current, pulse-, or pulse-reverse waveforms.[3,4,6,7] Various applications of TU as an additive have been studied, including the formation of the Cu twin, Ag superfilling, and the fabrication of CuS nanowire structures.[1,2,6-9]

TU is known to form thiolate complexes such as $[Cu\text{-}(TU)]^{2+}$, $[Cu\text{-}TU]^{+}$, and $[Cu\text{-}(TU)_2]^{2+}$ with $Cu^{2+}$ ions in acidic Cu plating solutions.[3-12] Additionally, TU can be oxidized to formamidine disulfide (FDS), which forms other thiolate complexes with $Cu^{+}$ and $Cu^{2+}$ ions.[10-12] Owing to the various derivatives and their different electrochemical

responses, TU shows unique electrochemical behavior unlike typical suppressors or levelers. Although TU commonly reduces the Cu deposition rate, it often acts in an opposite role as an accelerator under specific conditions such as low concentrations and low overpotentials.[10-12] Several mechanisms explaining the accelerating effect of TU have been proposed.[10-12]

Generally, the reduction of $Cu^{2+}$ occurs in two steps, namely the reduction of $Cu^{2+}$ to $Cu^{+}$, followed by the reduction of $Cu^{+}$ to $Cu^{0}$. The first step has been known to be the rate-determining step. In the presence of TU, however, additional reactions occur, as described in Eq. 1.[10-12]

$$2Cu^{2+} + 2TU \leftrightarrow 2Cu^{+} + FDS + 2H^{+} \quad \text{[Eq. 1]}$$

Kim *et al.* reported the accelerating effect of derivatized TU on Cu electrodes.[10] Wang *et al.* observed the acceleration effect of TU at low concentrations (below 5 ppm), and explained it based on the relatively higher concentration of $[Cu\text{-}FDS]^{+}$ compared to $[Cu\text{-}TU]^{+}$ on the Cu surface.[11] Suarez *et al.* also suggested that the predominance of $[Cu\text{-}FDS]^{+}$ over $[Cu\text{-}(TU)]^{+}$ and $[Cu\text{-}(TU)]^{2+}$ at low overpotentials/low concentrations caused the accelerating effect.[12] They explained that the chain reaction involving the reaction described by Eq. 1, the reduction of $Cu^{+}$ to $Cu^{0}$, and the reduction of FDS to TU was stimulated at low overpotentials/low concentrations.[12]

Monitoring tools to determine TU concentrations in aqueous medium have been extensively studies elsewhere in purpose of application to the environmental and industrial issues.[13-15] One of the approaches included the electrochemical method based on the redox reactions between TU and FDS.[13] However, the application of electrochemical methods on the quantification of TU in Cu plating solution have been rarely reported in spite of focused researches on the behavior of TU.[1-12] The scarcity of literature on electrochemical monitoring methods for TU in particular is probably due to the unique electrochemical behavior of TU, resulting from its various reduced species and their different electrochemical responses depending on the TU concentration and the applied potential. Owing to the interference from the reduced species, it appears that conventional DT-CVS is unsuitable as a monitoring tool for determining the TU concentrations. Therefore, in this chapter, DT-CVS was modified to improve the accuracy of the measured TU concentrations in Cu plating baths by adding PEG into the base solution, in order to suppress the undesired electrochemical behavior of TU and its reduced species.

## 2. Experimental

Figure 1 shows the experimental set-up used in this study. Cu plating solutions consisting of 0.25 M $CuSO_4$, 1.0 M $H_2SO_4$, and 0~1.5 mM TU were used for the CVS and UV-visible spectroscopy experiments. UV-visible spectroscopic measurements (Thermo, Genesys-10) were carried out using deionized water as a blank solution.

CVS (Metrohm, 797A Computrace) was carried out in order to observe the electrochemical response of TU and to measure the normalized stripping charge ($Q/Q_{base}$). The standard Cu plating solution containing 0.25 M $CuSO_4$, 1.0 M $H_2SO_4$, and 1.4 mM TU was periodically added to the base solution. The volume of the base solution was 50 mL and the standard solution was periodically added in doses of 0.05 mL. CVS was carried out after each addition, to obtain the stripping charges, which were normalized as ($Q/Q_{base}$), where $Q_{base}$ was the stripping charge of the base solution. As shown in Figure 1, two types of base solutions were used in the CVS analyses. The conventional base solution, referred to as base solution 1 (BS1) was composed of 0.25 M $CuSO_4$, 1.0 M $H_2SO_4$, and 1.0 mM NaCl, whereas the modified base solution (BS2) was composed of 0.25 M $CuSO_4$, 1.0 M $H_2SO_4$, 1.0 mM NaCl, and 90 μM PEG with a molecular weight of 3400.

The electrochemical cell for CVS was composed of a Pt rotating disk electrode (RDE) with an active area of 3.14 $mm^2$, which acted as the cathode, a Pt rod anode, and an

Ag/AgCl [3 M KCl] reference electrode. The rotation speed of the Pt RDE during CVS was fixed at 2000 rpm, which is aimed to support mass transport of TU to the electrode surface, thereby enhancing the inhibiting ability of TU.[16] The voltammograms were obtained with a potential range from 1.575 V to the cathodic vertex potential (-0.1 V~-0.4 V) with a scan rate of 0.1 V/s.

The influence of the molecular weight of PEG on the CVS results was also studied. A small volume of the standard solution (0.05 mL) containing 0.25 M $CuSO_4$, 1.0 M $H_2SO_4$, and 1.4 mM TU was periodically added to BS2 solutions (50 mL) containing PEG with molecular weights of 1050 Da, 1500 Da, 3400 Da, and 8000 Da. CVS was carried out after every addition and the stripping charges were obtained. Cathodic vertex potentials for the analyses were fixed at -0.3 V.

Plots of $Q/Q_{base}$ as a function of TU-derivative concentration were obtained for TU-derivatives such as N-ethyl thiourea (ETU) and N',N-diethyl thiourea (DETU). Small volumes of the standard solutions (0.05 mL) containing 0.25 M $CuSO_4$, 1.0 M $H_2SO_4$, and 1.4 mM TU-derivatives were periodically added to either BS1 or BS2 solutions (50 mL). The cathodic vertex potentials for the analyses were fixed at -0.3 V.

The accuracy of DT-CVS was evaluated by comparing the real and measured values of the concentrations of the TU-derivatives. Standard solutions comprising of 0.25 M

$CuSO_4$, 1.0 M $H_2SO_4$, and 1.4 mM TU-derivatives were used to generate the calibration curve. The evaluation ratios were 0.8 and 0.6 for BS1 and BS2, respectively and the cathodic vertex potential for the analyses was fixed at -0.3 V. Using the calibration curve, the concentrations of the TU-derivatives in target solution in the range of 0.7-1.4 mM were measured and compared with the real values.

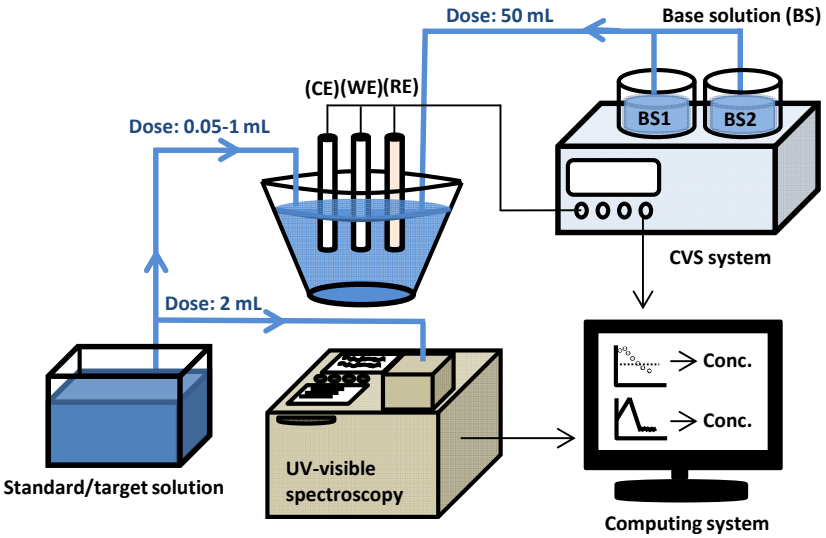


**Figure 1**. Schematic diagram of the experimental setup.

## 3. Results and Discussion

UV-visible spectroscopy was applied for the quantification of TU concentrations in Cu plating solutions. Figure 2(a) presents the UV-visible spectra of Cu plating solutions containing 0-1.5 mM TU. As shown in Figure 2(a), the Cu plating solutions containing TU exhibited peaks at 200-300 nm and 340 nm. The former peak resulted from the $Cu^{2+}$ in the plating solution and appeared to have an abnormal shape, since the absorbance exceeded the upper detection limit, owing to the high concentration of $Cu^{2+}$ in the plating solution. Considering the spectra of the individual components, the peak of pure TU was supposed to be at 235 nm. However, this peak was excluded from the analysis because it was buried under the large peak of $Cu^{2+}$.

Meanwhile, the intensity of the peak at 340 nm initially increased with TU concentration, and subsequently almost converged when the TU concentration was over 0.6 mM. The peak at 340 nm is known to originate from the d-orbital splitting of $Cu^{2+}$, during the formation of the $[Cu\text{-}(TU)]^{2+}$ complex.[17,18] As shown in Figure 2(b), the absorbance increased as the $Cu^{2+}$ concentration increased, confirming that the peak at 340 nm originated from the $[Cu\text{-}(TU)]^{2+}$ complex. The equilibrium among $Cu^{2+}$, TU, and the $[Cu\text{-}(TU)]^{2+}$ complex is described by Eq. 2 and Eq. 3.[17,18]

$$Cu^{2+} + TU \leftrightarrow [Cu - TU]^{2+} \quad [\text{Eq. } 2]$$

$$K = \frac{[Cu - Tu]^{2+}}{[Cu^{2+}][TU]} \quad [\text{Eq. } 3]$$

where K is the equilibrium constant. Figure 2(c) shows the absorbance at 340 nm as a function of the TU and $Cu^{2+}$ concentrations. As shown in the figure, the absorbance at 340 nm increased with an increase in the concentrations of TU and $Cu^{2+}$, owing to the equilibrium reaction described in Eq. 2.

When the concentration of $Cu^{2+}$ is significantly higher than that of TU, and the $[Cu\text{-}TU]^{2+}$ is the sole complex formed, the approximate relationship between the absorbance and the concentration of TU can be expressed by Eq. 4.[17]

$$\frac{[TU]_0}{A} = \frac{1}{\varepsilon b K [Cu^{2+}]_0} + \frac{1}{\varepsilon b} \quad [\text{Eq. } 4]$$

Here, A is absorbance, $\varepsilon$ is molar absorptivity, b is the cell length, $[Cu^{2+}]_0$ is the bulk concentration of $Cu^{2+}$, and $[TU]_0$ is the bulk concentration of TU. According to this equation, the absorbance and the concentration of TU are directly proportional to each other. However, as shown in Figure 2(c) and as reported in the literature[17], the relationship between the absorbance and the concentration of TU is non-linear, implying that there is a mismatch between the assumption made in arriving at Eq. 4 and the experimental results obtained. A possible explanation for the discrepancy could be the

formation of another complex with a higher coordination number such as $[Cu\text{-}(TU)_n]^{2+}$.[17] Based on these results, it appeared that monitoring the TU concentration with UV-visible spectroscopy is effective only in limited concentration ranges.

DT-CVS was also applied for the analysis of TU concentrations in Cu plating solutions. Prior to the application of DT-CVS, the electrochemical responses of TU were studied. Figures 3(a)-(c) present the CVS results in BS1 as the function of TU concentration. As shown in the figures, the addition of TU led to a slight decrease in the current density at all vertex potential values. The inhibition effect was associated with the adsorption of TU on the active sites of the Cu surface. Due to the inhibition effect of TU, the normalized stripping charge ($Q/Q_{base}$) decreased with TU concentration, as presented in Figure 3(d). The figure revealed that the absolute slope of the plot of $Q/Q_{base}$ versus TU concentration decreased as the vertex potential shifted negatively. This tendency appears to be related to the potential-dependent adsorption of TU.[19-23] It is known that the surface coverage of TU decreases as the cathodic overpotential increases because of hydrogen evolution,[19] TU decomposition,[20] and the electrical repulsion force between TU and the substrate.[21] It appears that the low surface coverage of TU at high overpotentials reduces the difference between Q and $Q_{base}$, resulting in the decrease in the slope of the plot of $Q/Q_{base}$.

However, as shown in Figure 3(d), the value of $Q/Q_{base}$ exceeded 1 at low TU concentrations and less negative vertex potentials, where the acceleration effect dominated the inhibition effect. In addition, $Q/Q_{base}$ decreased non-linearly at less negative vertex potentials (e.g., -0.10 V and -0.15 V). These results revealed the limitations of conventional DT-CVS for the determination of TU concentrations, namely a non-linear $Q/Q_{base}$ drop at less negative vertex potentials and relatively low TU concentrations due to the acceleration effect of TU and a less steep $Q/Q_{base}$ drop at highly negative vertex potentials as a result of the low surface coverage of TU.

It is expected that the elimination of the undesirable accelerating effect may contribute to an improvement in the linearity and the steepness of the $Q/Q_{base}$ drop in the DT-CVS analysis. One possible solution is the addition of PEG to the base solution, since PEG can suppress the accelerating effects by forming a PEG-$Cu^{+}$-$Cl^{-}$ complex[24-26] on the Cu surface. Figures 4(a)-(d) show the CVS results and the corresponding $Q/Q_{base}$ plot in the BS2 solution. As shown in the figures, the current density and the corresponding stripping charge of the base solution ($Q_{base}$) was significantly reduced in BS2 owing to the inhibition effect induced by the PEG-$Cu^{+}$-$Cl^{-}$ complex. Meanwhile, as shown in Figure 4(d), the use of BS2 resulted in a linear and steep $Q/Q_{base}$ drop even at highly negative vertex potentials. Note that an unusual $Q/Q_{base}$ drop behavior at the vertex

potential of -0.2 V might originate from the saturation of the TU adsorption sites due to the high coverage of PEG. In addition, the acceleration effect from TU clearly disappeared even at low concentrations. Therefore, the linear and steep $Q/Q_{base}$ drop appears to be related to the diminished acceleration effect due to the formation of PEG-$Cu^{+}$-$Cl^{-}$ on the Cu surface.

Another possibility is the suppression of TU desorption by the added PEG. Unlike the case of BS1, the slopes of the plots of $Q/Q_{base}$ versus TU concentration in the case of BS2 remained high even at very negative vertex potentials (Figure 4(d)). For confirmation, an additional CVS analysis was carried out with a high concentration of TU, and the results are presented in Figure 5. As shown in Figure 5(a), the suppression of Cu plating by TU appears to be effective only in the range of OCP~-0.2 V. At potentials more negative than -0.2 V, the current densities obtained from BS1+16.8 μM TU became comparable with that from BS1, implying that most of the TU desorbed from the electrodes. Likewise, when the vertex potential was more negative than -0.2 V, the current densities obtained from BS1+16.8 μM TU were almost the same with that from BS1 in the reverse scan, generating a hysteresis curve. The hysteresis curve generated by the sole action of the suppressor has been explained based on the delay between the desorption and the re-adsorption of the suppressor on the Cu surface.[24] As shown in Figure 5(a), a hysteresis

related to the desorption of TU was clearly observed for vertex potentials of -0.2 V and -0.3 V, whereas it was insignificant for a vertex potential of -0.1 V. However, in the case of BS2 (i.e., the solution containing PEG), while the hysteresis was not clear even at the vertex potential of -0.3 V, it became apparent at the vertex potential of -0.4 V, indicating that the desorption of TU was suppressed by PEG. (Figure 5(b))

The influence of the molecular weight of PEG in the BS2 solution was studied next. Figures 6(a)-(e) present the CVS results and the corresponding $Q/Q_{base}$ plot obtained in BS2 solutions containing PEG with various molecular weights. As shown in Figures 6(a)-(d), the hysteresis curve was clearly seen in the cases of low molecular weight PEG (i.e., for PEG with molecular weights of 1050 Da and 1500 Da), whereas it was insignificant in the case of high molecular weight PEG. This implied that PEG with high molecular weights suppressed either the accelerating effects of TU or the TU desorption itself, more strongly than PEG with low molecular weights. Consequently, the absolute slope of the plot of $Q/Q_{base}$ versus TU concentration increased with the molecular weight of PEG, as seen in Figure 6(e). S. Verma *et al.* reported that TU and PEG could form PEG-embedded TU complex structures.[27] The binding force between TU and PEG could retard the desorption of TU from PEG-covered Cu. Likewise, since the adsorption

strength of PEG on the Cu surface increased with molecular weight,[28,29] high-molecular-weight PEG could effectively suppress the desorption of TU.

In order to assess the suitability of this modification for monitoring the concentrations of the derivatives of TU; ETU, and DETU, the $Q/Q_{base}$ plots of TU, ETU, and DETU were obtained using either BS1 or BS2 as the base solutions. Figure 7 revealed that the slope of the $Q/Q_{base}$ plot in the case of BS2 was always higher than that in the case of BS1, regardless of the additives. Meanwhile, the slopes of the $Q/Q_{base}$ plots for the three cases were indistinguishable in the case of BS1, whereas the slopes showed differences according to the number of ethyl groups in the case of BS2. This effect probably came from the steric hindrance of the TU-derivatives during their adsorption on the PEG-covered Cu surface or the difference in the binding force between PEG and the TU-derivatives.

Based on the previous experiments, the concentrations of TU and its derivatives in plating solutions were measured by DT-CVS using either BS1 or BS2 as the base solution. Table 1 shows the difference between the real and measured concentrations of the TU-derivatives. As shown in Table 1, when BS2 was used, the errors between the real and measured concentrations were within 3.00%, 6.00%, and 6.00% for TU, ETU, and DETU, respectively, whereas the errors were originally about 15.0%, 36.0%, and 15.0%

for TU, ETU, and DETU when BS1 was used. The improvement in the measurements could be ascribed to the linear and steep $Q/Q_{base}$ drop in BS2 solution. This result demonstrated that the addition of PEG into the base solution enables precise quantification of the concentrations of the TU-derivatives using DT-CVS.

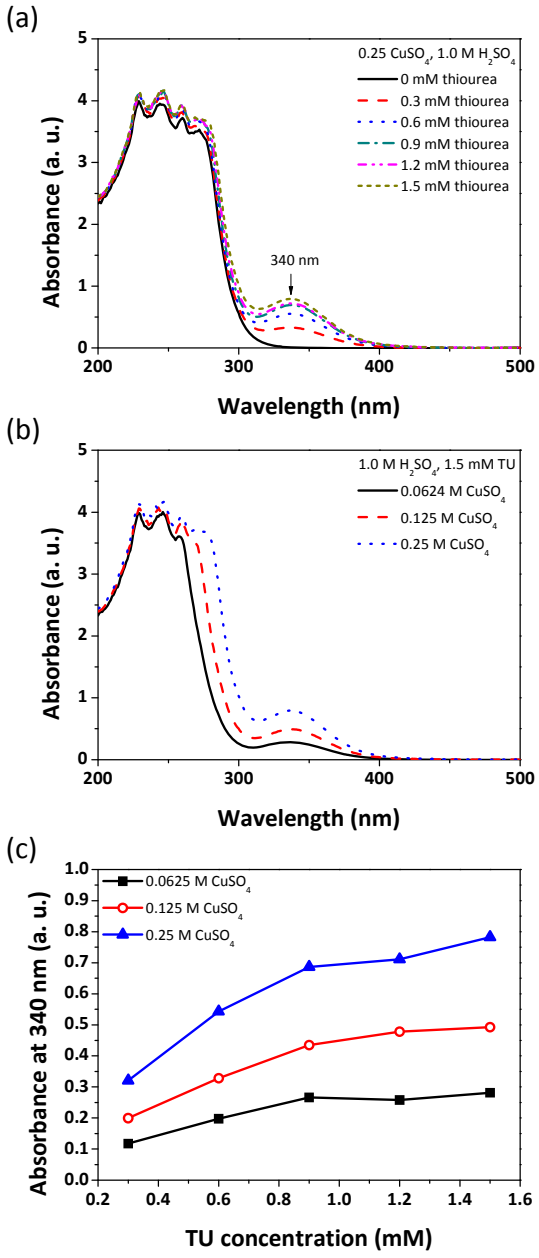


**Figure 2.** UV-visible spectra of the plating solutions containing various concentrations of (a) TU and (b) $CuSO_4$. The absorbance at 340 nm at various TU concentrations is shown in (c).

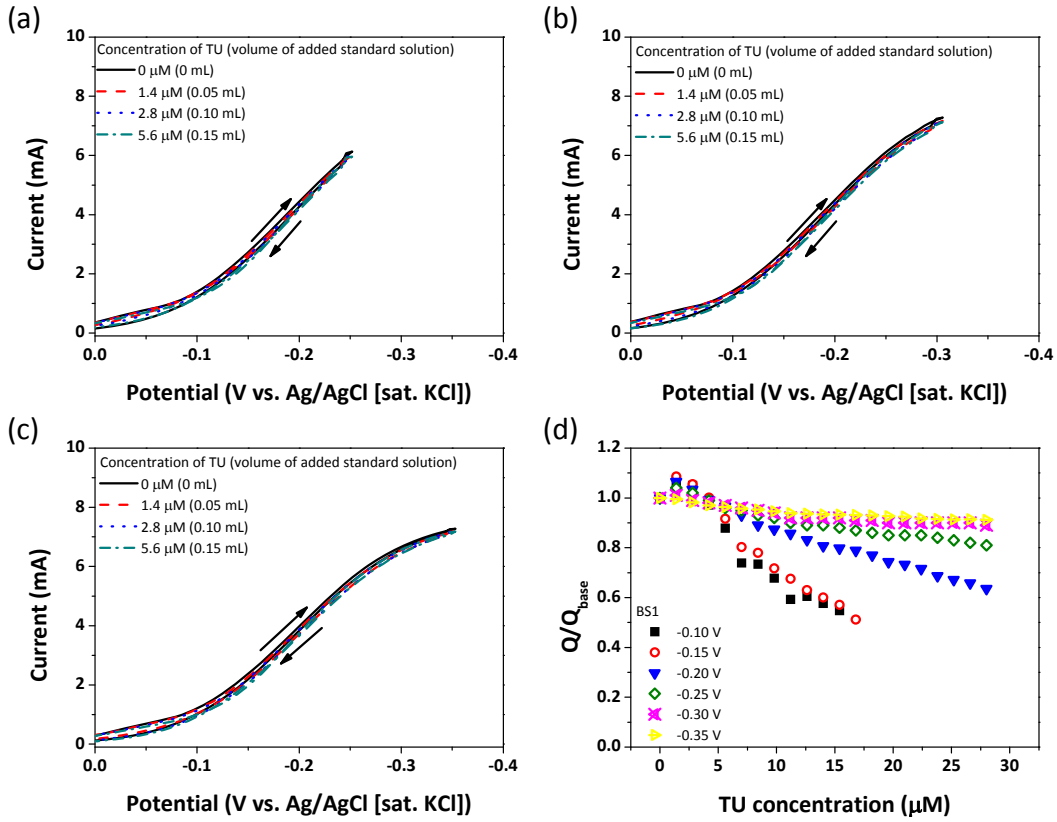


**Figure 3**. Voltammograms for Cu electrodeposition in BS1 solutions containing various concentrations of TU. (Note that the concentrations of TU are calculated after each additions of standard solutions into 50 mL base solution.) The vertex potentials are (a) -0.25 V, (b) -0.30 V, and (c) -0.35 V. The normalized stripping charges are shown in (d).

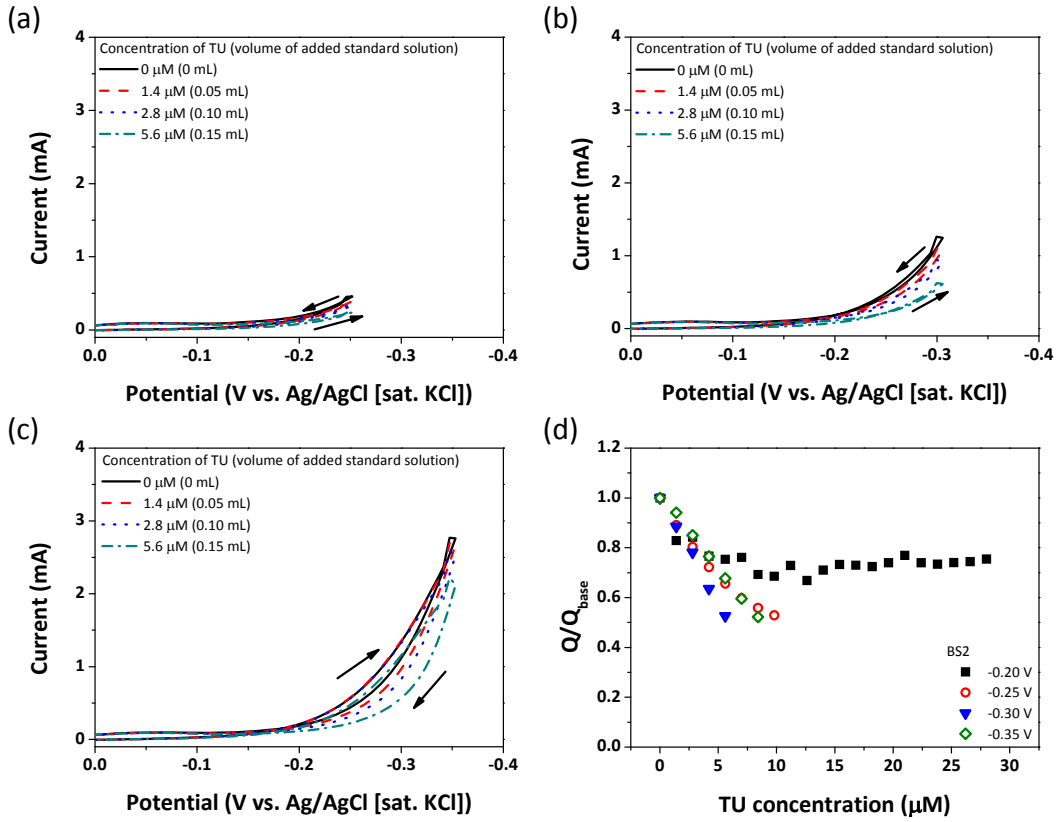


**Figure 4**. Voltammograms for Cu electrodeposition in BS2 solutions containing various concentrations of TU. (Note that the concentrations of TU are calculated after each additions of standard solutions into 50 mL base solution.) The vertex potentials are (a) -0.25 V, (b) -0.3 V, and (c) -0.35 V. The normalized stripping charges are shown in (d).

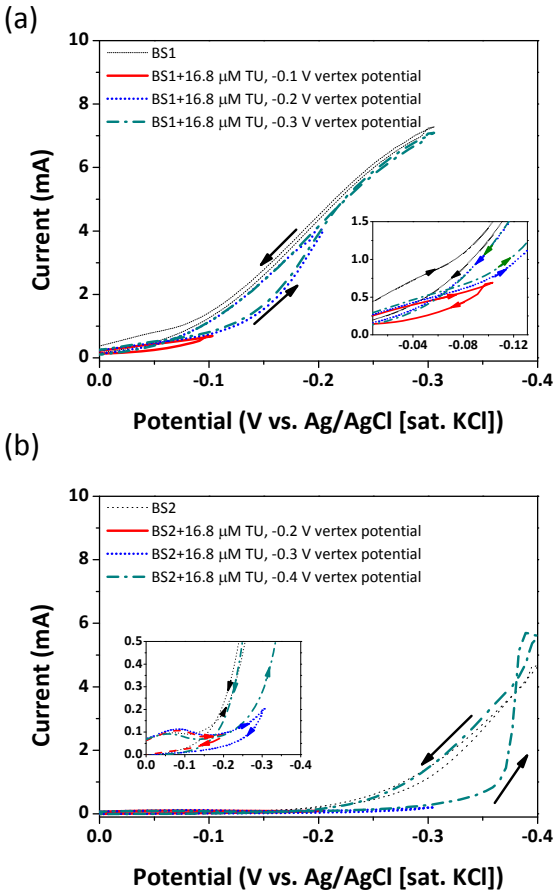


**Figure 5**. Voltammograms for Cu electrodeposition with various vertex potentials in (a) BS1 and (b) BS2 base solutions.

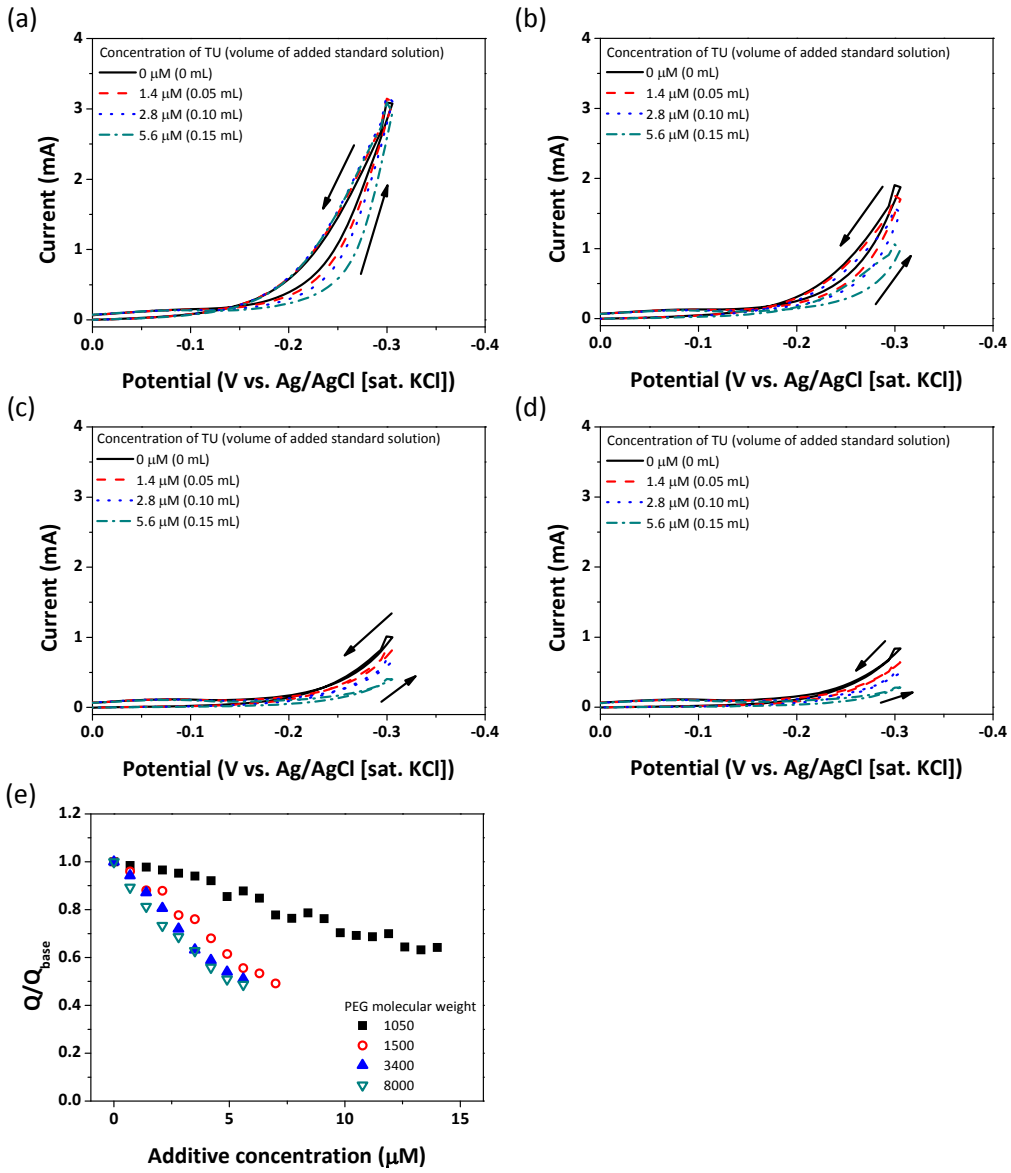


**Figure 6**. Voltammograms for Cu electrodeposition in BS2 solutions containing PEG with molecular weights of (a) 1050 Da, (b) 1500 Da, (c) 3400 Da, and (d) 8000 Da. (Note that the concentrations of TU are calculated after each additions of standard solutions into 50 mL base solution.) The normalized stripping charges are shown in (e).

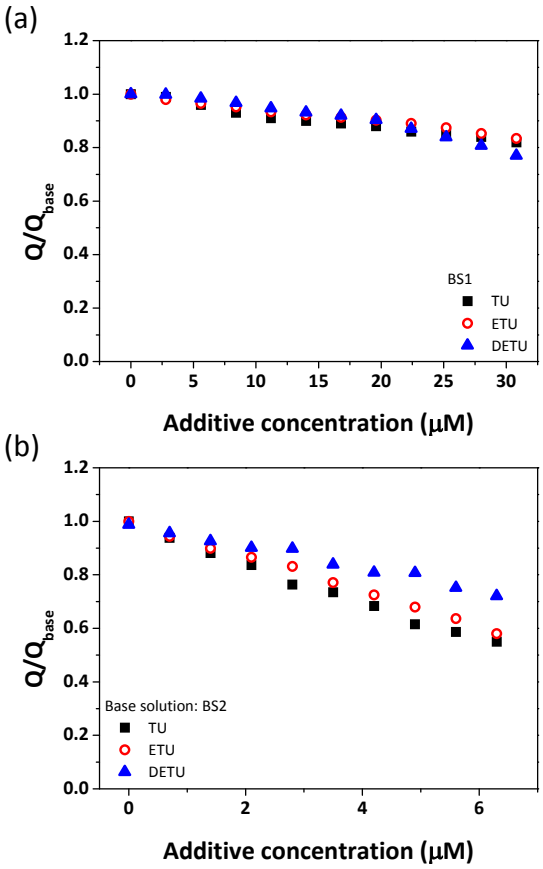


**Figure 7.** Normalized stripping charges as a function of the concentrations of TU-derivatives in (a) BS1 and (b) BS2 base solutions.

**Table 1**. Measured Concentrations of (a) TU, (b) ETU, and (c) DETU by DT-CVS in BS1 and BS2 Solutions and the Corresponding Errors between the Real And Measured Values.

| TU conc. (mM) | Measured in BS1 (mM) | Error (%) | Measured in BS2 (mM) | Error (%) |
|---|---|---|---|---|
| 0.70 | 0.62 | 10.9 | 0.71 | 1.43 |
| 1.05 | 0.90 | 14.2 | 1.08 | 2.76 |
| 1.40 | 1.35 | 3.57 | 1.40 | 0.71 |
| **ETU conc. (mM)** | **Measured in BS1 (mM)** | **Error (%)** | **Measured in BS2 (mM)** | **Error (%)** |
| 0.70 | 0.95 | 35.9 | 0.74 | 5.42 |
| 1.05 | 1.14 | 8.67 | 1.08 | 2.57 |
| 1.40 | 1.40 | 0.21 | 1.40 | 0.07 |
| **DETU conc. (mM)** | **Measured in BS1 (mM)** | **Error (%)** | **Measured in BS2 (mM)** | **Error (%)** |
| 0.70 | 0.72 | 3.43 | 0.66 | 5.14 |
| 1.05 | 0.90 | 14.1 | 1.03 | 1.90 |
| 1.40 | 1.26 | 9.86 | 1.40 | 0.36 |

# 4. Conclusion

In this chapter, UV-visible spectroscopy and DT-CVS were applied for the quantification of TU concentrations in acidic Cu plating baths. The results of UV-visible spectroscopy indicated that although a peak related to the $[Cu\text{-}TU]^{2+}$ complex was clearly seen at 340 nm, the peak intensity non-linearly increased with TU concentrations because of the formation of another complex with a higher coordination number. The conventional DT-CVS cannot guarantee high accuracy because the electrochemical behavior of TU is concentration- and potential-dependent, which can cause disturbances in the response signals. In order to resolve this problem, a modified base solution containing PEG was used for the DT-CVS analysis, which led to a steep and stable drop in $Q/Q_{base}$ per unit concentration of TU, ETU, and DETU. The distinguishable and stable $Q/Q_{base}$ drop with the modified base solution was due to the elimination of the undesirable electrochemical behaviors of the TU-related species, by the addition of PEG. With this modified method, we have demonstrated an improvement in the accuracy of DT-CVS in determining the concentrations of TU-derivatives.

## 5. Reference


[1] M.J. Kim, S.H. Yong, H.S. Ko, T. Lim, K.J. Park, O.J. Kwon, and J.J. Kim, *J. Electrochem. Soc.*, **159**, D656 (2012).

[2] M. J. Kim, K. J. Park, T. Lim, O. J. Kwon, and J. J. Kim, *J. Electrochem. Soc.*, **160**, D3126 (2013).

[3] N. Tantavichet and M. D. Pritzker, *Electrochimica Acta*, **50**, 1849 (2005).

[4] N. Tantavichet S. Damronglerd, and M. D. Pritzker, *Electrochimica Acta*, **55**, 240 (2009).

[5] M. S. Kang, S.-K. Kim, K. Kim, and J. J. Kim, *Thin Solid Films*, **516**, 3761 (2008).

[6] K. Shravan Kumar, Krishanu Biswas , and R. Balasubramaniam, *J. Nanopart. Res*, **13**, 6005 (2011).

[7] K. Shravan Kumar and Krishanu Biswas, *Surf. Coat. Technol*., **214**, 8 (2013).

[8] A. Ghahremaninezhad, E. Asselin, and D.G. Dixon, *Electrochem. Commun*., **13**, 12 (2011).

[9] A. Ghahremaninezhad, E. Asselin, and D.G. Dixon, *J. Phys. Chem. C*, **115**, 9320 (2011).

[10] H. C. Kim , M. J. Kim , S. Choe , T. Lim , K. J. Park , K. H. Kim , S. H. Ahn , S.-K. Kim, and J. J. Kim, *J. Electrochem. Soc.*, **161**, D749 (2014).

[11] C.T. Wang and T. J. O'Keefe, in Proceedings of the International Symposium on Electrochemistry (edited by P. E. Richardson, S. Srinivasan and R. Woods), The Electrochemical Society, Pennington, NJ, 655 (1982).

[12] D. F. Suarez, and F. A. Olson, *J. Appl. Electrochem.*, **22**, 1002 (1992).

[13] N. Spataru, T. Spataru, and A. Fujishima, *Electroanal.*, **17**, 800 (2005).

[14] J. Rethmeier, G. Neumann, C. Stumpf, A. Rabenstein, and C. Vogt, *J. Chromatogr.*, **934**, 129 (2001).

[15] H. J. Bowley, E. A. Crathorne, and D. L. Gerrard, *Analyst*, **111**, 539 (1986).

[16] S. S. Kruglikov, N. T. Kudriavtsev, G. F. Vorobiova, and A. Y. Antonov, *Electrochimica Acta*, **10**, 253 (1965).

[17] C. J. Doona and D. M. Stanbury, *Inorg. Chem.*, **35**, 3210 (1996).

[18] C. J. Doona and D. M. Stanbury, *J. Phys. Chem.*, **98**, 12630 (1994).

[19] G. Horanyi and E. M. Rizmayer, *J. Electroanal. Chem.*, **149**, 221 (1983).

[20] D. Papapanayiotou, R. N. Nuzzo, and R. C. Alkire, *J. Electrochem. Soc.*, **145**, 3366 (1998).

[21] G. Garcia, V. A. Macagno, and G. I. Lacconi, *Electrochimica Acta,* **48**, 1273 (2003).

[22] A. Łukomska, S. Smolinski, and J. Sobkowski, *Electrochimica Acta*, **46**, 3111 (2001).

[23] J. O'M. Bockris, B. R. Scharifker, and J. L. Carbajal, *Electrochemica Acta*, **31**, 799 (1987).

[24] M.E.H. Garrido, M.D. Pritzker, *J. Electrochem. Soc*., **155**, D332 (2008).

[25] Z. V. Feng, X. Li, and A. A. Gewirth, *J. Phys. Chem. B*, **107**, 9415 (2003).

[26] B. Bozzini, L. D'Urzo, C. Mele, and V. Romanello, *J. Mater. Sci*., **17**, 915 (2006).

[27] S. Verma, S. L. Jain, and B. Sain, *Tetrahedron Lett.*, **51**, 6897 (2010).

[28] W.-P. Dow, M.-Y. Yen, W.-B. Lin, and S.-W. Ho, *J. Electrochem. Soc.,* **152**, C769 (2005).

[29] S.-L. Ko, J.-Y. Lin, Y.-Y. Wang, and C.-C. Wan, *Thin Solid Films*, **516**, 5046 (2008).

# Appendix II

## Seed Repair by Electrodeposition in Pyrophosphate Solution for Acid Cu Superfilling

### 1. Introduction

As aforementioned, electrodeposition is widely used to fabricate Cu interconnections as it can easily achieve void-free filling using a combination of additives.[1-11] Successful gap-filling requires thin Cu films, seed layers, to provide continuous electron pathways and to enhance adhesion between the diffusion barrier layer and deposited Cu. While Cu seed layers are generally fabricated by PVD,[12-14] the requirement of ever smaller features reaches the limits of PVD's capability to provide seed layers with conformality and continuity.[12-15] The deteriorated properties result in exposure of the barrier layer and voids forming after Cu gap filling.[15]

Discontinuous Cu seed layers can be repaired by electrodeposition or other deposition techniques.[16-20] Repair by electrodeposition generally employs an alkaline solution based on pyrophosphate, citric acid and ethylenediaminetetraacetic acid (EDTA), since an acidic bath would dissolve the seed layer and result in poor nucleation on the diffusion

barrier layer.[17-20] While seed layer repair has been reported to produce good results, deposition during the repair is generally more favorable on the Cu seed layer, rather than on the exposed barrier layer, and this still remains a critical issue.[17-20] The resulting increase of seed layer thickness reduces the process margin and causes center voids to emerge after Cu gap-filling.[17] The self assembly of monolayers on the Cu before repairing has been shown to reduce this preferential deposition of Cu.[20] By inhibiting Cu deposition on the Cu seed layer, Cu can be selectively deposited on the Ta and TaN diffusion barrier. A drawback of this method is the additional processing required to first prepare and later remove the monolayers: if the monolayer is not completely removed, it will increase resistivity.

The use of alternated potential waveforms, such as pulse, pulse-reverse or two-step electrodeposition can also improve the quality of the seed layer. Two-step electrodeposition is particularly useful in the direct electrodeposition of Cu seed layers on barrier layers, as its modified initial potential significantly influences the nucleation characteristic of Cu.[21-23] However, the application of two-step electrodeposition to repairing seed layers has not yet been reported.

This work reports the optimization of two-step electrodeposition for the repair of Cu seed layers damaged with a 55 nm wide trench. Layers were also repaired by one-step deposition for comparison.

## 2. Experimental

The electrolyte for seed repairing comprised 0.028 M $Cu_2P_2O_7$ and 1.00 M $K_4P_2O_7$. The plating solution used for pattern filling testing consisted of 0.25 M $Cu_2SO_4$, 1.0 M $H_2SO_4$, 90 μM PEG (Mw: 3400), 1 mM NaCl and 50 μM SPS.[1,3,4] Electrochemical analysis and electrodeposition were carried out using a three-electrode system controlled by a potentiostat (EG&G Princeton Applied Research Corporation, 263A). 99.9% Cu wire and Ag/AgCl (sat. KCl) were used as counter and reference electrodes, respectively. All experiments were conducted at room temperature.

Before seed repairing, linear sweep voltammetry (LSV) was performed at 10 mV/s to determine the potential range of Cu deposition and $H_2$ evolution on the surfaces of Cu and Ta working electrodes in the pyrophosphate solution.

Multilayer structures of PVD Cu (10 nm)/ PVD Ta (7.5 nm)/ PVD TaN (7.5 nm)/$SiO_2$ were deposited on blanket Cu wafers. Before experiments, the wafers were damaged by

immersion in acidic plating solution for 300 s. The damage in this study implies any chemical attack to the Cu film. It includes dissolution of Cu seed layers during the immersion in the acidic plating solutions or during the chemical etching of Cu oxide. In this study, we have adapted very harsh conditions of immersion of the Cu deposited wafer in acidic plating solution for 300 s to find the most appropriate method for the repairing. The structures were then repaired in the pyrophosphate repairing electrolyte by one- or two-step electrodeposition. One-step electrodeposition was a typical potentiostatic deposition that was conducted at a constant potential of -0.95 V, -1.15 V, -1.25 V, -1.45 V or -1.65 V. Two-step electrodeposition involved a 0.5 s nucleation pulse of higher potential and then a lower growth potential applied for longer. The nucleation potentials were -1.15 V, -1.45 V, -1.65 V and -1.85 V; the growth potential was consistently -1.15 V. The total charge during deposition was fixed at 100 mC.

Patterned Cu wafer, with a 55 nm wide trench with an aspect ratio of 6, had a multilayer structure of PVD Cu (7.5 nm)/ PVD Ta (6 nm)/ PVD TaN (1.5 nm)/$SiO_2$. It was oxidized by exposure to air for 1 month. The oxide was removed by immersing the wafer in a mixture of 0.02 M citric acid and 0.034 M KOH for 3 min. Repairing was then carried out at the optimum conditions established in the blanket wafer experiments. Filling tests were then conducted in plating solution with 10 $mA/cm^2$ current density.

Total deposition charges for repairing and pattern filling were 30 mC and 300 mC, respectively.

A four-point probe (Chang Min Co., CMT-SR 1000N) and a field-emission-scanning electron microscope (FESEM, Hitachi) were used to determine the surface morphology, Cu coverage and resistivity of the samples.

## 3. Results and Discussion

For more practical information, we defined the onset potential rather than the thermodynamic equilibrium potential. The onset potential means the potential value where the reaction started to become kinetically observable. LSV showed that the onset potential of Cu reduction was lower than that of $H_2$ evolution on both Cu and Ta surfaces (Fig. 1a). Cu reduction appeared much more favorable on Cu than on Ta. The additional overpotential for Cu reduction on the Ta layer was associated with the ohmic drop across the resistive Ta layer and the nucleation overpotential arising from the crystallographic mismatch between Cu and Ta. The summarized potential ranges (Fig. 1b) show that the onset potentials of the reduction were ranked: Cu deposition on Cu, Cu deposition on Ta, $H_2$ evolution on Cu and $H_2$ evolution on Ta. To reduce the preferential Cu deposition on

the Cu seed layer, the cathodic potential was modified to induce a higher nucleation density on the Ta layer, which would enhance the formation of a continuous Cu seed layer. The observed potential ranges suggest an appropriate potential of between -1.00 V and -1.65 V, where Cu nucleation can occur on Ta without $H_2$ evolution (Fig. 1b).

Damaged Cu seed layers were repaired at various constant applied potentials by one-step repairing. Surface images of damaged and repaired seed layers (Figs. 2a – f) were used to assess surface coverage. The surface coverage of Cu in % was calculated from the contrast differences between Cu and underlying Ta substrates. The contrast differences were obtained using Scion Image software followed by comparing the areas of Cu and Ta. Samples resistivities were also measured (Fig. 2g). The damaged wafer showed 78.1% surface coverage of Cu. This increased to over 90% after repairing due to the lateral growth of Cu at the remaining seed layer and the nucleation of Cu at the exposed Ta surface. Surface coverage was maximized at -1.15 V, resulting in the lowest resistivity, implying the highest continuity of repaired Cu layer.

LSV suggested that the optimal potential may be in the range from -1.00 to -1.65 V. Nucleation density exponentially increases with increasing overpotential,[18,19,23] hence a more negative potential favors the formation of nuclei. However, as the potential increased in magnitude from -1.15 V to -1.65 V, surface coverage dropped and resistivity

increased due surface roughening and decreased current efficiency owing to $H_2$ evolution on the Cu. In particular, the severe hydrogen evolution at -1.45 V, and -1.65 V caused the rapid increase in resistivities which are about 3~4 times higher than those of -0.95 V, -1.15 V and -1.25 V, despite their having comparable Cu coverage. The resistivities of Cu films repaired by -1.45 V and -1.65 V are even higher than the damaged one due to the dendritic growth of Cu resulting from hydrogen evolution. Therefore, an applied potential of -1.15 V was considered optimal for seed layer repairing, giving the best surface coverage and resistivity.

Surface coverage was shown to have been enhanced more by two-step potential electrodeposition. Applied potentials more negative than -1.15 V caused $H_2$ evolution on the Cu surface. Therefore, two-step electrodeposition involved a short nucleation pulse (0.5 s) of -1.15 V, -1.45 V, -1.65 V or -1.85 V, with subsequent Cu growth at -1.15 V. The total applied charge during two-step electrodeposition was consistently 100 mC. The surface morphology, coverage and resistivity of samples were observed after two-step electrodeposition (Fig. 3). The highest surface coverage and the lowest resistivity occurred after nucleation at -1.65 V. Lower magnitude nucleation potential resulted in lower surface coverage due to less nucleation of Cu on the Ta surface. Nucleation potential more negative than -1.65 V resulted in decreased surface coverage due to the

severe $H_2$ evolution on the Ta surface, as observed during LSV (Fig. 1), which showed $H_2$ evolution on the Ta layer occurring at potentials more negative than -1.65 V. $H_2$ gas produced on the Ta surface caused the detachment of Cu nuclei and inhibited nucleation. Therefore, the optimum conditions for two-step electrodeposition were nucleation at -1.65 V for 0.5 s and subsequent growth at -1.15 V.

The effectiveness of two-step electrodeposition was assessed by repairing intentionally damaged patterned wafers. Wafers were also repaired by one-step electrodepostion and the cross-sections of the samples were analyzed (Figs. 4a - c). The total charge used during repairing was reduced to 30 mC due to the small features. Nucleation during two-step repairing was consistently for 0.5 s. Given the profile of the damaged seed layer (Fig. 4a), only 77.5% of the trench was successfully filled without defects (Fig. 4d). However, continuity of the seed layers clearly recovered after both one-step (Figs. 4b & e) and two-step (Figs. 4c & f) repairing, leading to improved filling. Both one-step and two-step repairing led to effective pattern filling, despite the better performance of the two-step process on the blanket wafer. Nevertheless, it is highly recommended to use the two-step repairing to prevent possible micro-voids at the trench sidewalls and improve resistivity.

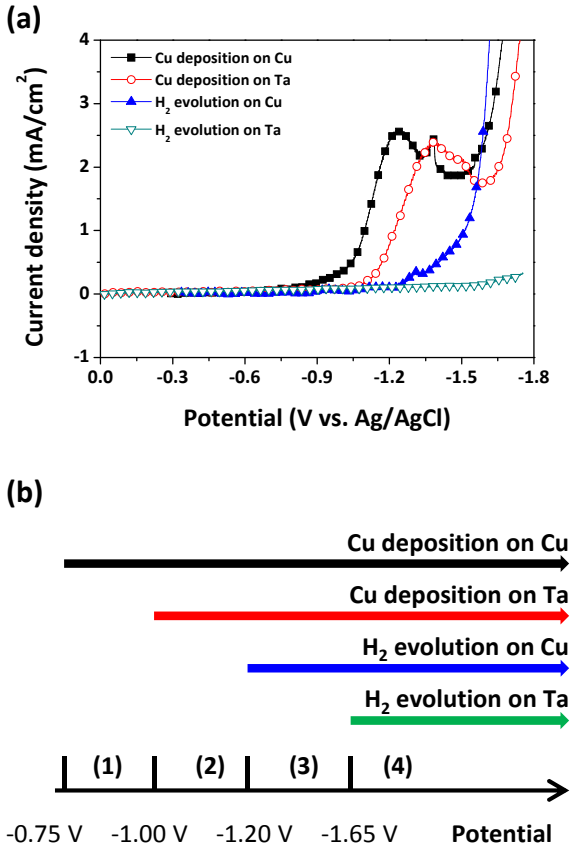


**Figure 1.** (a) LSV curves for Cu electrodeposition and $H_2$ evolution on Cu and Ta layer in pyrophosphate solution and (b) summarized potentials for Cu deposition and $H_2$ evolution on Cu and Ta surfaces.

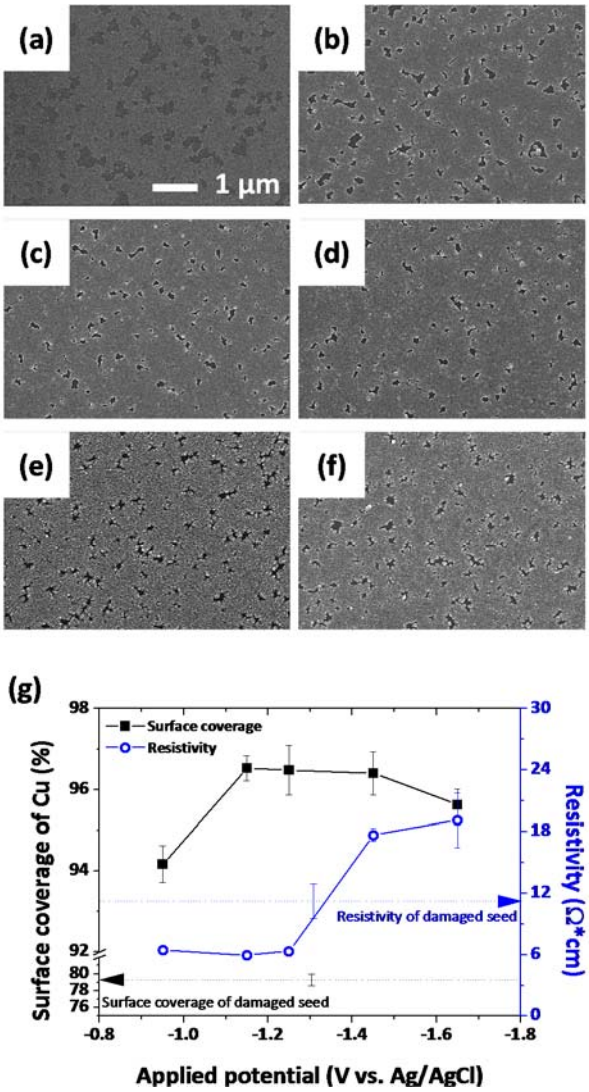


**Figure 2.** The surface morphologies of (a) damaged and (b)-(f) repaired seed layer. The repair potential were (b) -0.95 V, (c) -1.15 V, (d) -1.25 V, (e) -1.45 V, and (f) -1.65 V. The changes in surface coverage and the resistivities of repaired seed layers are summarized in (g). The horizontal dashed lines in (g) are the surface coverage and resistivity of the damaged seed shown in (a).

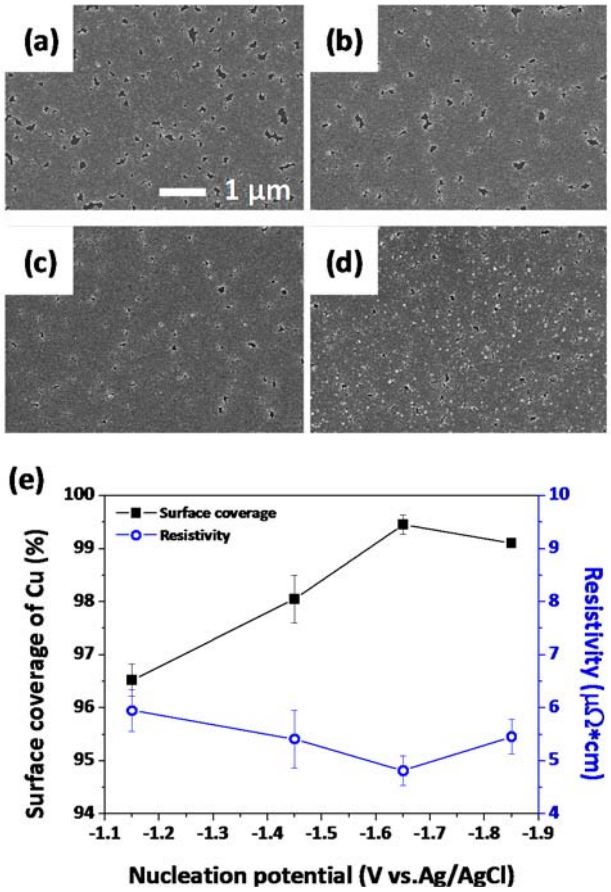


**Figure 3.** The surface morphologies of repaired seed layers. The two-step repairing was implemented with (a) -1.15 V, (b) -1.45 V, (c) -1.65 V, and (d) -1.85 V of nucleation potential for 0.5 s prior to -1.15 V of growth potential. The changes in surface coverage and the resistivities of repaired seed layers are summarized in (e).

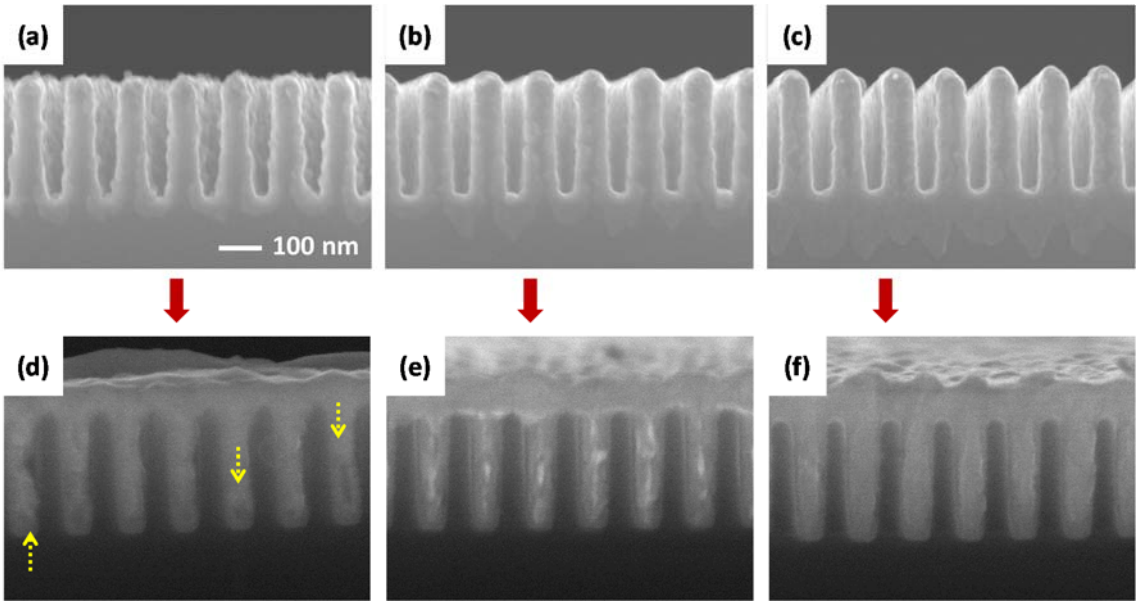


**Figure 4.** Cross sectional images of (a) damaged, (b) one-step repaired, (c) two-step repaired seed layer and (d)-(f) following filling performances of those seed layers.

# 4. Conclusion

Damaged Cu seed layers were successfully repaired by two-step electrodeposition, which consisted of nucleation at a higher potential and subsequent growth of Cu nuclei at a lower potential. Two-step electrodeposition efficiently enhanced the continuity and the surface coverage of damaged Cu seed layers, allowing void-free filling at the trenches.

## 5. Reference


[1] T. P. Moffat, D. Wheeler, and D. Josell. *J. Electrochem. Soc.*, **151**, C262 (2004).

[2] S. K. Cho, S. -K. Kim, and J. J. Kim, *J. Electrochem. Soc.*, **152**, C330 (2005).

[3] T. P. Moffat and L.-Y. Ou Yang, *J. Electrochem. Soc.*, **157**, D228 (2010).

[4] S. -K. Kim, S. K. Cho, J. J. Kim, and Y. -S. Lee, *Electrochem. Solid-State Lett.*, **8**, C19 (2005).

[5] M. J. Willey and A. C. West, *J. Electrochem. Soc.*, **154**, D156 (2007).

[6] S. -K. Kim, D. Josell and T. P. Moffat, *J. Electrochem. Soc.*, **153**, C616 (2006).

[7] D. Josell, D. Wheeler, C. Witt, T. P. Moffat, *Electrochem. Solid-State Lett.,*6, C143 (2003).

[8] J. –M. Seo, S. K. Cho, H. –C. Koo, S. –K. Kim, O. J. Kwon, J. J. Kim, *Korean J. Chem. Eng.,* **26**, 265 (2008).

[9] J. W. Gallaway, M. J. Willey, A. C. West, *J. Electrochem. Soc.*, **155**, C287 (2009).

[10] J. W. Gallaway, M. J. Willey, A. C. West, *J. Electrochem. Soc.*, **156**, C287 (2009).

[11] M. J. Kim, S. H. Yong, H. S. Ko, T. Lim, K. J. Park, O. J. Kwon, and J. J. Kim, *J. Electrochem. Soc.*, **159**, D656 (2012).

[12] S. T. Lim, Y. C. Park, S. J. Yoo, B. J. Lee, *Thin Solid Films*, **517**, 3935 (2009).

[13] J. Guillan, K. Haxaire, S. Chhun, E. Richard, M. C. Luche, L. Arnaud, E. Petitprez, C. Monget, D. Galpin, P. Normandon, *Microelectron. Eng*., **88**, 697 (2011).

[14]. T. Karabacak and T.-M. Lu, *J. Appl. Phys*. **97**, 124504 (2005).

[15] J. Reid, *Jpn. J. Appl. Phys*., **40**, 2650 (2001).

[16] S. K. Cho, T. Lim, H. -K. Lee, and J. J. Kim, *J. Electrochem. Soc.*, **157**, D187 (2010).

[17] J. H. Sukamto, E. Webb, T. Andryushchenko and J. Reid, *J. Appl. Electrochem*., **34**, 283 (2004).

[18] M. Zheng, J. J. Kelly, and H. Deligianni, *J. Electrochem. Soc*., **154**, D400 (2007).

[19] J. J. Kelly, M. Zheng, H. Deligianni, B. C. Baker-O'Neal, and C. Cabral, Jr., *J. Electrochem. Soc.*, **154**, D406 (2007).

[20] C. –Y. Liu and A. J. Bard, *Electrochem. Solid-State Lett*., **6,** C51 (2003).

[21] D. Starosvetsky, N. Sezin, Y. E. –Eli, *Electrochimica Acta*, **55**, 1656 (2010).

[22] S. Kim, *Electrochem. Solid-State Lett*., **13**, D83 (2010).

[23] E. Budevski, G. Staikov and W. J. Lorenz, *Electrochimica Acta*, **45**, 2559 (2000).

# Appendix III

# One-Step CVS Analysis to Measure the Average MW of PEG in Cu Plating Bath

## 1. Introduction

In chapter 5, it is demonstrated that the suppressor species fragmented into lower MW units during Cu electrodeposition, leading to the degradation of bath performance.[1-3] It is also revealed that the conventional DT-CVS is unable to detect the changes of MW of PEG, thereby resulting in the inaccurate diagnosis and the improper feedback.

Considering those factors, it is necessary to develop the additional *in-situ* method to analyze the average MW of PEG in Cu plating bath. Hence, in this chapter, a simple electrochemical method to analyze the average MW of PEG is suggested, based on the hysteresis behavior in CVS plots at the low concentration of PEG. The interior area of hysteresis, which are shown to be related with the adsorption kinetics of PEG, are utilized to evaluate the average MW of PEG in Cu plating bath. Additionally, the origin

of hysteresis is clarified by means of the simulation results that are obtained with Tafel plot and Langmuir isotherm equations.

## 2. Experimental

Cu plating solutions comprised 0.25 M $CuSO_4$, 1.0 M $H_2SO_4$, and 1 mM NaCl. CVS analysis was aimed at observing the electrochemical behavior of the solutions and measuring the electrochemical and adsorption/desorption kinetic parameter. A Pt rotating disk electrode with a rotating speed of 2000 rpm, a Pt rod, and Ag/AgCl (3 M KCl) were used as the working, counter, and reference electrodes, respectively. The reference electrode is sealed with outer plastic tube filled with 1 M $KNO_3$ to minimize $Cl^-$ leakage into the samples. A scan rate of 0.1 V/s and a vertex potential of -0.45 V were constantly applied.

## 3. Results and Discussion

Figure 1 presents the CVS results for bathes containing PEGs with MW of 600-6000. For all cases, the hysteresis is apparently observed and its interior area increases with the

increase of MW of PEG. The formation of hysteresis is attributed to the delay between desorption and re-adsorption of PEG on Cu surface during voltammetric scanning.[4-6] In detail, the PEG rapidly desorbs from cathode electrode during forward sweep of CVS because the coverage of PEG decrease with the increase in cathodic overpotential. Otherwise, in the return sweep, the suppressor re-adsorbs again on electrode surface and begin to rebuild the inhibition layers. However, the re-adsorption of PEG is so slow that the surface coverage of PEG at return sweep is lower than that at forward sweep, resulting in the hysteresis behaviors during CVS analysis.

Figure 2 presents the changes of interior hysteresis areas expressed as $Q_b$ (the total cathodic charge amount during return sweep) – $Q_f$ (the total cathodic charge amount during forward sweep) as function of concentration and MW of PEG. It is observed that the interior hysteresis areas are maximized at the specific concentrations and the maximum hysteresis areas strongly depends on the average MW of PEG.

The relation between the maximum hysteresis area and the average MW of PEG is shown in Figure 3. It is evident that the maximum hysteresis area increases as the average MW of PEG increases. This relation is further used as the standard calibration curve to determine the average MW of PEG in the unknown samples.

Table 1 presents the actual and measured MW values of PEGs that have either symmetric or bimodal MW distributions. The samples with bimodal MW distributions are made by mixing two symmetric PEG samples with proper mass ratio. All measured values in Table 1 are well matched with actual values less than 10% error, indicating the accuracy of this method regardless whether the MW distribution is symmetric or bimodal.

The dependency of interior area of hysteresis on the average MW of PEG may be ascribed by the difference in adsorption kinetic parameters of PEG. For elucidating the origin of hysteresis, I simulate the CVS results with assumption that the adsorption of PEG follows ideal Langmuir isotherm, as described at Eq. 1.

$$\frac{d\theta}{dt} = k_a(1-\theta)C - k_d\theta \ (Eq.1)$$

Here, C is the bulk concentration of PEG, $\theta$ is the surface coverage of PEG on the cathode electrode, $k_a$ is the adsorption kinetic constant, and $k_d$ is the desorption kinetic constants, respectively.

I also assume that the current density for Cu deposition can be expressed as the modified Butler-Volmer equation, as described at Eq. 2.

$$i_{none} = \frac{i_0 \exp[\frac{-\alpha nF}{RT}\eta]}{1 + \frac{i_0 \exp[\frac{-\alpha nF}{RT}\eta]}{i_L}} = \frac{i_k}{1 + \frac{i_k}{i_L}} \ (\text{Eq. } 2)$$

Here, $i_0$ is the exchange current, $\alpha$ is the symmetric factor, R is the gas constant, F is the Faraday constant, T is the temperature of solution, and $i_L$ is the limiting current.

However, in the presence of PEG, the partial surface area covered by PEG is passivated, resulting in the decrease of kinetic current density ($i_k$). Considering those factors, the current density could be approximated as Eq 3.

$$i_{supp} = \frac{(1-\theta)i_k}{1+\frac{(1-\theta)i_k}{i_L}} \ (Eq.3)$$

The electrochemical and adsorption kinetic parameters are evaluated with the preliminary electrochemical experiments. All electrochemical parameters are determined with Tafel plot obtained from the series of linear sweep voltammetry (LSV) experiments with various rotating speeds. The obtained $i_0$ and $\alpha$ values from Tafel plot are -0.28 mA and 0.4, respectively, which are in good agreement with the previous literatures.[7] The adsorption kinetic parameters of PEG are measured by chronoamperometry experiments, from which the linear regression between $\frac{d\theta}{dt}$ and $\theta$ are used to determine the $k_a$ and $k_d$.

$$\frac{d\theta}{dt} = (-k_aC - k_d)\theta + k_aC \ (\text{Eq.}4)$$

Figure 4 shows the experimental and simulation results of CVS plots from bath containing 14.2 mg/L PEG-1050. It is clearly observed that the simulation result is well consistent with the experimental result, indicating the accuracy of this simulation.

In conclusion, the hysteresis curve is evolved on CVS plots in the presence of PEG due to the delay between desorption and re-adsorption of PEG on Cu surface. The relation between interior hysteresis area and average MW of PEG might be utilized to evaluate the MW of PEG in Cu plating bath for industrial application.

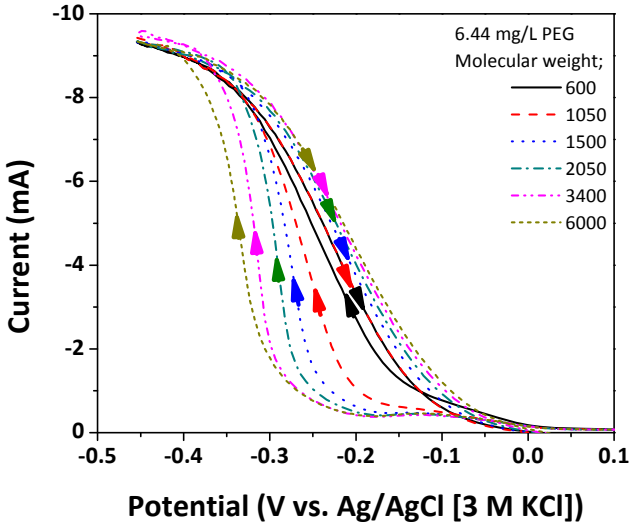


**Figure. 1**. CVS results for Cu plating bathes containing PEG with various MW. The concentration of PEG is fixed as 6.44 mg/L.

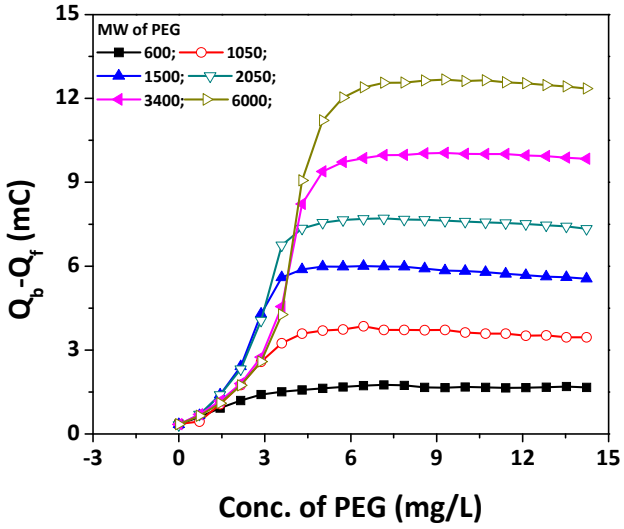


**Figure. 2**. Interior hysteresis areas expressed as $Q_b$ – $Q_f$ with various MW and concentration of PEG.

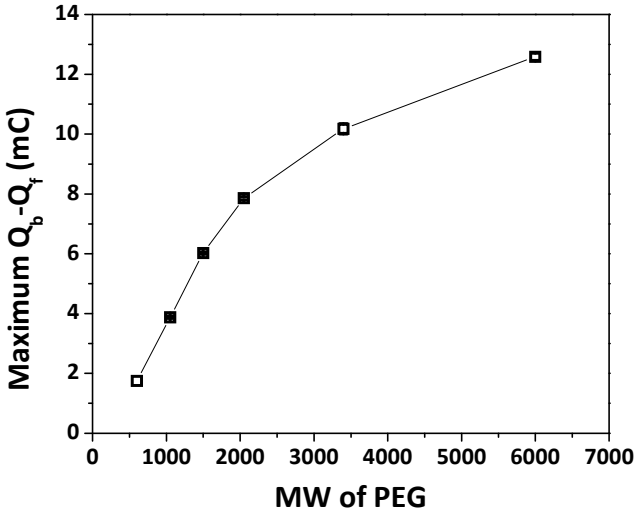


**Figure. 3**. Maximum interior hysteresis area expressed as $Q_b - Q_f$ as functions of MW of PEG.

**Table 1**. Actual and Measured Values of MW of PEG in Cu Plating Bath.

| | Combination | | | | | Average MW | Measured MW | Error(%) |
|---|---|---|---|---|---|---|---|---|
| Sample | 600 | 1050 | 1500 | 2050 | 3400 | | | |
| 1 | 0 | 0 | 0 | 1 | 0 | 2050 | - | - |
| 2 | 0 | 0 | 0.71 | 0 | 0.29 | 2050 | 1882 | 8.54 |
| 3 | 0 | 0.57 | 0 | 0 | 0.43 | 2050 | 1906 | 7.28 |
| 4 | 0.48 | 0 | 0 | 0 | 0.52 | 2050 | 2149 | 4.72 |
| 5 | 0 | 0.5 | 0.5 | 0 | 0 | 1275 | 1274 | 0.08 |
| 6 | 0 | 0 | 0 | 0.5 | 0.5 | 2725 | 2679 | 1.69 |

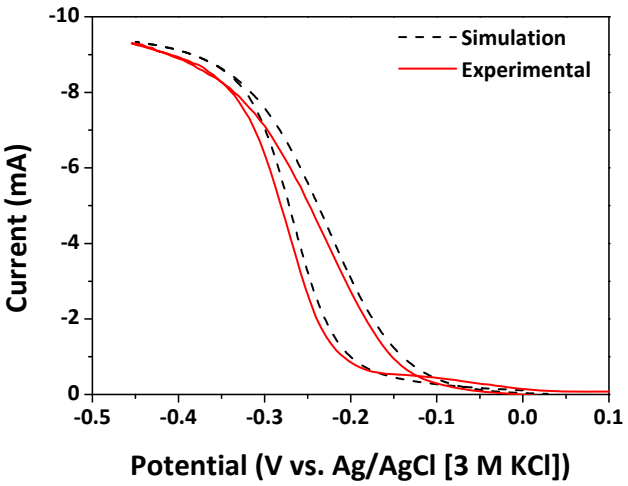


**Figure. 4**. Experimental and simulation results of CVS from bath containing 14.2 mg/L PEG-1050.

## 4. Conclusion

Modified CVS method is suggested as a monitoring tool for the determination of MW of PEG in Cu plating bath. Hysteresis, whose interior area depends on the MW of PEG, is formed during CVS analysis. The interior area of hysteresis is used to evaluate the average MW of PEG in the unknown Cu plating bath. This modified method can be simply applied as *in-situ* monitoring tool of Cu plating bath in various industrial field.

## 5. Reference

[1] W. P. Dow, M. -Y. Yen, W. -B. Lin, and S. -W. Ho, J. *J. Electrochem. Soc.*, **152**, C769 (2005).

[2] J. -M. Shieh, S. -C. Chang, B. -T. Dai, and M. -S. Feng, Jpn. *J. Appl. Phys.*, **41**, 6347 (2002).

[3] R. Maru and S. Jayakrishnan, *Bull. Mater. Sci.*, **34**, 347 (2011).

[4] M. E. H. Garrido and M. D. Pritzker, *J. Electrochem. Soc.*, **155**, D332 (2008).

[5] M. J. Willey and A. C. West, *J. Electrochem. Soc.*, **153**, C728 (2006).

[6] L. Yang, A. Radisic, J. Deconinck, and P. M. Vereecken, *J. Electrochem. Soc.*, **161**, D269 (2014).

[6] T. P. Moffat, D. Wheeler, M. D. Edelstein, and D. Josell, *IBM J. Res. & Dev.*, **49**, 19 (2005).